RICE UNIVERSITY

Thermal Generation of Spin Current in the Magnetic Insulators

by

Renjie Luo

A Thesis Submitted
in Partial Fulfillment of the
Requirements for the Degree

Doctor of Philosophy

Approved, Thesis Committee:

Douglas Natelson, Chair of the committee
Professor of Physics and Astronomy

Matthew Foster
Associate Professor of Physics and Astronomy

Hanyu Zhu
Assistant Professor of Materials Science and NanoEngineering

Houston, Texas

July, 2025

ABSTRACT

Thermal Generation of Spin Current in the Magnetic Insulators

by

Renjie Luo

The increasing demands for energy-efficient information technologies have driven interest in spin caloritronics, where the interaction of charge and spin degrees of freedom with heat current is actively investigated. Among them, the spin Seebeck effect (SSE), the thermal generation of spin current in a magnetic insulator / nonmagnetic metal junction system, has drawn particular attention. The SSE has been vastly studied in ferrimagnetic insulators, particularly $Y_3Fe_5O_{12}$ (YIG), with magnetic field, temperature, thickness dependence, and magnon-based theories are well-developed. However, investigation of the SSE in paramagnets and antiferromagnets is still in the development. The absence of the long-range order in paramagnets raises fundamental questions about spin current generation and transport. Antiferromagnets have no net magnetic moment, are robust against external fields, and can be operated at terahertz frequencies, making them a promising material for spintronics devices. Understanding the spin dynamics in the antiferromagnets also becomes a major objective.

In this thesis, we experimentally demonstrate SSE in two magnetic insulators, paramagnetic vanadium dioxide (VO_2) and antiferromagnetic vanadium sesquioxide (V_2O_3), both at low temperatures. In the nonlocal configuration, the SSE signal in VO_2 film grows in magnitude with decreasing temperature below an onset of detectability at approximately 30 K, with a sign reversal between 15 K and 10 K. The SSE signal saturates in high magnetic field, and displays the expected dependence

on in-plane field orientation. In the longitudinal configuration, the SSE signal in VO_2 grows linearly with increasing field at low fields, but experiences a field-induced reduction at high fields and the lowest temperatures, qualitatively consistent with a paramagnetic SSE model. Under fixed heater power, the magnitude of SSE voltage shows non-monotonic behavior with temperature. The sign of the SSE response is not consistent with that expected for a triplon-dominated SSE, in which mobile triplet excitations are the angular momentum carriers. The SSE in V_2O_3 shares several qualitative features with that in VO_2; however, the SSE magnitude in V_2O_3 consistently decreases as a function of film thickness. It's interpreted in the context of antiferromagnetic magnons, suggesting that the length scale for thermal relaxation between magnons and phonons in V_2O_3 is shorter than 50 nm, consistent with the wealth of experimental support for strong spin-lattice interactions in V_2O_3.

Our findings explore the field of SSE and may help better understand the mechanism of spin transport in various materials. Pertinent open questions and possible future research directions will also be discussed.

Acknowledgments

First of all, I would like to express my profound gratitude to my advisor, Prof. Douglas Natelson, for his unwavering support, invaluable guidance, and insightful feedback throughout my six years' graduate studies and researches. His motivation, enthusiasm, and vast knowledge greatly helps me to grow as a researcher. I feel fortunate to have had him as my advisor, and I'll always cherish the profound impact he's had on my life.

I would also like to thank Prof. Matthew Foster and Prof. Hanyu Zhu for serving in my defense committee and for providing insightful comments and suggestions for my projects. I would also like to thank Prof. Patricia H. Reiff for her participation in my advisory committee for annual program review.

I would like to extend my gratitude to all my collaborators for their invaluable contributions to the projects. Without their dedication and support, this thesis would not have been possible. I want to thank Dr. Ali C. Basaran, Dr. Henry Navarro, Dr. Erbin Qiu, and Dr. Ivan K. Schuller for offering vanadium oxide film samples and fruitful discussions; I want to thank Dr. Anand Bhattacharya, Dr. Deshun Hong, and Dr. Changjiang Liu for offering YIG samples.

I would like to thank the staff in Shared Equipment Authority (SEA) at Rice University: Dr. Bo Chen, Dr. Timothy Gilheart, Dr. Carlos Gramajo, Dr. Jing Guo, Dr. Jianhua Li, and Dr. Nadia Pervez. Their technical expertise and shared enthusiasm have made my time in the cleanroom and on the shared equipments productive and enjoyable.

I would like to express my gratitude to the following members of the Natelson lab for their invaluable contributions to our research projects, especially to the spintronics

group: Dr. Mahdiyeh Abbasi, Dr. Liyang Chen, Dr. Longji Cui, Dr. Xifan Wang, Dr. Jiawei Yang, Dr. Xuanhan Zhao, Dr. Yunxuan Zhu, Gage Eichman, Tanner Legvold, Shushen Liao, Dale Lowder, Ken Ssennyimba, Yuxin Wan, and Kexin Xie. Among them, I would like to express deepest gratitude to Dr. Liyang Chen for his patient guidance during my early days in the Natelson lab. I am also profoundly saddened by the sudden passing of Mr. Tanner Legvold this spring. He worked in the same field (spin caloritronics) in the Natelson group and contributed significantly to the thermal simulations in this thesis. His dedication and kindness left a lasting impression on me, and I will carry his memory with me always.

I would like to thank all my friends here at Rice University. Forgive me for not able to list their names here, but I really appreciate their companion and support to entertain my graduate student life.

Finally, I would like to extend my heartfelt appreciation to my parents, Mr. Nianhua Luo and Mrs. Xiaojun He, for their unconditional support during the challenging times. Their love is the most precious gift I have ever received, and I will always be grateful for having them in my life.

Contents

List of Figures

List of Tables

Chapter 1

Introduction

1.1 Spintronics and spin caloritronics

After the observation of spin-polarized electron injection from a ferromagnetic metal to a normal metal in 1985 and the discovery of giant magnetoresistance (GMR) in 1988, the field of spintronics emerges [1–3]. Spintronics involves the study of active control and manipulation of spin degrees of freedom in solid-state systems for information processing and storage, providing potential advantages over conventional charge-based electronics, such as reduced power consumption and increase their memory and processing capabilities. Many phenomena have been studied, including the interplay of charge and spin transport, spin dynamics in magnetic systems, and the electrical manipulation of magnetization switching by spin-transfer torque and spin-orbit torque. For large-scale commercial applications, the GMR-based spin valves and magnetic tunnel junctions (MTJs) have been extensively used as magnetic field sensors in the read heads of hard disk drives, position or proximity sensors in automated industrial tools, and data storage like magnetic random access memory (MRAM). The latest development has been employing three-dimensional structures and quantum engineering, including the applications for quantum computation.

The thermoelectric effects [4] denote the direct interconversion of temperature differences to electric voltage and vice versa, including the Seebeck effect and the Nernst(-Ettingshausen) effect. In the Seebeck effect, when a conductor is subjected

to a temperature gradient, an electromotive force develops between the two ends. The temperature gradient drives charge carriers (electrons or holes) diffusion from the warmer region of the conductor towards the cooler region. Under the open circuit conditions, a difference in the electronic chemical potential develops between the two ends, so that a drift current driven by the electromotive force balances out the diffusion current driven by the temperature gradient. At equilibrium, this drift current ensures no net current flow and the resulting voltage difference is known as the Seebeck emf. The magnitude and polarity of the Seebeck effect depend on the dominant carrier type in the conductor (electrons or holes) and the energy dependence of the electrical conductivity. In the Nernst effect, a transverse electric field is produced by a longitudinal temperature gradient in the presence of a mutually perpendicular magnetic field.

The paradigm of spintronics is to investigate the interplay between charge current and spin current. Inspired by the thermoelectrics which deal with the interconversion between the charge current and heat current, a new field of research, spin caloritronics [5,6], where the interaction of charge and spin degrees of freedom with heat current is actively investigated. In spin caloritronics, various thermo-spin conversion phenomena and principles have subsequently been discovered and magneto-thermoelectric effects, thermoelectric effects unique to magnetic materials, have received renewed attention with the advances in physical understanding and thermal/thermoelectric measurement techniques. Some typical thermo-spin effects are listed below:

- spin-dependent Seebeck and Peltier effect, spin versions of ordinary Seebeck and Peltier effect, due to thermal transport of spin-polarized conduction electrons.

- spin Seebeck effect, where a temperature gradient generates via spin pumping

a diffusive spin current in the adjacent metal.

- spin Peltier effect, the Onsager reciprocal of spin Seebeck effect, where a temperature modulation occurs in response to spin accumulation.

- spin Nernst effect, the thermal analogue of the spin Hall effect, where a conduction-electron spin current is generated in nonmagnetic conductors via the spin-orbit interaction in the direction perpendicular to the applied heat current.

The societal relevance of the spin caloritronics is given by the imminent breakdown of Moore's Law by the thermodynamic bottleneck: Further decrease in feature size and transistor speed goes in parallel with intolerable levels of Ohmic energy dissipation associated with the motion of electrons in conducting circuits. Spin caloritronics is intimately related to possible solutions to these problems by making use of the spin degree of freedom. Although the thermoelectric conversion efficiency of the spin caloritronics is much smaller than that of the conventional thermoelectric methods, the field of the spin caloritronics is still in a infant stage and novel phenomena are discovered frequently. Further discovery of new principles and improvement of the thermo-spin conversion efficiencies are expected in the future.

1.2 Spin current

To better understand the idea of spintronics and spin caloritronics, the notion of "spin current" plays an essential role [7]. Spin current is a flow of spin angular momentum. Generally, the spin current can be defined by the continuity equation for the magnetization $\boldsymbol{M}$ as:

$$\frac{\mathrm{d}\boldsymbol{M}}{\mathrm{d}t} = -\gamma \nabla \cdot \boldsymbol{j}_s + \boldsymbol{T}, \tag{1.1}$$

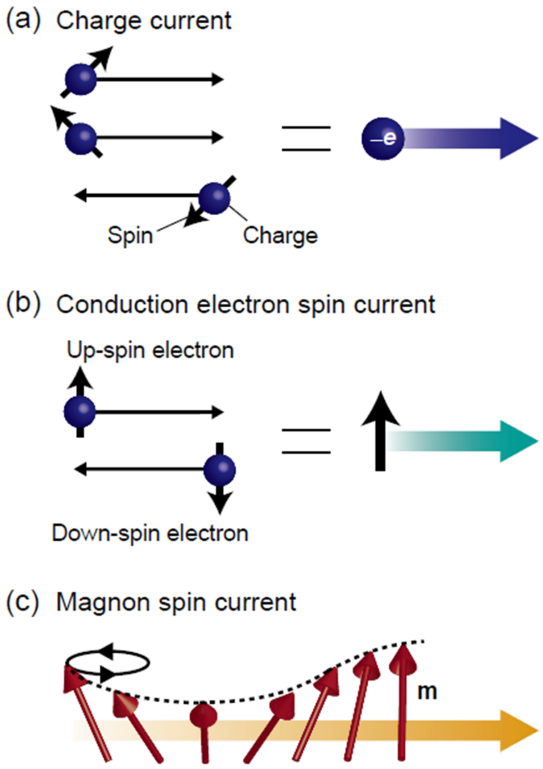

Figure 1.1 : Schematic illustrations of (a) the charge current, (b) the conduction electron spin current, and (c) the magnon spin current. $-e$ and m denote the electron charge and the magnetic moment, respectively. Taken from [6].

where γ is the gyromagnetic ratio, $\boldsymbol{T}$ includes spin relaxation process, and $\boldsymbol{M}$ includes not only the macroscopic spontaneous magnetization but also nonequilibrium components. Unlike charge current, the spin current is a non-conserved quantity that disappears over a certain distance after a certain time. Depending on the mobile carrier, the spin current can be categorized into conduction-electron spin current, magnon spin current, or spin current carried by other quasiparticles.

1.2.1 Conduction-electron spin current

The electrons carry not only charge $-e$, but also spin angular momentum $s = 1/2$. When an electric field is applied to a conductor, there is a slight difference in electrons quantities having a velocity component parallel and antiparallel to the electric field. Due to this slight imbalance in the electron velocity distribution, a group of electrons flows in a certain direction, which is a charge current. When the number of spin-up electrons and spin-down electrons is not equal, such as in a ferromagnetic conductor, this charge current can carry a flow of spin angular momentum, sometimes called spin-polarized current. An important case is that the spin-up and spin-down electrons flow in the opposite directions with the same magnitude. In this situation, the charge flows cancel out each other and the net charge current is zero; by contrast, the spin flow remains uncanceled. This is a spin current carried by conduction electrons.

The spin z component of the spin current is expressed as:

$$\boldsymbol{J}_s = \frac{\hbar}{2}(\boldsymbol{j}_\uparrow - \boldsymbol{j}_\downarrow), \tag{1.2}$$

where $\hbar$ is reduced Planck constant and the current $\boldsymbol{j}_{\uparrow(\downarrow)}$ represents a particle flow carrying the upward (downward) spin. By contrast, a charge current is described as:

$$\boldsymbol{J}_c = (-e)(\boldsymbol{j}_\uparrow + \boldsymbol{j}_\downarrow), \tag{1.3}$$

where $-e$ is the charge of electron. Then, we introduce the spin dependent chemical potentials, $\mu_{\uparrow(\downarrow)}$, which satisfy $\boldsymbol{j}_{\uparrow(\downarrow)} = D\nabla\mu_{\uparrow(\downarrow)}$, where D is the electron diffusion constant. The spin current $\boldsymbol{J}_s$ can be written as:

$$\boldsymbol{J}_s = \frac{\hbar}{2}D\nabla(\mu_\uparrow - \mu_\downarrow). \tag{1.4}$$

This shows that $\mu_\uparrow - \mu_\downarrow$ acts as a driving force for conduction-electron spin current. Actually, spin is not a conservative quantity, it's difficult to transport the spin current

over long distances, which is totally different from a charge current. As a result, the conduction-electron spin current disappears after flowing over a certain distance, which is named the spin diffusion length.

1.2.2 Magnon spin current

Magnons [8], the quanta of spin waves, are a quasiparticle that describes the collective wave-like behavior of localized magnetic moments in magnetic materials. A magnon is a spatially modulated deviation of the local spin direction from that of the magnetically ordered state. Magnons are bosonic quasiparticles, propagating in the $\boldsymbol{k}$ direction and each one transporting $\hbar$ angular momentum directed opposite to the spin orientation of the magnetically ordered sublattice. Thus, a flow of magnons can carry a flow of spin angular momentum.

In ferromagnets, the permanent magnetic moments of atoms or ions align parallel to a certain direction and the matter exhibits finite magnetization even in the absence of external magnetic field. Now consider low-energy excitations from a ferromagnetic ground state where each spin is aligned along the z-axis. Assume that spins are coupled with nearest neighbor spins via the exchange interaction. In a simple situation where only nearest neighbor interactions are important and all nearest exchange interactions are equal [7], the Hamiltonian is:

$$\mathcal{H} = -2J \sum_{\langle i,j \rangle} \boldsymbol{s}_i \cdot \boldsymbol{s}_j - g\mu_B \sum_i \boldsymbol{H} \cdot \boldsymbol{s}_i, \tag{1.5}$$

where $\boldsymbol{s}_i$ represents the spin operator of an atom or an ion at the position labeled by i, $J(>0)$ is the nearest neighbor exchange interaction parameter between the spin $\boldsymbol{s}_i$ and its neighbor $\boldsymbol{s}_j$, and the second term represents the Zeeman energy (μ_B is the Bohr magneton, g is the spectroscopic splitting factor, $\boldsymbol{H}$ is the external field along

the z-axis). We will further assume $s = 1/2$. Using the spin raising and lowering operators for the ith spin site, $s_i^+ = s_{ix} + is_{iy}$, $s_i^- = s_{ix} - is_{iy}$, the Hamiltonian becomes:

$$\mathcal{H} = -2J \sum_{\langle i,j \rangle} \left[\frac{1}{2}(s_i^+ s_j^- + s_i^- s_j^+) + s_{iz} s_{jz} \right] - g\mu_B H \sum_i s_{iz}. \tag{1.6}$$

By introducing $s_{\boldsymbol{k}}$ with the Bloch representation:

$$s_{\boldsymbol{k}}^{\pm} = \frac{1}{\sqrt{N}} \sum_j e^{-i\boldsymbol{k}\cdot\boldsymbol{R}_j} s_j^{\pm}, \tag{1.7}$$

the Hamiltonian can be written in a diagonal form:

$$\mathcal{H} = \sum_{\boldsymbol{k}} \hbar\omega_{\boldsymbol{k}} s_{\boldsymbol{k}}^{\dagger} s_{\boldsymbol{k}}, \tag{1.8}$$

where $\omega_{\boldsymbol{k}}$ is the eigenfrequency with wavevector $\boldsymbol{k}$:

$$\hbar\omega_{\boldsymbol{k}} = 2sJZ(1 - \gamma_{\boldsymbol{k}}) + g\mu_B H, \tag{1.9}$$

where Z is the number of nearest neighbors and $\gamma_{\boldsymbol{k}} = \frac{1}{Z} \sum_{\boldsymbol{R}_i - \boldsymbol{R}_j} e^{i\boldsymbol{k}\cdot(\boldsymbol{R}_i - \boldsymbol{R}_j)}$. The above discussion shows that the spin configuration behaves as an oscillatory motion with frequency $\omega_{\boldsymbol{k}}$ and wavevector $\boldsymbol{k}$. This collective mode is the spin wave that is mediated by the exchange interactions. For small k, the eigenfrequency of spin wave shows a quadratic dependence on the wavevector around the minimum at $\boldsymbol{k} = 0$.

Then the magnon spin current is expressed as:

$$\boldsymbol{j}^{M_z} = \hbar \sum_{\boldsymbol{k}} \boldsymbol{v}_{\boldsymbol{k}} n_{\boldsymbol{k}}, \tag{1.10}$$

where $\boldsymbol{v}_{\boldsymbol{k}} = \partial\omega_{\boldsymbol{k}}/\partial\boldsymbol{k}$ is the group velocity of the magnon with wavevector $\boldsymbol{k}$, and $n_{\boldsymbol{k}}$ is the distribution function of the magnons. It shows when the numbers of excited spin waves are different between $\boldsymbol{k}$ and $-\boldsymbol{k}$, a nonzero net spin current is carried by the spin waves: a magnon spin current.

Antiferromagnetic states refer to states in which the permanent magnetic moments align antiparallel and cancel each other out and thus the net magnetization is zero in the absence of magnetic fields (Fig. 1.2a). Consider the Hamiltonian of a two-sublattice antiferromagnet consisting of contributions from Zeeman, exchange, and magnetic anisotropy energies in the form [9]:

$$\mathcal{H} = \sum_{\langle i,j \rangle} 2J_{ij}\boldsymbol{s}_i \cdot \boldsymbol{s}_j - D\sum_i (s_i^z)^2 - g\mu_B \sum_i \boldsymbol{H} \cdot \boldsymbol{s}_i, \tag{1.11}$$

where $\boldsymbol{s}_i$ is the spin-s ($s \neq 1/2$) at a generic lattice site i , J_{ij} is the exchange constant of the interaction between spins $\boldsymbol{s}_i$ and $\boldsymbol{s}_j$, D is the uniaxial anisotropy constant, g is the spectroscopic splitting factor, μ_B is the Bohr magneton, and $\boldsymbol{H}$ is the magnetic field lying in the z direction. Using the Holstein-Primakoff approach [10], the Hamiltonian becomes diagonal in the form:

$$\mathcal{H} = \sum_{\boldsymbol{k}} \hbar(\omega_{\alpha\boldsymbol{k}}\alpha_{\boldsymbol{k}}^\dagger\alpha_{\boldsymbol{k}} + \omega_{\beta\boldsymbol{k}}\beta_{\boldsymbol{k}}^\dagger\beta_{\boldsymbol{k}}), \tag{1.12}$$

where $\alpha_{\boldsymbol{k}}^\dagger$, $\alpha_{\boldsymbol{k}}$, and $\beta_{\boldsymbol{k}}^\dagger$, $\beta_{\boldsymbol{k}}$ are the creation and destruction operators for the two magnon modes which satisfy the boson commutation rules; $\omega_{\alpha\boldsymbol{k}}$ and $\omega_{\beta\boldsymbol{k}}$ are the frequencies of these two magnon modes, given by:

$$\omega_{\alpha\boldsymbol{k}} = \omega_{\boldsymbol{k}} + \gamma H, \;\; \omega_{\beta\boldsymbol{k}} = \omega_{\boldsymbol{k}} - \gamma H, \tag{1.13}$$

$$\omega_{\boldsymbol{k}} = \gamma[H_c^2 + H_E^2(1-\gamma_{\boldsymbol{k}}^2)]^{1/2}, \tag{1.14}$$

$$H_c = [H_A(2H_E + H_A)]^{1/2}, \tag{1.15}$$

$$\gamma_{\boldsymbol{k}} = (1/z)\sum_{\boldsymbol{\delta}} \exp(i\boldsymbol{k}\cdot\boldsymbol{\delta}), \tag{1.16}$$

where $\gamma = g\mu_B/\hbar$ is the gyromagnetic ratio, $H_E = 2zSJ/\gamma\hbar$ is the effective exchange field, $H_A = (2S-1)D/\gamma\hbar$ is the anisotropy field, z is the number of the nearest neighbors, $\boldsymbol{\delta}$ is the vector connecting nearest neighbor. The frequencies of the two

magnon modes are minimum at the center of the sublattice Brillouin zone, $\boldsymbol{k} = 0$, where $\omega_\alpha(k = 0) = \gamma(H_c + H)$, $\omega_\beta(k = 0) = \gamma(H_c - H)$. As k increases, both frequencies increase quadratically near the $\boldsymbol{k} = 0$ point, and reach the maximum values at the Brillouin zone boundary. The two modes are degenerate in the absence of the external magnetic field. The application of an external field $\boldsymbol{H}$ in the direction of the anisotropy lifts the degeneracy. As the field increases, the frequency of the α mode increases while the one of the β mode decreases (Fig. 1.2b). In the magnon mode, the two sublattice magnetizations are nearly opposite to each other, and they precess circularly in the same sense, counterclockwise in the α mode and clockwise in the β mode.

Similarly, the magnon spin current in the antiferromagnet is expressed as:

$$\boldsymbol{j}^{M_z} = \hbar \sum_{\boldsymbol{k}} \boldsymbol{v}_{\boldsymbol{k}} (-\alpha^\dagger_{\boldsymbol{k}} \alpha_{\boldsymbol{k}} + \beta^\dagger_{\boldsymbol{k}} \beta_{\boldsymbol{k}}), \tag{1.17}$$

If the field reaches the critical value H_c, the frequency $\omega_\beta(k = 0)$ becomes 0, indicating the antiferromagnetic phase is no longer stable and there is a transition to the spin-flop (SF) phase. In the SF phase, the magnetizations in both sublattices ($\boldsymbol{m}_1$ and $\boldsymbol{m}_2$) rotate abruptly to be nearly perpendicular to the field $\boldsymbol{H}$ with a small angle $\theta = \arccos\left(H/(2H_E - H_A)\right)$ with the field, giving a small net magnetization $\boldsymbol{m} = \boldsymbol{m}_1 + \boldsymbol{m}_2$ along the field (Fig. 1.2a). Still, we can diagonalize the Hamiltonian as:

$$\mathcal{H} = \sum_{\boldsymbol{k}} \hbar (\omega_{\alpha' \boldsymbol{k}} \alpha'^\dagger_{\boldsymbol{k}} \alpha'_{\boldsymbol{k}} + \omega_{\beta' \boldsymbol{k}} \beta'^\dagger_{\boldsymbol{k}} \beta'_{\boldsymbol{k}}), \tag{1.18}$$

where $\alpha'^\dagger_{\boldsymbol{k}}$, $\alpha'_{\boldsymbol{k}}$, and $\beta'^\dagger_{\boldsymbol{k}}$, $\beta'_{\boldsymbol{k}}$ are the creation and destruction operators for the magnon modes α' and β' ; $\omega_{\alpha' \boldsymbol{k}}$ and $\omega_{\beta' \boldsymbol{k}}$ are the frequencies of these two magnon modes. Near the Γ point, the frequencies become:

$$\omega_{\alpha' k} \approx \frac{1}{2} \gamma H_E \, ak, \;\; \omega_{\beta' k} \approx \gamma \left(H^2 - H_c^2 + \frac{1}{4} H_E^2 \, a^2 k^2 \right)^{1/2}. \tag{1.19}$$

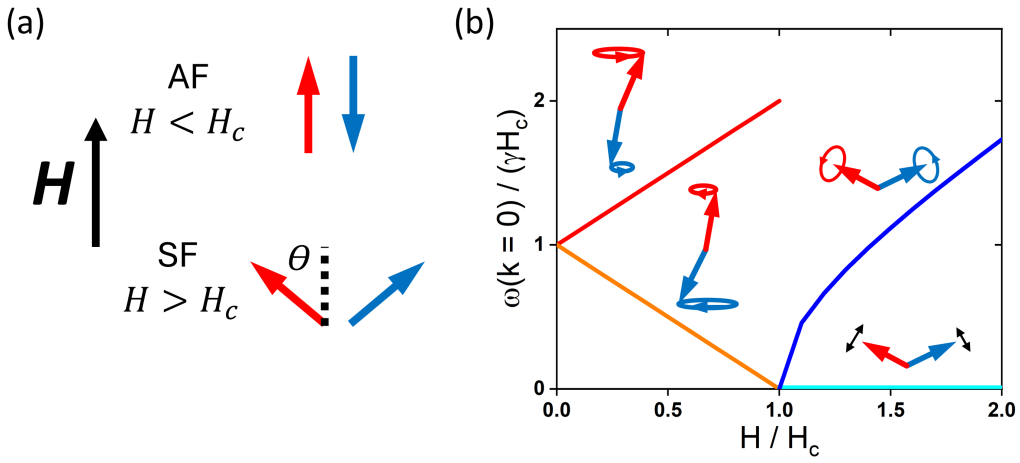

Figure 1.2 : (a) Spin configurations in the antiferromagnetic and spin-flop phases of a uniaxial antiferromagnet with the external field applied along the easy axis. The red and blue arrow represent the magnetization of the sublattices. (b) Magnon energy at $k = 0$ vs magnetic field along the easy axis of a uniaxial antiferromagnet. The inset illustrations show the precessions of the sublattice magnetizations in each magnon mode, respectively.

The frequency of the α' mode becomes independent of the field. The α' mode is characterized by both linearly polarized $\boldsymbol{l}$ and $\boldsymbol{m}$, where $\boldsymbol{l} = \boldsymbol{m}_1 - \boldsymbol{m}_2$ is the Néel vector (Fig. 1.2b). In contrast, The frequency of the β' mode increases with the field. In the β' mode, $\boldsymbol{l}$ is linearly polarized while $\boldsymbol{m}$ is elliptically polarized and precesses around $\boldsymbol{H}$ in the same sense as the α mode.

1.2.3 Other type of spin current

Since magnons can carry spin current, other quasiparticles with nonzero spin angular momentum may also transport spin current. Candidates include spin-triplet pairs in superconductors [11], spinons in quantum spin liquids [12], triplons in quantum dimerized spin systems [13] and chiral phonons in chiral insulators [14].

1.3 Spin Hall effect

The spin Hall effect (SHE) [15, 16] constitutes the conversion of a charge current into a transverse conduction-electron spin current due to strong spin-orbit coupling in the material. The inverse spin Hall effect (ISHE), the reciprocal effect, generates a transverse charge current when a conduction-electron spin current flows through the material. The charge-to-spin conversion is governed by the phenomenological parameter named as the spin Hall angle, θ_{SH}, which relates the spin and charge current densities, given by: $\boldsymbol{J}_s = \frac{2e}{\hbar}\theta_{SH}\boldsymbol{J}_c \times \boldsymbol{\sigma}$ in the SHE and $\boldsymbol{J}_c = \frac{\hbar}{2e}\theta_{SH}\boldsymbol{J}_s \times \boldsymbol{\sigma}$ in the ISHE, where $\boldsymbol{\sigma}$ is spin polarization vector.

The SHE and ISHE originate from spin-orbit interactions, which result in a spin-dependent deflection for spin-up and spin-down electrons. These effects can originate from either intrinsic or extrinsic mechanisms. The intrinsic mechanism stems from the electronic band structure of the material, where spin-orbit coupling leads to spin-dependent transverse velocities for electrons with different spin states which develops during the acceleration between scattering events. Two different extrinsic mechanisms can be distinguished: spin skew scattering, in which the spin-orbit coupling gives rise to an effective field gradient along the scattering vector, which effectively results in a spin dependence of the scattering angle; and side jump, in which the spin-orbit coupling results in an effective field gradient along the incoming and out-coming moment direction, which results upon repeated scattering in a sideway displacement.

The SHE and ISHE provide a bridge between conventional electronics and spintronics and make it possible to detect the spin current by measuring the transverse electric voltage.

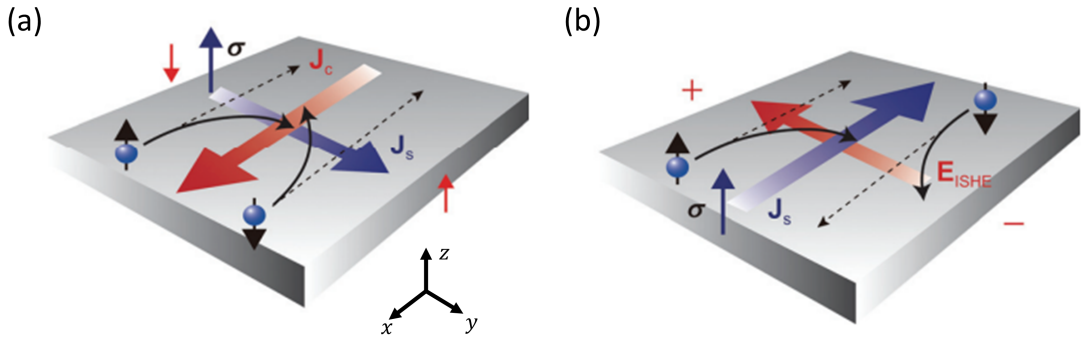

Figure 1.3 : (a) Illustration of the spin Hall effect (SHE), where a charge current J_c induces a transverse spin current J_s . Spin-down electrons are deflected to the −y direction, while spin-up electrons are deflected towards +y. Both spin species are initially moving in the −x direction. (b) Illustration of the inverse spin Hall effect (ISHE), where the spin current J_s induces a transverse charge current J_c. Spin-down electrons are initially moving in the -x direction, while spin up electrons are moving towards +x. Both spin species are deflected to the +y direction. Taken from [17].

1.4 Spin Seebeck effect

Spin Seebeck effect (SSE) [18–20] refers to the generation of a spin current from magnetic insulator (MI) into attached nonmagnetic metals under the presence of heat flow. The first SSE observation was reported in a ferromagnetic conductor $Ni_{81}Fe_{19}$ films with transverse configurations [21]. However, the transverse SSE is not free from controversy: several studies indicate that it might be due to parasitic effects coming from other magnetothermal phenomena. For this reason, many studies of the SSE rely on the longitudinal configuration, in which the spin current flows parallel to the heat current. The first longitudinal SSE was observed in ferrimagnetic insulator $Y_3Fe_5O_{12}$ (YIG) [22], in which the conduction electrons are frozen out and only magnons take part in the SSE. This opened up a new direction for studying SSE in magnetic insulators. Since this demonstration, the LSSE has been observed in various combinations of magnetic insulators. Later, a nonlocal geometry has also been used

to investigate the length scale of the SSE.

The SSE in magnetic insulators enables "insulator-based thermoelectric conversion", which was impossible if only conventional thermoelectric technologies were used. However, the present values of the SSE voltage are still far from realistic applications and various efforts are devoted not only to further understand the physics of the SSE but also to increase the magnitude of the SSE voltage.

1.4.1 Longitudinal spin Seebeck effect

The longitudinal spin Seebeck effect (LSSE) refers to the thermal generation of spin current parallel to the heat current. A basic structure for measuring the LSSE consists of a magnetic insulator (MI) / nonmagnetic metal (NM) junction system, as seen in Fig. 1.4a. Here the MI can be a slab without a substrate or a film formed on a substrate, while the NM layer must be a thin film. When a temperature gradient is applied perpendicular to MI/NM interface, a spin current is thermally injected into PM through the interfacial spin exchange interaction, i.e., spin-mixing conductance, at the MI/NM interface. The injected spin current is then converted into a measurable transverse electric voltage (SSE voltage) by means of the inverse spin Hall effect (ISHE) as a result of the spin-orbit interaction of the NM. To apply the temperature gradient perpendicular to the MI/NM interface, the device is usually sandwiched between two heat baths which are stabilized at different temperatures, or a heater is applied to one side of the sample while the other side is hold at a controlled temperature. Under this condition, a DC electric voltage difference V between the ends of the NM layer is measured. Additionally, the temperature gradient can be applied to the device also by using Joule heating in an on-chip heater (Fig. 1.4b) [23]. In this situation, we can send an ac current at angular frequency ω through

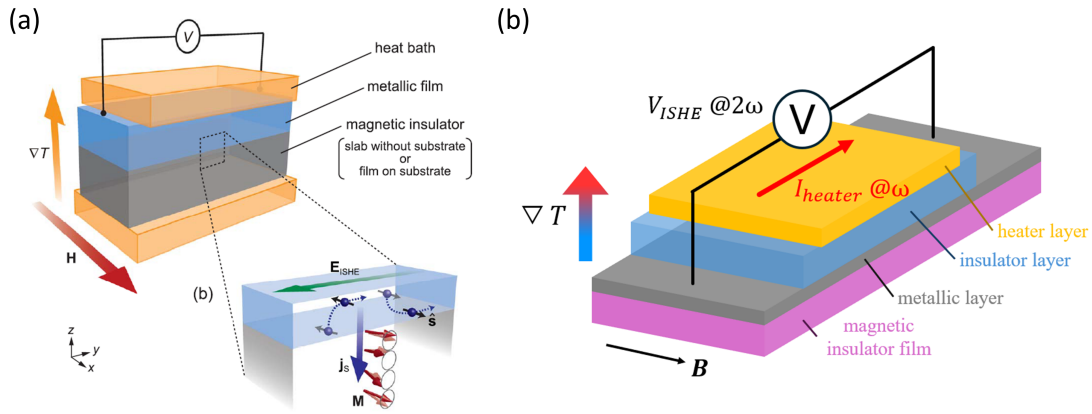

Figure 1.4 : (a) Up-left: schematic illustration of the typical experimental configuration for measuring the LSSE in a junction system comprising a metallic film and a magnetic insulator. ∇T is applied across the metal/insulator interface by sandwiching the LSSE device between two heat baths with different temperatures. Down-right: schematic illustration of the ISHE induced by the LSSE. Taken from [19]. (b) schematic of spin Seebeck device using an on-chip heater.

the on-chip heater, which generates a heat current flowing into the MI/NM junction with an ac component at 2ω. This heat current drives a spin current at 2ω, which is then converted into a transverse voltage at 2ω by ISHE. Thus the SSE voltage is measured at the second harmonic frequency with a lock-in amplifier, which can detect the response as small as several nanovolts. All the experiments in this thesis were performed in this setup.

The first observation of the longitudinal spin Seebeck effect (LSSE) was reported in ferrimagnetic insulator $Y_3Fe_5O_{12}$ (YIG) [22]. Since Pt and YIG enable efficient spin-charge conversion and pure detection of spin-current effects, respectively, the Pt/YIG junction is recognized as a model system for studying SSE physics. A number of experiments have been conducted using YIG and YIG/Pt systems to reveal the physics behind SSE. Reports include temperature dependence [24–29], field dependence [25–27, 30, 31], YIG thickness dependence [25–27, 29, 32], separation with

other thermoelectric and spin-current effects [33–37] and quantitative estimation of SSE thermoelectric coefficient [38, 39].

Meanwhile, LSSE are also reported in other materials, such as ferrimagnet Fe_3O_4 [23, 40], multiferroic $CoCr_2O_4$ [41], van der Waals ferromagnet $CrSiTe_3$ and $CrGeTe_3$ [42] and compensated ferrimagnet $Gd_3Fe_5O_{12}$ (GdIG) [43–47].

Since 2015, LSSE has been reported for various antiferromagnetic insulators (AFIs), including easy-axis AFIs Cr_2O_3 [48–53], MnF_2 [54], FeF_2 [55], α-Fe_2O_3 [50]; polar AFI α-$Cu_2V_2O_7$ [56]; easy-plane AFI NiO [57–59]; $SrFeO_3$ [60]; $DyFeO_3$ [61]; $SrMnO_3$ [62]; noncollinear AFI $LuFeO_3$ [63, 64]; 3D Heisenberg AFI $RbMnF_3$ [65]; Berezinskii-Kosterlitz-Thouless candidate AFI $BaNi_2V_2O_8$ [66]; van de Waals AFI $CrPS_4$ [67], showing the versatility of the SSE to investigate AF spin dynamics. There is, however, still debate on the field response for easy-axis AFIs below the spin-flop field. Seki *et al.* didn't observe any detectable signal in Cr_2O_3/Pt [48], whereas Wu *et al.* observed a ferromagnetic (positive) sign in MnF_2 [54]. Li *et al.* reported a negative sign for Cr_2O_3/Pt and α-Fe_2O_3/Pt in its easy-axis AF phase, which is consistent with the spin polarization carried by the low-frequency mode. Li *et al.* further showed that the SSE sign changes from negative to positive when the surface of Cr_2O_3 is etched before Pt deposition. This result may be interpreted in terms of the appearance of uncompensated magnetic moments at the interface that contribute to the positive ferromagnetic-like SSE signal through modification of the interfacial spin-mixing conductance or generation of an additional spin current.

The paramagnetic LSSE was first observed in $Gd_3Ga_5O_{12}$ (GGG), a geometrically frustrated magnetic insulator, and $DyScO_3$ at temperatures above its Néel temperature of 3.1 K [68], where conventional magnon theory fails. In GGG, short-range order and field-induced long-range correlations [69] are thought to contribute to the

SSE, despite the lack of long-range order. Later, paramagnetic SSE was observed in the paramagnetic phase of ferromagnets above its Curie temperature T_C (e.g., $CoCr_2O_4$ [41], and $CrSiTe_3$ and $CrGeTe_3$ [42]) and antiferromagnets above its Néel temperatrue T_N (e.g., FeF_2 [55], $RbMnF_3$ [65]). The SSE from paramagnets was also found in the one-dimensional (1D) quantum spin liquid (QSL) system Sr_2CuO_3 [70,71] and the spin-Peierls system $CuGeO_3$ [72], associated with the thermal generation of exotic spin excitations, such as spinons in the 1D QSL and mobile triplets (triplons) in the spin-Peierls system, respectively. Additionally, the spin-gapped quantum magnet $Pb_2V_3O_9$, showed SSE at low temperatures, with a peak behavior near the critical field for the Bose–Einstein condensation of triplons [73].

1.4.2 Nonlocal spin Seebeck effect

The experiment geometry of the nonlocal spin Seebeck effect (nlSSE) measurements is shown in Fig. 1.5a. When a charge current I is sent through the heater, the heater wire heats up and induces a radial thermal gradient in the MI, which drives a magnon spin current away from the heater. Magnons are driven away from the heater, towards the bottom of the MI film and will eventually diffuse to the detector, where a voltage V is generated by ISHE. Signal generation in the nonlocal SSE is a complex process, since both thermally-driven and diffusion magnon spin currents are at play. Both sign and magnitude of the signal depend sensitively on temperature, the MI film thickness, the injector-detector distance and the relative transparency to spin currents of the NM/MI interface compared to that of the MI bulk.

The nlSSE was first observed in the ferrimagnetic insulator $Y_3Fe_5O_{12}$ (YIG) by Cornelissen *et al.*, where the magnon diffusion length is found to be several micrometers at room temperature [74]. Later, the same group observed a signal reversal of

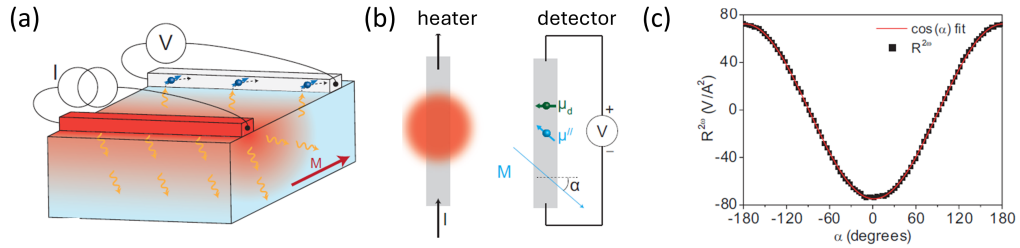

Figure 1.5 : (a) Schematic representation of the experimental geometry. Joule heating due to the current I in the heater generates a radial temperature gradient in the magnetic insulator, and via SSE, it drives a magnon spin current away from the heater. The magnons ultimately diffuse to the detector, where they are absorbed and generate a voltage V. (b) Schematic illustration of the angular dependence of nonlocal SSE voltage: At the heater, Joule heating excites magnons thermally, which diffuse to the detector. This process is independent of α. At the detector, the excited magnons generate a spin accumulation $\mu_{\parallel}$ anti-parallel to the magnetization $\boldsymbol{M}$. Due to the inverse spin Hall effect, $\mu_{\parallel}$ generates a charge voltage, of which we detect the component generated by μ_d. This gives rise to a $\cos\alpha$ dependence of the detected magnon current. The total signal is a product of the effects at the heater and detector, leading to the $\cos\alpha$ dependence. (c) The nonlocal SSE signal with a $\cos\alpha$ fit. Adapted from [74].

nlSSE in YIG which occurs at a certain heater-distance and is influenced by both the opacity of the YIG/heater interface and the YIG thickness [75]. Since the nlSSE allows for the extraction of the magnon relaxation length in a magnetic material [76], the field and temperature dependences of the magnon diffusion length in YIG were investigated in the nonlocal geometry [77, 78]. At low temperatures ($T < 20$ K) with increasing I, the nlSSE shows a nonlinear power dependence, at which the B-induced signal reduction becomes less visible, suggesting that in the nonlinear regime, high-energy magnons are overpopulated compared to those expected from the thermal energy [79].

This nonlocal approach to examine the SSE has been applied to different magnetic systems, including ferrimagnet $NiFe_2O_4$ [80, 81], $Tm_3Fe_5O_{12}$ [82]; easy-axis antiferro-

magnet Cr_2O_3 [83, 84]), α-Fe_2O_3 [85, 86]; easy-plane antiferromagnet NiO [87]; van der Waals antiferromagnet $MnPS_3$ [88, 89], $CrBr_3$ [90]; and multiferroic $BiFeO_3$ [91].

1.4.3 Applications

The spin Seebeck effect can be used as a sensitive probe for elementary spin-carrying excitations, spin correlation, transport and associated scattering rates, static magnetic and Néel order, and domain in solids [19]. This unique feature is realized because both the interfacial spin-current injection and bulk spin transport play essential roles in SSE, unlike other conventional spintronic phenomena that appear only in a nanoscale, highlighting the power of SSE.

The spin Seebeck effect also attracted attention due to possible future thermoelectric applications. A suggested application is the so called spin-thermoelectric coating [92], consisting of a metal/MI bilayer film directly coated on a heat source. Due to the simple structure and straightforward scaling law of the LSSE, the spin-thermoelectric coating is potentially applicable to the implementation of large-area thermoelectric devices onto various-shaped heat sources, such as the surfaces of electronic instruments and automobile bodies. Another possible application is to use the nonlocal SSE to transport information in the magnetoelectric, spin-orbit coupled (MESO) logic device [93].

1.5 Theory of longitudinal spin Seebeck effect

1.5.1 Inverse spin Hall voltage from injected spin current in nonmagnetic metal

Consider a nonmagnetic metal (NM) layer with length l_{NM}, width w_{NM} and thickness t_{NM}. The spin current with density $J_s(0^+)$ is injected at $z = 0$, creates finite spin accumulation μ_{NM}, and then diffuses to flow in NM. The μ_{NM} follows the diffusion equation:

$$\nabla^2 \mu_{NM} = \frac{\mu_{NM}}{\lambda_{NM}^2}, \tag{1.20}$$

where λ_{NM} is the spin diffusion length in NM. The general solution for λ_{NM} is written as $\lambda_{NM}(z) = ae^{-z/\lambda_{NM}} + be^{z/\lambda_{NM}}$. With the boundary conditions:

$$\left.\frac{\mathrm{d}\mu_{NM}}{\mathrm{d}z}\right|_{z=0} = J_s(0^+), \quad \left.\frac{\mathrm{d}\mu_{NM}}{\mathrm{d}z}\right|_{z=t_{NM}} = 0, \tag{1.21}$$

we can obtain

$$j_{s,NM}(z) = J_s(0^+)\frac{e^{-z/\lambda_{NM}} - e^{(z-2t_{NM})/\lambda_{NM}}}{1 - e^{-2t_{NM}/\lambda_{NM}}}. \tag{1.22}$$

Due to the ISHE in NM, $j_{s,NM}(z)$ generates an electric field $\boldsymbol{E}_{ISHE}$ given by $E_{ISHE} = (2e/\hbar)\theta_{SH}\rho_{NM}\langle j_{s,NM}(z)\rangle$, where θ_{SH} is the spin Hall angle of NM, ρ_{NM} is the resistivity of NM, and $\langle j_{s,NM}(z)\rangle = (1/t_{NM})\int_0^{t_{NM}} j_{s,NM}(z)\,\mathrm{d}z$ is the average of $j_{s,NM}(z)$. Then the ISHE voltage $V_{ISHE} = E_{ISHE}l_{NM}$ becomes:

$$V_{ISHE} = R_{NM}w\lambda_{NM}\frac{2e}{\hbar}\theta_{SH}\tanh\left(\frac{t_{NM}}{2\lambda_{NM}}\right)J_s(0^+), \tag{1.23}$$

where $R_{NM} = \rho_{NM}\dfrac{l_{NM}}{w_{NM}t_{NM}}$ is the resistance of the NM layer. Eqn. 1.23 holds for all the spin Seebeck theory.

1.5.2 Spin current density at the interface

Now we deal with the spin current density at the MI/NM interface $J_s(0^+)$. Depending on the magnetic properties of MI and theoretical considerations, $J_s(0^+)$ has different forms. Generally, theorists consider that the SSE has two contributions: from the MI/NM interfacial temperature difference and from the bulk temperature gradient in the MI.

In the interfacial temperature difference model for ferromagnetic SSE [94], the SSE is explained as a result of the thermal nonequilibrium between the magnon system in ferromagnetic insulator (FMI) and electron systems in nonmagnetic metal (NM). The total spin current at the FMI/NM interface is given by the difference between the spin-pumping and backflow components, which is proportional to the difference between the effective magnon and electron temperatures:

$$\boldsymbol{J}_s(0^+) = \boldsymbol{J}_{sp} - \boldsymbol{J}_{bf} \quad \propto \quad T_{M,FMI} - T_{e,NM}, \tag{1.24}$$

If an external temperature gradient is applied to FMI, an effective magnon-electron temperature difference is induced, and a spin current is generated across the FMI/NM interface.

In the magnon bulk transport model for ferromagnetic SSE [95], the SSE is formulated in terms of a bulk magnon spin current thermally induced in the FMI, not at the FMI/NM interface. When a temperature gradient $\boldsymbol{\nabla} T$ is applied to the FMI, a number of magnons are excited out of thermal equilibrium. Then the magnon spin current in the FMI layer can be written as:

$$\boldsymbol{J}_s = \frac{\hbar}{(2\pi)^3} \int \mathrm{d}^3\boldsymbol{k}\, \boldsymbol{v}_{\boldsymbol{k}} (n_{\boldsymbol{k}} - n^0_{\boldsymbol{k}}), \tag{1.25}$$

where $n_{\boldsymbol{k}}$ the number of magnons with wave number $\boldsymbol{k}$ and energy $\hbar\omega_{\boldsymbol{k}}$ in the whole volume V of the FMI layer; $n^0_{\boldsymbol{k}}$ is the number in thermal equilibrium, given by the

Bose-Einstein distribution, $n_{\boldsymbol{k}}^0 = 1/[\exp(\hbar\omega_{\boldsymbol{k}}/k_BT) - 1]$; $\boldsymbol{v}_{\boldsymbol{k}}$ is the $\boldsymbol{k}$-magnon velocity. Then using the Boltzmann transport equation, the magnon distribution can be calculated. Considering the boundary conditions in the FMI/NM structure, the magnon spin current density at the FMI/NM interface can be described as:

$$\boldsymbol{J}_s(0^+) = -F_{FMI}\,\rho\, g_{eff}^{\uparrow\downarrow} \boldsymbol{\nabla} T, \tag{1.26}$$

where F_{FMI} is a prefactor dependent on FMI material parameters; $\rho = \dfrac{\cosh(t_{FM}/\lambda_m) - 1}{\sinh(t_{FM}/\lambda_m)}$ describes the effect of the FMI layer thickness t_{FM} with respect the magnon diffusion length in FMI λ_m; and $g_{eff}^{\uparrow\downarrow}$ is the real-part of effective spin mixing conductance, which originates from microscopic exchange interactions at the NM/MI interface between the conduction electrons in the NM and the magnetic moments in the MI. Eqn. 1.26 is used to explain a variety of experimental results of the SSE, such as the dependence on the FMI thickness [25, 27, 32] and SSE suppression at high magnetic fields [25].

Eqn. 1.26 considers that the spin current is entirely produced by the thermal excitation of magnons in the FMI. However, it cannot readily explain the strong enhancement of the SSE observed at low temperatures. Now consider a phonon drag mechanism [96], in which phonons in the heat current generate a spin current by means of magnon-phonon interaction, then the magnon spin current can be written as:

$$\boldsymbol{J}_s(0^+) = -F_{FMI}{}'\,\rho\, g_{eff}^{\uparrow\downarrow}\, \kappa_{th} \boldsymbol{\nabla} T, \tag{1.27}$$

where κ_{th} is the thermal conductivity of the FMI and $F_{FMI}{}'$ is another prefactor different from F_{FMI} in Eqn. 1.26, since $F_{FMI}{}'$ includes magnon-phonon coupling. Eqn. 1.27 provides results for the temperature dependence of the SSE that are in quite good agreement with the experimental data in [28].

Now let's turn to antiferromagnetic insulator (AFI). The two-sublattice AFI has

two magnon modes with opposite chirality, so Eqn. 1.26 should be generalized to include these two magnon modes. With the similar treatments, the magnon spin current can be written as [97, 98]:

$$\boldsymbol{J}_s(0^+) = C_{AFI}\rho g_{eff}^{\uparrow\downarrow} S_{AFI} \boldsymbol{\nabla} T, \tag{1.28}$$

where C_{AFI} is a prefactor dependent on AFI material parameters, and

$$S_{AFI} = \frac{\hbar^2}{6\pi^2 k_B T^2} \int \mathrm{d}k k^2 v_{mk}^2 \left[\frac{e^{\hbar\omega_{\beta k}/k_B T}\omega_{\beta k}}{\eta_{\beta k}(e^{\hbar\omega_{\beta k}/k_B T}-1)^2} - \frac{e^{\hbar\omega_{\alpha k}/k_B T}\omega_{\alpha k}}{\eta_{\alpha k}(e^{\hbar\omega_{\alpha k}/k_B T}-1)^2} \right], \tag{1.29}$$

where $\hbar\omega_{\mu k}$, $\boldsymbol{v}_{mk}$, $\eta_{\mu k}$ is the energy, group velocity and relaxation rate of the μk magnon ($\mu = \alpha$ or β). In a uniaxial AFI, Eqn. 1.28 shows that the spin current vanishes for $H = 0$ because the two modes have the same occupancy; and for H smaller than the spin-flop field H_{SF}, the SSE signal has the opposite sign to the signal in ferromagnets, as the lowest magnon mode has polarization along the external field.

Reitz *et al.* [99] extended the SSE in the easy-axis AFIs to the spin-flop phase. They found that below the spin-flop field, there are two spin carriers with opposite magnetic moments, with the carriers polarized along the field forming a majority magnon band; above spin-flop field, the low-energy, ferromagnetic-like mode has magnetic moment opposite the field; this results in a sign change of the SSE across the spin-flop transition.

Yamamoto *et al.* [100] developed a theory of the spin Seebeck effect (SSE) in paramagnets as well as in antiferromagnets at elevated temperatures where the classical limit of the fluctuation-dissipation theorem is applicable. Employing dissipative stochastic models, the spin current at the MI/NM interface, for both PM and AFM, is proportional to the spin susceptibility of the MI, multiplied by the external magnetic field. It concludes that in this limit, one would expect the same sign for both the paramagnetic and antiferromagnetic SSEs, also equal to the SSE in a ferromagnet.

Later, Yamamoto *et al.* [101] used a stochastic Ginzburg-Landau simulation and demonstrated that a sign reversal of the antiferromagnetic SSE across the spin-flop transition occurs when the interfacial coupling of conduction electron spin $\boldsymbol{s}$ in the NM to the staggered magnetization $\boldsymbol{n}$ of the AFI dominates; whereas no sign reversal appears when the interfacial coupling of $\boldsymbol{s}$ to the magnetization $\boldsymbol{m}$ dominates. Moreover, the sign reversal is influenced by the degree of spin dephasing in the NM layer.

Oyanagi *et al.* [102] developed a general theoretical model of the paramagnetic SSE based on the interfacial temperature difference between localized spin in the paramagnetic insulator (PI) and the conduction-electron spin in the normal metal (NM). Through a linear response approach, the interfacial spin current can be written as:

$$J_s(0^+) = -S_{SSE} k_B \Delta T, \tag{1.30}$$

where $\Delta T = T_{NM} - T_{PI} \ll T_{PI}$, and S_{SSE} is the spin Seebeck coefficient:

$$S_{SSE} = \frac{\hbar}{2e^2} \frac{g\mu_B B}{k_B T} \frac{2g_s}{1 + 2\rho_{NM}\lambda_{NM} g_s \coth\left(t_{NM}/\lambda_{NM}\right)}, \tag{1.31}$$

with the effective spin conductance:

$$g_s = 2\pi \frac{2e^2}{\hbar} n_{PI} J_{int}^2 S B_S \left(\frac{g\mu_B B}{k_B T}\right) \left[\frac{(g\mu_B B/2k_B T)}{\sinh^2\left(g\mu_B B/2k_B T\right)}\right], \tag{1.32}$$

where n_{PI} is the interfical spin density, J_{int} is interfacial exchange interaction, B_S is the Brillouin function of spin S as a function of dimensionless ratio of the Zeeman energy to the thermal energy. Eqn. 1.30 holds for small temperature difference ($T_{NM}/T_{PI} \sim 1$) and small spin conductance condition ($\rho_{NM}\lambda_{NM} g_s \ll 1$), which is always satisfied at low temperatures. This model qualitatively reproduces the field-induced reduction of the SSE observed at high fields and low temperatures in the Pt/GGG system.

Reitz *et al.* [103] used Schwinger boson mean-field theory (SBMFT) to evaluate the spin Seebeck effect in FMs and AFMs and found that well below the ordering temperature, J_s is dominated by a magnonic contribution, reproducing the behavior of a dilute-magnon gas; near the transition temperature, an additional paramagnetic-like contribution becomes significant. In the AFM, the two contributions come with opposite signs, resulting in a signature, rapid inversion of the spin Seebeck coefficient as a function of temperature.

Chapter 2

Fabrication Techniques and Experimental Methods

In this chapter, we will summarize and discuss the device fabrication techniques and experimental methods employed throughout the researches presented in the subsequent chapters.

2.1 Fabrication techniques

To fabricate a typical SSE device, it involves multiple layers build-up, each layer consisting of pattern lithography, material deposition and the liftoff.

2.1.1 Lithography

Lithography is the process of transferring a pattern into a reactive polymer film, known as a resist, which is subsequently used to replicate that pattern onto an underlying substrate [104, 105]. Depending on the type of energetic radiation used to expose the resist, lithography can be broadly categorized into three main types: e-beam lithography, photolithography, and focused-ion-beam lithography.

E-beam lithography (EBL) employs a focused beam of high-energy electrons to directly write arbitrary patterns onto a resist-coated substrate. The electron beam modifies the solubility of the resist, enabling selective removal of either the exposed or unexposed regions of the resist. Due to the sub-nanometer beam diameter, EBL offers extremely high resolution, with feature sizes as small as 1 nm. The EBL process consists of three main steps: resist coating, exposure and development.

- Resist coating: In our laboratory, the positive-tone EBL resist MicroChem PMMA (polymethylmethacrylate) with molecular weights of 495k and 950k are used. For PMMA 495k, the resist is spin-coated at 3000 rpm (revolutions per minute) for 40 seconds and then baked on a hot plate at 210 °C for 60 seconds. For PMMA 905k, the resist is spun at 4000 rpm for 60 seconds and then baked at 220 °C for 60 seconds. A bilayer PMMA structure (spinning 495k first, followed by 950k) facilitates a clean and reliable liftoff process.

- Exposure: An Elionix ELS-G100 system is used to write the pattern onto the resist layer, operating at an acceleration voltage of 100 kV. The dose required for exposure depends on the substrate material. For PMMA 495k on silicon wafer, an area dose of 800 μCcm^{-2} is typically used. For bilayer PMMA on silicon wafer, VO_2 film on sapphire, and V_2O_3 film on sapphire, an area dose of 2,000 μCcm^{-2} is typically used,

- Development: Following the exposure, the sample is developed in a solution of isopropanol and methyl-isobutyl-ketone (IPA:MIBK) with a volume ratio of 3:1 for 60 seconds to dissolve the exposed parts of the PMMA layer. The development process is quenched by rinsing in IPA for another 30 seconds, followed by nitrogen blow-drying to prevent the formation of organic residues. Prior to the deposition, a 30-second low-power argon plasma cleaning is applied to clean off any remaining organic contaminants.

Photolithography, instead, uses light to expose the resist. While the minimum feature size achievable (typically 0.5 μm) is larger than that of EBL, photolithography enables rapid patterning over large areas, offering significantly higher throughput and yield.

In our lab, the positive photoresists Shipley Microposit S1813 and S1818 are commonly used. The photoresist is spin-coated at 5,000 rpm for 60 seconds and baked at 115 °C for 60 seconds. The exposure is carried out using a Bruker SF-100 Lightning Maskless Photolithography System, equipped with a 405 nm light source and two objectives (4x and 20x). For silicon substrates, the typical exposure time is 9.5 seconds with the 4x objective and 0.38 seconds with the 20x objective. After exposure, the sample is developed in Shipley Microposit MF-321 or MF-319 developer solution for 1 minute, followed by a rinse in the deionized water and nitrogen blow-drying.

2.1.2 Deposition

Deposition is a fundamental process in nanofabrication used to form thin films of materials on a substrate [106]. It involves the controlled transfer of atoms from a source to the surface of a target substrate, where they condense to form a uniform layer. Depending on the energy source and material transport mechanism, deposition techniques can be categorized into several types, including e-beam evaporation, magnetron sputtering, and chemical vapor deposition.

E-beam evaporation is a widely used technique for preparing high-purity thin films. During the evaporation process, the target material is heated by a focused high-energy electron beam and transformed into the gaseous phase. Under the low chamber pressure of 10^{-5} mbar or lower, the vaporized atoms travel with minimal scattering and condense onto the substrate surface. By precisely controlling the evaporation rate, film thickness can be accurately managed, ensuring tight tolerances. We use an e-beam evaporator to deposit SiO_x insulating layer and Ti/Au metal contacts in our experiments.

Magnetron sputtering, instead, utilizes energetic ions, typically Ar^+ ions, generated in a low-pressure argon plasma, to bombard the target. The impact ejects atoms from the target surface through momentum transfer, which then deposit onto the substrate. To enhance the sputtering efficiency and obtain a high deposition rate, a magnetic field is applied near the target to confine electrons in a closed-loop path, increasing plasma density. We use an AJA ATC Orion Sputtering System to deposit Pt, W, and Ti/Au layer in our experiments.

2.1.3 Liftoff

After deposition, the sample is immersed in acetone for at least 1 hour to dissolve the resist layer. As a result, the metal deposited on top of the resist is lifted off, while the metal deposited in the exposed areas (i.e. directly in contact with the substrate) remains, hence the pattern is effectively transferred from the mask onto the substrate. If necessary, a brief low-power ultrasonication step (typically 5-10 seconds) can be performed to remove any metallic residues on the surface. The sample is then rinsed sequentially with acetone and isopronanol, and finally blow dried with nitrogen.

2.2 Experimental methods

The typical spin Seebeck voltage across the detector wire has a magnitude of several microvolts, which is considerably smaller compared to the applied ac voltage on the heater wire of several volts. To detect such a small signal and improve the signal-to-noise ratio, we use a lock-in detection technique [107].

2.2.1 Principle of the lock-in amplifiers

In order to understand how a lock-amplifier works, let's first review the product of two harmonic signals. The following mathematical identity holds for the product of two harmonic functions at two different frequencies:

$$\begin{aligned} & A\cos(\omega_1 t+\varphi)\times B\cos(\omega_2 t) \\ & \quad =\frac{1}{2}AB\left\{\cos\left[(\omega_1+\omega_2)t+\varphi\right]+\cos\left[(\omega_1-\omega_2)t+\varphi\right]\right\}, \end{aligned} \tag{2.1}$$

where A and B are the amplitudes of two harmonic signals; ω_1 and ω_2 are the corresponding angular frequencies; and φ is the phase difference between the two harmonic signals.

If $\omega_1=\omega_2=\omega$, the first cos term results in a harmonic signal with frequency 2ω. The second cos term containing the frequency difference results in a DC component. If $\omega_1\neq\omega_2$, the product of the two harmonic signals can be written as the sum of two harmonic signals oscillating with the sum and the difference of ω_1 and ω_2. In this case, the product signal has no DC component.

In the long-time average or with a low-pass filter, only the DC component remains as:

$$\lim_{T\to\infty}\frac{1}{T}\int_0^T A\cos(\omega_1 t+\varphi)\times B\cos(\omega_2 t)\,\mathrm{d}t=\frac{1}{2}AB\cos\varphi\times\mathbf{1}_{\{0\}}(\omega_1-\omega_2), \tag{2.2}$$

where $\mathbf{1}_{\{0\}}(x)$ is an indicator function, which equals 1 when $x=0$ and 0 otherwise. For the case $\omega_1\neq\omega_2$, the time averaging results in the signal vanishing completely. For the case $\omega_1=\omega_2$, the time averaging filters out just the DC component of the product signal $\frac{1}{2}AB\cos\varphi$, which is proportional to the signal amplitudes A and B. Additionally, the result is related to the phase difference between two signals. Due to this, the lock-in technique is also called phase-sensitive detection [107].

Now, let signal A be the signal to measure and signal B the reference signal. We can manipulate the frequency of the reference signal ω_{ref}, then, after time averaging, all (noise) frequency components with $\omega_s \neq \omega_{ref}$ are filtered out, and only the frequency component with $\omega_s = \omega_{ref}$ survives. Since we know the amplitude and phase of the reference signal, we can extract $A\cos\varphi$. In this way, we successfully extract the useful information from the noisy environment.

The absolute value of the amplitude and the phase can also be measured simultaneously. In one channel (called channel X), the usual measurement is performed; while in the another channel (called channel Y), phase of the reference signal is shifted additionally by 90°. If we neglect the constant factor $\frac{1}{2}B$, this results in $X = A\cos\varphi$ and $Y = A\cos(\varphi - \pi/2)$. The absolute value of the amplitude A and the phase difference φ can be determined from the measured values X and Y as $A = \sqrt{X^2 + Y^2}$ and $\varphi = \arctan(Y/X)$.

2.2.2 Applications to SSE measurements

By applying an ac current $I(t) = \sqrt{2}I_0 \sin(\omega t)$, the generated voltage V(t) can be written as the sum of first-, second-, and higher-order current responses as:

$$V(t) = R_1 I(t) + R_2 I^2(t) + R_3 I^3(t) + R_4 I^4(t) + \cdots, \tag{2.3}$$

where R_n is the nth-order response of the measured system to the applied current $I(t)$.

With the use of lock-in detection, we let the reference signal proportional to $\sin(n\omega t + \varphi)$, to extract the ω, 2ω, 3ω, ... components in the generated voltage $V(t)$.

The detected nth-harmonic signal is defined as:

$$V_n(t) = \frac{\sqrt{2}}{T}\int_{t-T}^{t} \sin(n\omega s + \varphi)V(s)\,\mathrm{d}s, \tag{2.4}$$

where $T = 2\pi/\omega$ is the period of the current $I(t)$.

Assuming the voltage response up to the fourth order, the following lock-in voltages are calculated:

$$V_1 = R_1 I_0 + \frac{3}{2} R_3 I_0^3 \text{ for } \varphi = 0°, \tag{2.5}$$

$$V_2 = \frac{1}{\sqrt{2}}(R_2 I_0^2 + 2R_4 I_0^4) \text{ for } \varphi = -90°, \tag{2.6}$$

$$V_3 = -\frac{1}{2} R_3 I_0^3 \text{ for } \varphi = 0°, \tag{2.7}$$

$$V_4 = -\frac{1}{2\sqrt{2}} R_4 I_0^4 \text{ for } \varphi = -90°, \tag{2.8}$$

So using lock-in amplifiers to measure the first-, second-, third-, and the fourth-harmonic voltage responses, R_n can be deduced. Note that V_1 (V_2) does not purely scale linearly (quadratically) with I_0. A third (fourth) order current dependence is also present in the measured voltage response. However, in the following chapters we only present the V_2, assuming that $R_4 I_0^2 \ll R_2$. Its validity can be seen from the power dependence of the V_2 signal. The measured V_2 is linearly dependent on the heater power, which is proportional to I_0^2, indicating the R_2 term dominates.

2.2.3 Circuit schematic

During the entire measurement process, both the resistances of the metal wires and the spin Seebeck effect (SSE) signals are measured on the same device. These measurements require distinct circuit configurations.

Fig.2.1a illustrates the typical circuit diagram used for the resistance measurements. A function generator (Stanford Research Systems Model DS345) sends out a sinusoid signal, which passes through the device under test (DUT) in series with a protective resistance R_o. The resulting current is first amplified by a low-noise current preamplifier (Model SR570) and then sent to a Signal Recovery 7265 DSP amplifier.

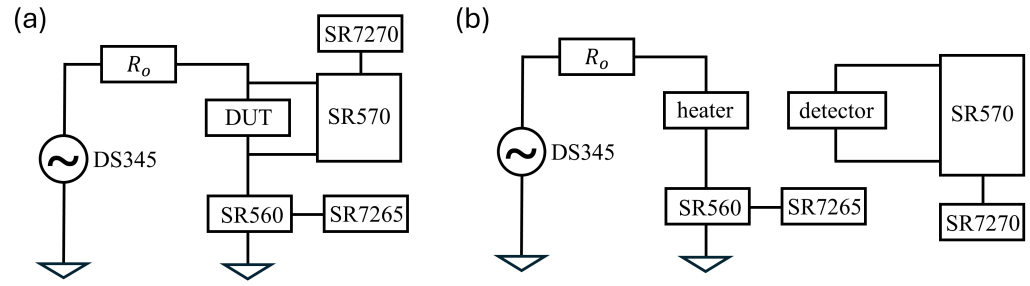

Figure 2.1 : Circuit diagram for (a) the resistance measurements and (b) the SSE measurements.

Simultaneously, the voltage across the DUT is first amplified by a low-noise voltage preamplifier (Model SR560) and then measured by a Signal Recovery 7270 DSP amplifier. The excitation frequency is set to 137.7 Hz, and the time constant for both DSP amplifiers is set to 200 ms.

Fig.2.1b shows the circuit used for the SSE measurements. The DS345 serves as a function generator, driving a current through the heater wire in series with the protective resistor R_o. The voltage across the detector wire is amplified by SR560 and recorded by the SR7270. In this configuration, the SR7270 operates in dual harmonic mode, allowing it to simultaneously detect signals at the first and second harmonics of the reference frequency. The excitation frequency is set to 7.7 Hz, and the time constant for both DSP amplifier is set to 2 s. Special attention must be paid to phase calibration in the SSE measurements. Unlike the resistance measurements, where the current and voltage paths are directly linked, the heater and the detector in the SSE configuration are ideally electrically isolated. As a result, no or little X channel of the first harmonic signal is expected. The nonlinear capacitive or inductive couplings could contribute to the second harmonic signal. For example, assume $U(t) = \dfrac{\mathrm{d}(L(I(t)) \cdot I(t))}{\mathrm{d}t}$ with $I(t) = I_0 e^{\mathrm{i}\omega t}$, then

$U = \frac{\mathrm{d}L(I)}{\mathrm{d}I}\frac{\mathrm{d}I}{\mathrm{d}t}I + L(I)\frac{\mathrm{d}I}{\mathrm{d}t} = \mathrm{i}\omega I_0^2\frac{\mathrm{d}L}{\mathrm{d}I}e^{\mathrm{i}2\omega t} + \mathrm{i}\omega L I_0 e^{\mathrm{i}\omega t}$. However, these effects are expected to be small ordinarily. The standard procedure for phase calibration in practice is as follows: 1) Temporarily connect the detector wire in the resistance measurement circuit. Adjust the phase so that the Y channel of the first harmonic signal is zero. This phase shift is denoted as ϕ. (It can be conveniently done using the "Auto Phase" function in the SR7270.) 2) In the SSE measurement circuits, maintain the phase shift ϕ for the first harmonic mode and set the phase shift in the second harmonic mode to 2ϕ. This procedure ensures accurate extraction of both first and second harmonic components in SSE measurements.

Chapter 3

Nonlocal Spin Seebeck Effect at Low Temperatures in the Nominally Paramagnetic Insulating State of Vanadium Dioxide

This chapter will mainly show a nonlocal spin Seebeck (nlSSE) response in vanadium dioxide (VO_2) films at low temperatures deep in the insulating regime. Given the expected nature of paramagnetism in VO_2, this observation is surprising. For a fully spin dimerized system, paramagnetic response is expected to be suppressed at low temperatures, unlike, e.g., a classical spin liquid (such as gadolinium gallium garnet). The "local" paramagnetism, as in the van Vleck mechanism, is expected to be temperature independent, not expected to transport angular momentum and thus should not contribute to the SSE response. The nlSSE is non-hysteretic as a function of field and has the expected dependence on orientation of magnetic field in-plane. With the field in-plane, the SSE signal grows in magnitude with decreasing temperature below an onset of detectability at approximately 30 K, with a sign inversion between 15 K and 10 K. This chapter is adapted with permission from *Applied Physics Letters*. See Ref [108].

3.1 Device fabrication and experimental setup

Vanadium dioxide is an archetypal strongly correlated transition metal oxide [109, 110], with a phase transition at $\sim$ 345 K in bulk between a high temperature, rutile metallic phase with one-dimensional vanadium atom chains and a low temperature,

monoclinic insulating phase with dimerized vanadium atoms. The vanadium dimers are thought to form singlets [111, 112], greatly reducing the magnetic response of the VO_2 at low temperatures. The local paramagnetism, as in the van Vleck mechanism, is expected to be temperature independent. However, the measured susceptibility in the insulating state shows a significant temperature dependence, which is proportional to $T^{-2/3}$ [111].

The $\sim$ 100 nm thick epitaxial VO_2 film was grown by reactive sputtering on top of an Al_2O_3 substrate (r-cut). A 4-mtorr argon/oxygen mix (8% O_2) was used during deposition, and the substrate was kept at 520 °C during the growth and later cooled down at a rate of 12 °C/min. X-ray diffraction measurements confirmed single-phase growth, textured along (100) for VO_2. Transport measurements were carried out on a TTPX Lakeshore cryogenic probe station, using a Keithley 6221 current source and a Keithley 2182A nanovoltmeter. The films exhibit a large, hysteretic metal-insulator transition (Fig. 3.1c), as expected for high-quality films. Electron beam lithography and magnetron sputtering are used to prepare Pt nanowires (100 μm long, 200 nm wide, 20 nm thick, separated by 400 nm) on the VO_2 surface for the nonlocal SSE measurements, as shown in Fig. 3.1b. Typical resistance of each wire is 18 - 20 kΩ. Measurements are performed as a function of temperature and field in a Quantum Design Physical Property Measurement System (PPMS) equipped with a rotation stage.

In the nlSSE measurement configuration (Fig. 3.1a), an AC heater current at angular frequency $\omega = 2\pi \times$ (7.7 Hz) is driven through a Pt wire, while the voltage across the other wire is measured at ω and 2ω using a lock-in amplifier. The dominant signal at ω is due to capacitive coupling between the wires. Even in the absence of VO_2 (e.g., Pt wires fabricated on SiO_2/Si or sapphire substrates), there is

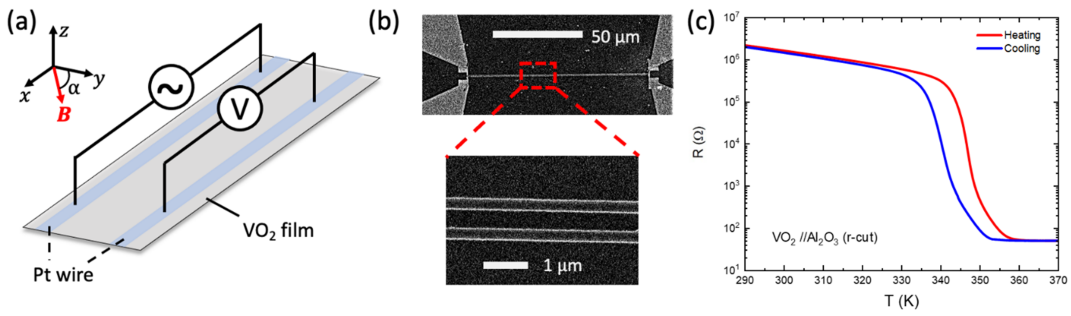

Figure 3.1 : (a) Geometry of the nonlocal spin Seebeck measurement configuration, showing the field orientations in the x-y plane with α defined as the angle between field and y-axis. (b) Scanning electron micrograph showing a typical device configuration. (c) Resistance as a function of temperature for a typical VO_2 film used in this work, showing the metal-insulator transition.

a temperature-dependent, magnetic field-independent parasitic background signal at 2ω in this electrode and wiring geometry.

3.2 Results

Below 30 K, a magnetic field-dependent 2ω signal becomes detectable, as shown in Fig. 3.2 for in-plane field oriented along $\alpha = 0°$. The signal magnitude increases with increasing field, linearly near $\boldsymbol{B} = 0$ T and saturates at high fields, with no indication of hysteresis as a function of $\boldsymbol{B}$. As the temperature decreases, the magnitude of the signal increases, with a change in sign between 15 K and 10 K. The signal grows rapidly with further decreases in temperature, and the saturation at large $\boldsymbol{B}$ is readily apparent.

To confirm that this 2ω signal results from the spin Seebeck effect, it is important to consider the field dependence of the signal on the orientation of $\boldsymbol{B}$ in the plane of the film. As shown in Fig. 3.3a, at each temperature and fixed field $\boldsymbol{B} = 3$ T, the signal is fit well by a $\cos\alpha$ dependence, as expected for the SSE and required for

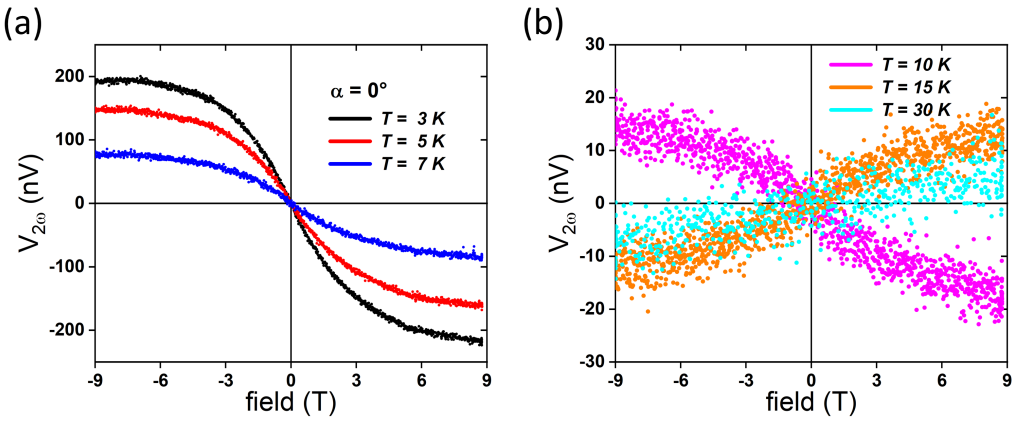

Figure 3.2 : (a) The second harmonic signal vs $\boldsymbol{B}$ at low temperatures for $\alpha = 0°$. (b) The second harmonic signal at higher temperatures, showing the sign inversion between 10 K and 15 K for the measurement configuration in Fig. 3.1b. The heater power is 40 μW.

the generation of an inverse spin Hall signal in the Pt associated with transport of angular momentum from magnetization oriented along the y-axis in the geometry of Fig. 3.1a. The 2ω voltage signal likewise depends linearly on heater power at fixed $\boldsymbol{B}$ oriented at $\alpha = 0°$, as expected for a signal of spin Seebeck origin (Fig. 3.3b). A possible confounding effect could be the Nernst response of Pt, but that is expected to be temperature independent [68] and would require a vertical temperature gradient at the VO_2/Pt detector interface and in the Pt detector. Instead, the temperature dependence of the signal is qualitatively similar to the paramagnetic response reported in the susceptibility [111, 112], supporting that the measured signal originates from the SSE. In addition to Nernst response, another possible contribution to a 2ω signal in the detector would be local SSE at the detector due to a local temperature gradient [113]. However, our temperature profile simulations (see the subsection 3.5.2) show that the vertical temperature difference between detector Pt and underlying VO_2 film is on the order of 10^{-4} mK, far too small to lead to any measurable Nernst or local

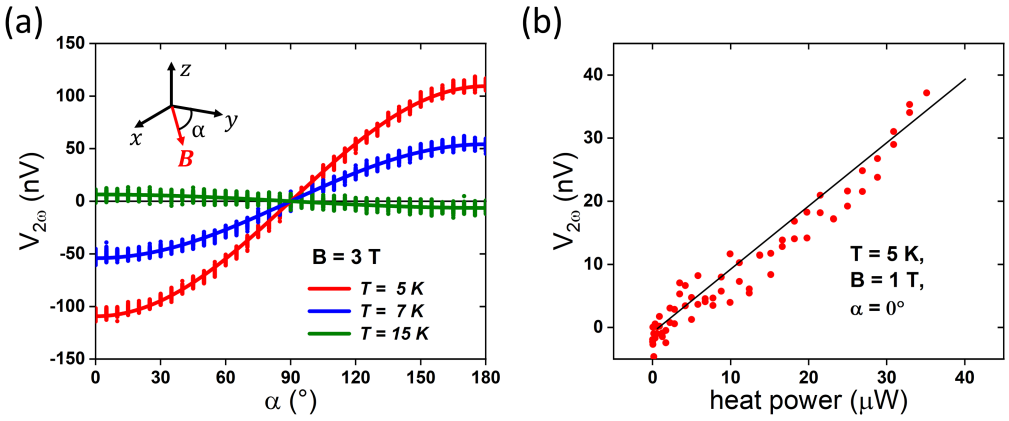

Figure 3.3 : (a) The second harmonic signal as a function of in-plane field orientation. Vertical marks show the scatters in the data at each angle, and solid lines are fit to the $\cos\alpha$ dependence. (b) The second harmonic signal is linear in heater power, as expected.

spin Seebeck effects.

Extensive additional control experiments were carried out to rule out possible artifacts. Concerns about charge leakage, unintended capacitive couplings, and other artifacts have been raised in nonlocal spin transport experiments in conducting samples [114]. We fabricated an analogous device with the identical Pt electrode geometry directly on a sapphire substrate with the same fabrication methods. The 2ω signals measured show trivial behavior at both high and low temperatures, with the in-plane external field perpendicular to the Pt wire (Fig. 3.4). This indicates that sapphire itself cannot support a spin Seebeck effect or a detectable Nernst response, as expected. This confirms that the nlSSE observed on VO_2/sapphire should originate from the VO_2 thin film.

Next, we performed a temperature-dependent study on zero-field background with different wiring configurations on a SiO_2/Si substrate. When measuring the spin Seebeck signal, there is a background response at 2ω as detected by the lock-in amplifier

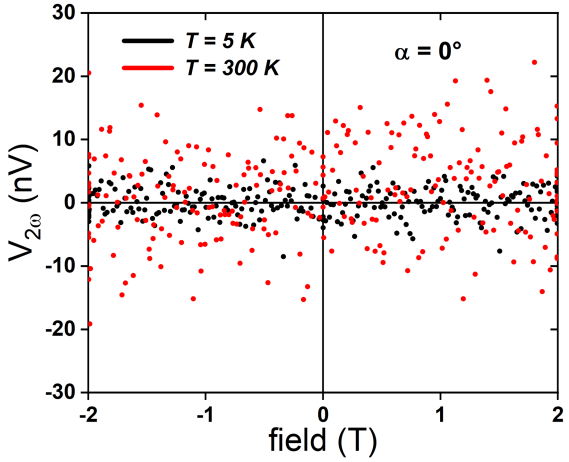

Figure 3.4 : Field dependence of the second harmonic signal at low and high temperatures for $\alpha = 0°$ on a device patterned on a sapphire substrate.

(the signal sitting at the zero field, or zero-field offset) that changes slightly with temperature. To understand this, we patterned analogous devices, with the same geometry as the Pt wires on the VO_2 film, instead on SiO_2/Si substrates using the same fabrication methods. With different wiring configurations, the zero-field offset either increases or decreases in the temperature range from 5 K to 20 K and remains essentially constant at temperatures above 20 K (Fig. 3.5a). The value of the zero-field offset changes greatly when changing the wiring and grounding configurations. This implies that this offset originates from the capacitive and inductive couplings between the wires in the measurement apparatus and the device. No field dependence of this background offset is observed in devices on SiO_2/Si, and hence it has been subtracted from the nlSSE data, under the presumption that its origin is extrinsic to the sample and its field independence will remain. The "normal" configuration refers to a configuration with heater current applied to one wire, AC voltage measured on the other wire, and the ground of the drive current is on the same end of the wires as the "B" of the (A-B) differential voltage measurement. The "swap" configuration

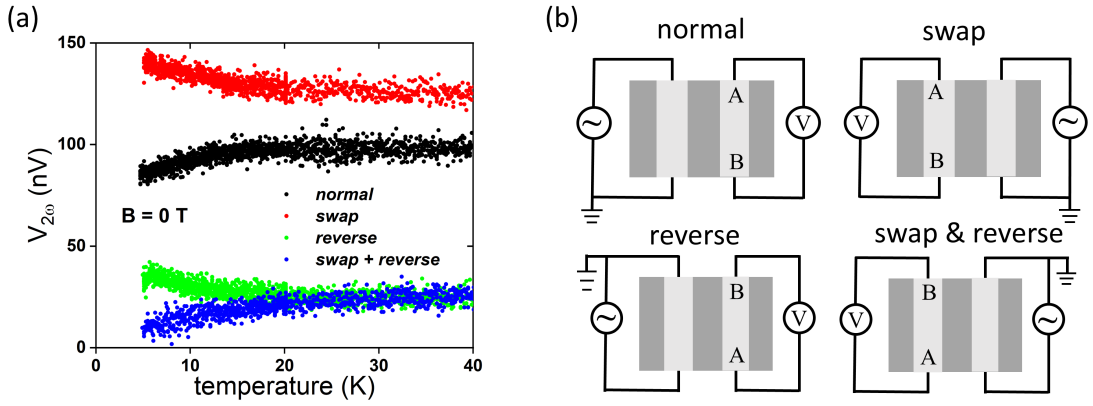

Figure 3.5 : (a) Temperature dependence of the zero-field offset with different wiring configurations on SiO_2/Si substrates. (b) Illustration of different electrode and wiring configurations.

switches which wire is used as the heater and which is used as the detector. The "reverse" configuration has the ground of the drive current on the opposite end of the wires as the B end of the differential voltage measurement.

Furthermore, an analogous device with the same electrode geometry was patterned on the VO_2 film/sapphire substrate with the same fabrication methods, one wire being Pt and the other wire Au. The resistance of Pt wire is $\sim$ 18 kΩ and the resistance of Au wire is $\sim$ 600 Ω at 10 K. When using Au wire as heater and Pt wire as detector, the 2ω signals measured on Pt wire show the similar behavior (Fig. 3.6a) as that shown in Fig. 3.2. However, when using Pt wire as heater and measuring 2ω voltage along Au wire under the same heater power condition, it shows trivial behavior (Fig. 3.6b), since Au has very small spin Hall angle [15]. This confirms that the SSE observed onVO_2/sapphire devices should originate from the Pt.

Possible charge leakage between heater and detector is expected to lead to a ω signal rather than a 2ω signal; the ω signal is dominated by capacitive effects where the quadrature component is larger than the in-phase component.

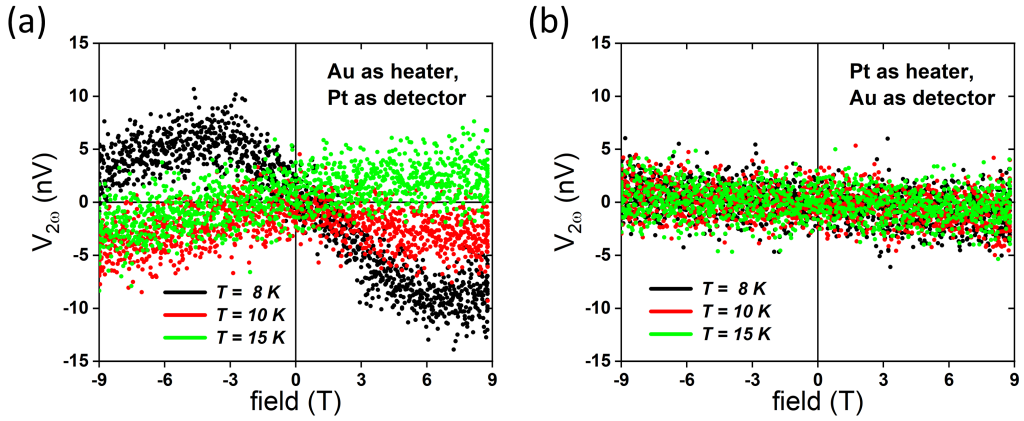

Figure 3.6 : Field dependence of the second harmonic signal at different temperatures for $\alpha = 0°$ on a device patterned on a VO_2/sapphire substrate with Pt wire (a) or Au wire (b) playing role of detector. The heater power is 40 μW in both cases.

These controls as well as the systematic dependence of the measured signal on temperature, heater power, field magnitude and orientation are consistent with nlSSE response as the signal origin.

3.3 Discussion

The growth of the SSE signal magnitude with a decrease in temperature is consistent with observations of local SSE response in paramagnetic insulator $Gd_3Ga_5O_{12}$ (GGG) [68]. In these experiments, the local SSE response as a function of $\boldsymbol{B}$ resembles the experimentally observed $\boldsymbol{M}$ vs $\boldsymbol{B}$ polarization. Deviations in the SSE vs $\boldsymbol{B}$ in GGG from a simple Brillouin function-like dependence become apparent below 4 K and are thought to be related to Zeeman effect induced suppression. Because of the small volume of VO_2 film relative to the volume of sapphire substrate and paramagnetic impurities contained within the sapphire [115], it has not been possible to isolate $\boldsymbol{M}$ vs $\boldsymbol{B}$ for the VO_2 film in our samples. The low temperature magnetization

M in bulk VO_2 crystals does not saturates at high fields [111].

The sign reversal in the measured SSE between 10 K and 15 K is qualitatively similar to a sign reversal observed in nlSSE measurements on YIG films [75]. In YIG, spin transport takes place via magnons, with regions of elevated magnon chemical potential building up in proximity to the injecting and collecting Pt wires [116]. The sign reversal of SSE in Pt/YIG/Pt is a consequence of a crossover of length scales between Pt electrode spacing and magnon chemical potential spatial length, affected strongly by the thickness of the magnon-bearing YIG film on the GGG substrate. Devices with the different wire separations were patterned on a different piece of VO_2 film/sapphire substrate other than the device reported in the Fig. 3.2 and the spin Seebeck signal was measured at $\alpha = 0°$ and low temperatures. For devices with wire separation 0.4 μm, the near-zero-field slope is negative at 5 K, 7 K and 10 K, and becomes positive at 15 K (Fig. 3.7a). However, for device with separation 1 μm, the near-zero-field slope changes sign between 5 K and 7 K (Fig. 3.7b). (We note that for this set of devices co-fabricated simultaneously, the low temperature SSE voltage vs field behaves more complicated than the saturating response at high fields shown in the Fig. 3.2 with lower magnitude of the signal, suggesting comparatively inferior Pt/VO_2 interface quality.) Thus, the sign reversal of SSE response in VO_2 moves to lower temperatures with increasing electrode spacing, though a detailed spacing dependence study has not been performed. Sign reversal of the SSE response as a function of temperature can also take place due to other mechanisms. In antiferromagnets and compensated ferrimagnets, competing responses of two magnon branches can cause a crossover in LSSE sign as a function of temperature [43]. Similarly, in an antiferromagnet, the presence of multiple magnon branches can lead to a field-dependent precession of the magnon pseudospin [117]. Both of these possibil-

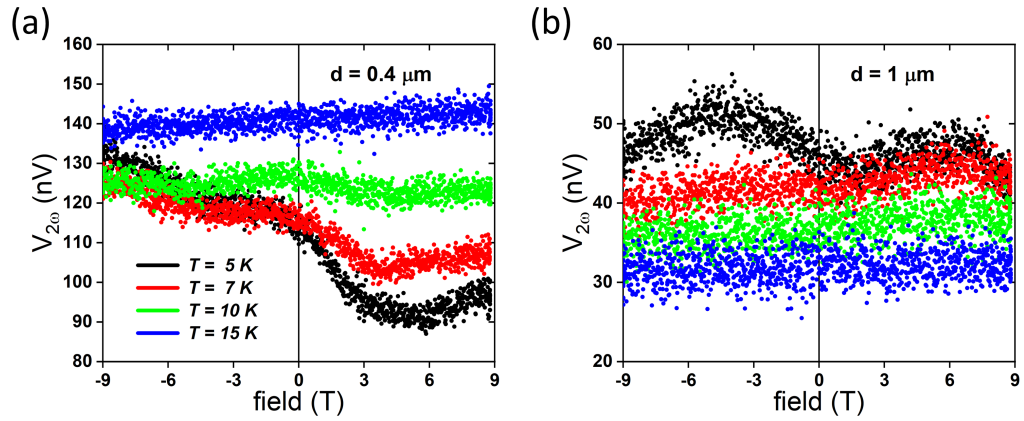

Figure 3.7 : Field dependence of the second harmonic signal at different temperatures with separation between the wires being 0.4 μm (a) and 1 μm (b).

ities would require the presence of long-range magnetic order and multiple magnon branches in the material, which are believed absent in VO_2.

Repeated measurements of devices, after cycling back to room temperature and sample aging on the timescale of days or weeks, show much reduced signal magnitudes, though identical field dependence. The nlSSE signal depends critically on interfacial exchange coupling between the oxide ions and the Pt conduction-electrons and, hence, is extremely sensitive to the Pt/oxide interface quality. The observed signal reduction upon sample aging likely indicates degradation of the Pt/VO_2 interface.

The presence of a strong spin Seebeck response that grows at low temperatures in VO_2 calls into question the nature of the angular momentum-carrying excitations. In prior examinations of paramagnets, the argument was advanced that SSE response can originate from short-range magnetic order [69] or field-supported paramagnons above a lower ordering temperature [68]. The magnetic state of monoclinic VO_2 is thought to be a singlet-dimer state [109], rather than a traditionally ordered state. One picture for the phase is that the dominant spin-carrying excitations are thermally

excited triplets ("triplons") and the increase in susceptibility at low temperatures is due to the Curie-like response of the temperature-dependent effective spin of the dimers [111, 112]. This picture does not have long-ranged order nor well-defined magnons. The sign inversion of the SSE as a function of temperature suggests that it may be related to the spatial distribution of the local chemical potential of spin-carrying excitations.

We note that muon spin rotation within monoclinic VO_2 implies the onset of an internal magnetic field below a sharp transition near 35 K [118]. This is interpreted as originating from the "disruption of the V-V dimers", which produce a "nonzero net spin" below 35 K. This suggests that there may indeed be some magnetic ordering taking place that is not readily observed in the susceptibility yet may lead to well-defined magnon excitations. While high temperature defect-mediated ferromagnetism is possible in VO_2 films deposited on sapphire [119], there is no evidence of any ferromagnetic order in the present or other materials grown by the authors, nor is the observed field dependence of the signal compatible with ferromagnetism.

3.4 Conclusion

To summarize, we have detected a spin Seebeck response in insulating VO_2 thin films below 30 K that grows in magnitude with increasing field. This response is non-hysteretic in $\boldsymbol{B}$, has the expected SSE dependence on field orientation in-plane, and saturates at large $\boldsymbol{B}$ and low temperatures. Given the singlet-dimer nature expected of the monoclinic VO_2 ground state, a detailed examination of angular momentum transport in this system is needed to explain these observations, and whether such an effect is a consequence of the transport of triplet excitations or a sign of the emergence of magnon-like excitations in a magnetically ordered phase below 35 K.

3.5 Supplementary information

3.5.1 Resistance and capacitance between two nearby Pt wires

We used two-terminal lock-in measurement methods (Fig. 3.8a) to measure the resistance and capacitance between the two nearby Pt wires, with the separation being 0.4 μm, of the device on VO_2/sapphire. An ac voltage with frequency $f = 2.01$ Hz was applied to the two Pt wires, and the voltage U between the wires and the current I flowing through the VO_2 film were measured simultaneously. The current has both x-component and y-component because of the capacitance between the wires, denoted as I_x and I_y. Then the resistance of the film is given by: $R = U/I_x$, and the capacitance is given by $C = I_y/(2fU)$.

Although VO_2 is deep in the insulating regime, the resistance between two nearby Pt wires is not unmeasurably high in this configuration. This residual conduction has no obvious temperature dependence from 5 K to 30 K (Fig. 3.8b). Besides, the capacitance between the wires is also independent on temperature (Fig. 3.8c).

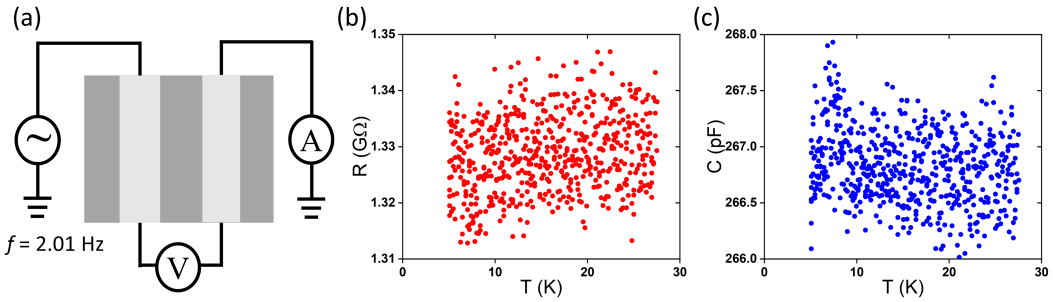

Figure 3.8 : (a) Illustration of two-terminal lock-in measurement setup. (b, c) Temperature dependence of resistance and capacitance between two nearby Pt wires, respectively.

3.5.2 Temperature profile simulation of nonlocal spin Seebeck device

We simulated the temperature profiles with COMSOL of the nonlocal spin Seebeck device induced by Joule heating on VO_2/sapphire substrates with specific geometry and reasonable material parameters (see Table 3.1). The chamber temperature of PPMS $T_0 = 5$ K was set as a boundary condition at the bottom of sapphire. We also applied the thermal boundary conductance at the Pt/VO_2 interface (~ 60 $MWm^{-2}T^{-1}$). As shown in Fig. 3.9, the current flowing through the heater wire with power 32 μW warms up the heater and underlying Pt wire nearby; however, this temperature gradient is strongly localized near the heater wire and the heater power has minor effect on the detector wire (Fig. 3.10). More specifically, the temperature difference between the detector and the underlying VO_2 film is on the order of 10^{-4} mK (Fig. 3.12).

	Pt	**VO_2**	**sapphire**
geometry	length 100 μm; width 200 nm; thickness 20 nm; edge-to-edge distance 400 nm.	infinite plane; thickness 100 nm.	infinite large.
electric conductivity	1.25×10^6 S/m	$\sim 10^5$ S/m	$\sim 10^{-10}$ S/m
thermal conductivity	$\sim$ 0.15 W/(mK)	$\sim$ 20 W/(mK)	$\sim$ 550 W/(mK)
density	21.45×10^3 kg/m^3	4.57×10^3 kg/m^3	3.98×10^3 kg/m^3
specific heat	$\sim$ 0.266 J/(kgK)	$\sim$ 0.0313 J/(kgK)	$\sim$ 0.098 J/(kgK)

Table 3.1 : Geometry and material parameters of Pt, VO_2, and sapphire used in the simulation.

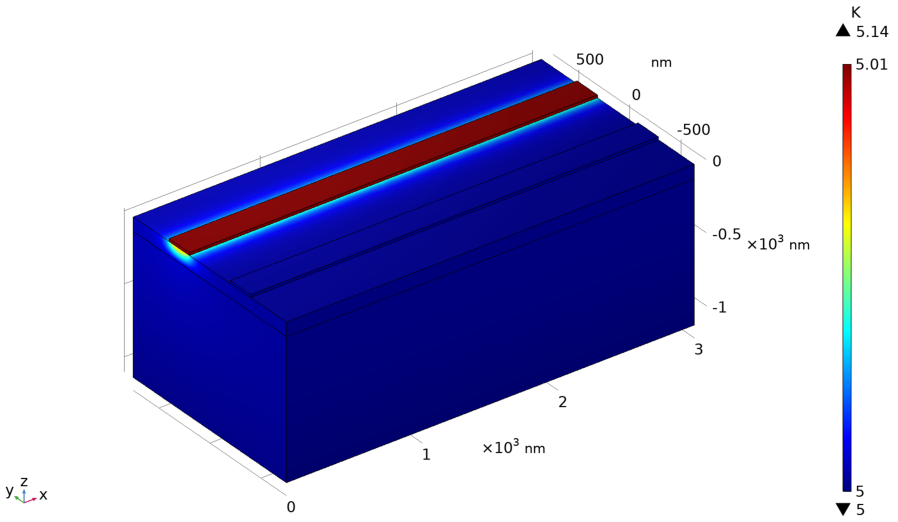

Figure 3.9 : Temperature profile of the nlSSE device on the VO_2/sapphire substrate.

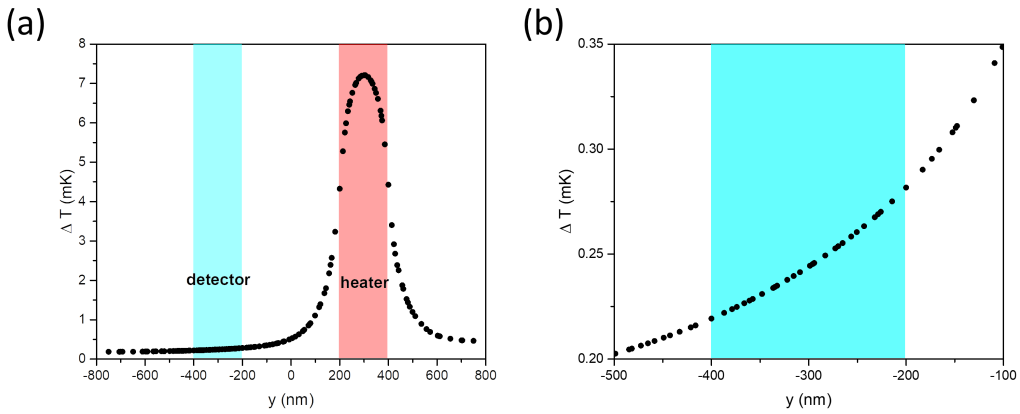

Figure 3.10 : (a) Temperature difference profile on the y-direction on the top surface of VO_2, including the interface between VO_2 film and the heater wire and the interface between VO_2 film and the detector wire. (b) Temperature difference profile on the y-direction on the top surface of VO_2 near the interface between VO_2 film and the detector wire.

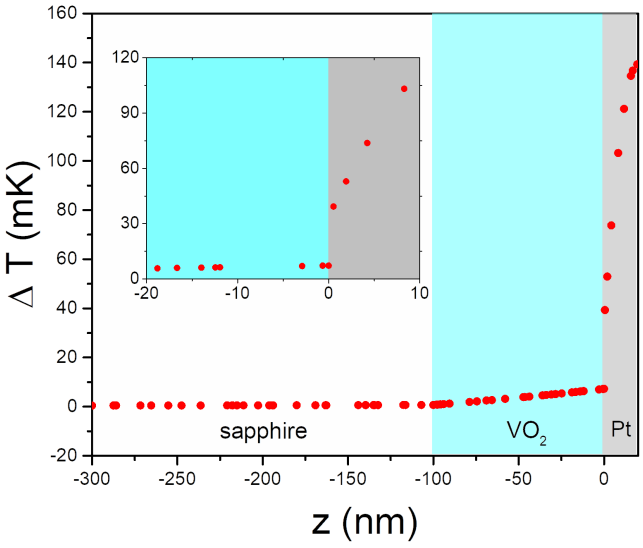

Figure 3.11 : Temperature difference profile on the z-direction at the center of the heater wire and underlying VO_2/sapphire. Inset is the enlargement of the figure near the Pt/VO_2 interface. The area in white, cyan and gray color indicate sapphire substrate, VO_2 and platinum, respectively.

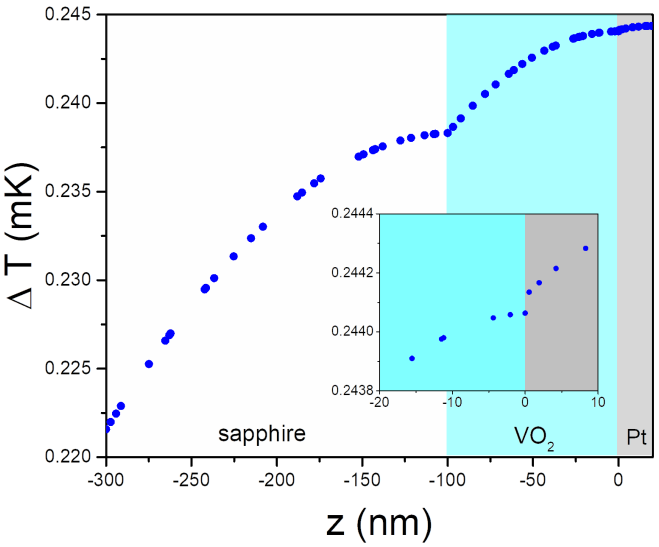

Figure 3.12 : Temperature difference profile on the z-direction at the center of the detector wire and underlying VO_2/sapphire. Inset is the enlargement of the figure near the Pt/VO_2 interface.

Chapter 4

Low Temperature Longitudinal Spin Seebeck Effect in Non-Magnetic Vanadium Dioxide

Following Chapter 3, this chapter will mainly show a readily detectable longitudinal spin Seebeck response in the nonmagnetic insulating phase of vanadium dioxide (VO_2) films at low temperatures. The longitudinal spin Seebeck effect (LSSE) voltage grows linearly with increasing field at low fields but experiences a field-induced reduction at high fields and the lowest temperatures, qualitatively consistent with the recent model of paramagnetic SSE response. The LSSE shows the expected angular dependence with the in-plane field orientation and is linear to the heater power. When the heater power is held constant, the magnitude of LSSE voltage peaks with increasing temperature. The sign of the LSSE response is not consistent with that expected for a triplon-mediated SSE, in which mobile triplet excitations are the angular momentum carriers. The magnitude of SSE in VO_2 is comparable to that in $Y_3Fe_5O_{12}$, a paradigmatic ferrimagnetic insulator that exhibits magnon-mediated SSE. The magnetic degrees of freedom in the VO_2 and the mechanism behind such an unexpectedly large paramagnetic SSE call for further studies. This chapter is adapted with permission from *Physical Review B*. See Ref [120].

4.1 Properties of vanadium dioxide

Strong electronic correlations can lead to the emergence of local moments and unusual spin excitations. Vanadium dioxide (VO_2) is a paradigmatic example of a

correlated transition metal oxide, with a metal-insulator phase transition at $\sim$ 345 K in bulk, between a high-temperature rutile metallic phase and a low-temperature monoclinic insulating phase [109, 110, 121]. Thermodynamic arguments [122], quantum Monte Carlo calculations [123] and low-frequency Raman spectra [124] indicate that, in the monoclinic phase, the vanadium ions form dimers, each of which comprises a spin singlet in the ground state (as shown in Fig. 4.1). As a result, the insulating VO_2 is expected to be nonmagnetic in the sense of lacking local moments. In practice, VO_2 is paramagnetic throughout the range of temperatures covering the metallic and insulating states [111]. The deviation from Curie law susceptibility at low temperatures (see Fig. 4.2) has been suggested to result from paramagnetic contributions from unpaired electrons created by thermal excitation of triplet states [112].

Ideally, we need to measure the magnetization of VO_2 thin film in our device. However, due to the small thickness compared to the diamagnetic substrate sapphire (hundreds of nanometers compared to millimeter), the magnetic signal of VO_2 is overwhelmed by the diamagnetic background of the sapphire. For an example of VO_2 magnetic response at low temperatures, we measured a sample of commercially available VO_2 powder. In Fig. 4.2a, we show the field dependence of magnetization. No hysteresis is observed, implying that VO_2 is paramagnetic. The susceptibility increases when the temperature is lowered. The $1/\chi$ vs. T plot (Fig. 4.2b) shows the deviation from a straight line, indicating other paramagnetic contributions, rather than Curie's law, dominate at low temperatures. Extrapolating the high temperature trend implies a negative Curie-Weiss temperature, $\sim$ -5.60 K.

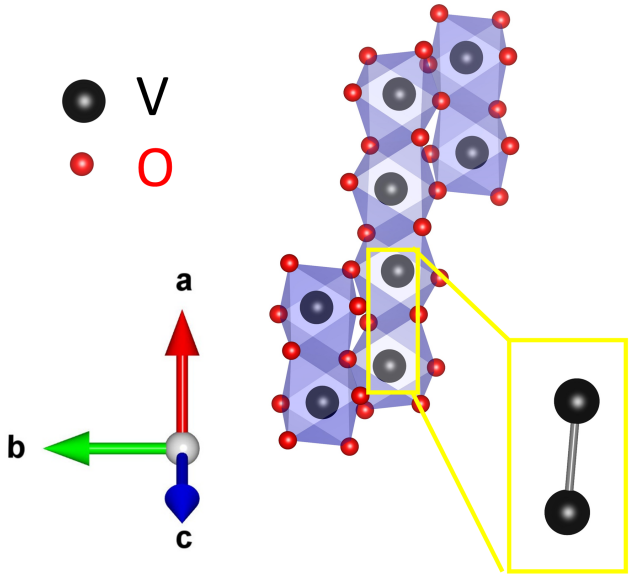

Figure 4.1 : Crystal structure of VO_2 in the low temperature, insulating monoclinic phase. The inset shows parallel zigzag chains each consisting of V-V dimers in this phase. Films in this work have the V chains oriented along the normal direction of the surface, parallel to the applied temperature gradient. The crystal structure is generated by VESTA [125].

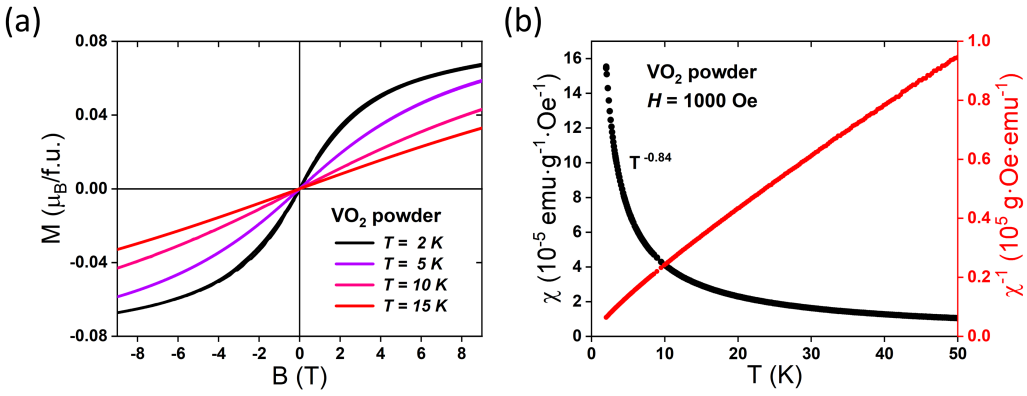

Figure 4.2 : (a) Field dependence of the magnetization of VO_2 powder, showing paramagnetism over the temperature range of interest. (b) Temperature dependence of magnetic susceptibility χ and $1/\chi$ in the field of 1000 Oe. The susceptibility shows non-Curie behavior at low temperatures.

4.2 Device fabrication and experimental setup

In the on-chip-heating geometry of the longitudinal SSE (LSSE) [23], a current flowing through a heater wire is driven at angular frequency ω, creating a temperature gradient normal to the sample surface with an AC component at 2ω. This drives an angular momentum current, and a voltage at 2ω can be detected at a nearby inverse spin Hall (ISH) detector made from a strong spin-orbit metal (e.g., Pt) for a properly oriented magnetization of the insulator. Single-phase epitaxially grown VO_2 thin films with different thicknesses (50 nm, 100 nm, 250 nm, 400 nm) were deposited on 7×12 mm^2 $[1\bar{1}02]$ r-plane Al_2O_3 substrates using RF magnetron sputtering from a V_2O_3 target (99.9% purity) at a substrate temperature of 520 °C in Ar/O_2 mixture (8% O_2) at 3.7 mTorr [126]. The substrate was later cooled down to 20 °C at a rate of 12 °C/min. X-ray diffraction measurements confirmed single-phase, textured growth along (100) for VO_2. A schematic of the device is presented in Fig. 4.3a and a photography of a Pt/VO_2 (100 nm) device is shown in Fig. 4.3b. Photolithography, magnetron sputtering, and liftoff were used to prepare the Pt (W) wire (800 μm long, 10 μm wide, 10 nm thick) on the VO_2 film surface. A lithographically defined SiO_x layer with a thickness of 100 nm and a Au heater wire (1300 μm long, 10 μm wide, 50 nm thick) were fabricated on the top of the Pt (W) wire by e-beam deposition and liftoff. The SiO_x layer electrically isolates the Au heater and the Pt (W) wire. An AC current at angular frequency $\omega = 2\pi \times$ (7.7 Hz) is driven through the Au wire, while the voltage across the Pt (W) wire is measured at 2ω using a lock-in amplifier. The measurements are performed as a function of temperature and field in a Quantum Design Physical Property Measurement System (9T-PPMS) and 14T-DynaCool equipped with a rotation stage.

Since the spin Seebeck response is proportional to the resistivity of the spin-orbit

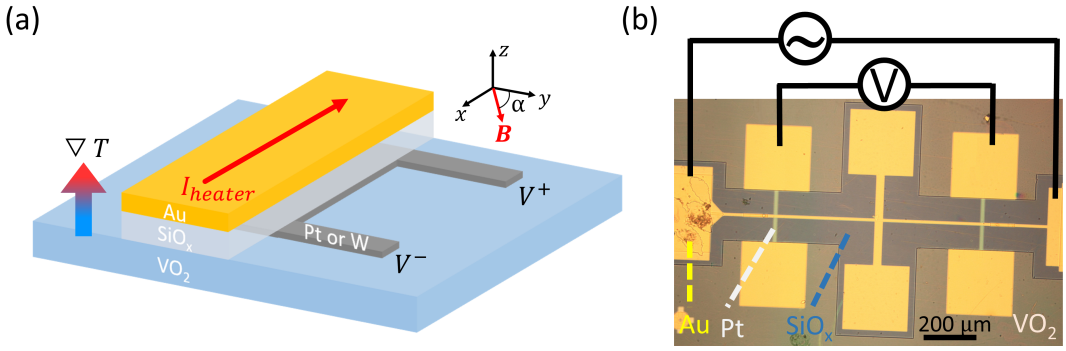

Figure 4.3 : (a) Schematic of local spin Seebeck measurement. An AC heater current produces an oscillating z-directed temperature gradient. A vertical (z-directed) thermal spin current with the y component of the paramagnetic magnetization of the VO_2 could produce an ISH voltage along the x-directed strong spin-orbit metal wire. (b) Optical microscope image of a representative device.

metal, a change of the Pt and W resistance with temperature or field will affect the measured spin Seebeck voltage extrinsic to the actual spin Seebeck physics. Fig. 4.4a (4.4b) shows the temperature dependence of the resistance of the Pt (W) wire. The change of R_{Pt} and R_W in the temperature range from 50 to 5 K is relatively small, less than 2%. The field dependence of R_{Pt} and R_W at T = 5 K at some selected angles is shown in Fig. 4.4c and Fig. 4.4d, respectively. R_{Pt} and R_W change less than 0.1 % up to 8 T. In short, the contribution of the resistivity change in the Pt and W wires within the experiment's temperature and magnetic field ranges is negligibly small compared to the observed SSE signal in our devices.

4.3 Results and discussion

4.3.1 Field dependence

The magnetic field dependence of the second harmonic signals is shown for Pt/VO_2 (100 nm thick) (Fig. 4.5a,b) and W/VO_2 (100 nm thick) (Fig. 4.5c) for the in-plane

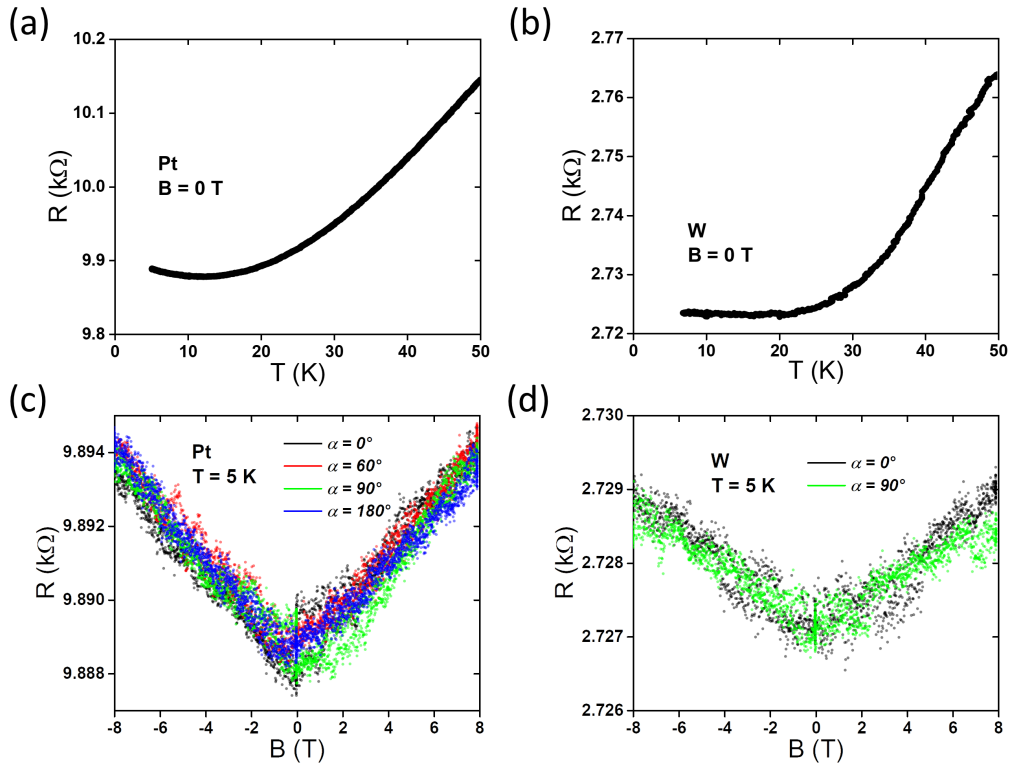

Figure 4.4 : Resistances of the Pt wire and W wire. (a, b) Temperature dependence of the resistances of the Pt and W wires. (c, d) The magnetoresistances of the Pt and W wires at 5 K, at some representative angles. The resistance changes for both metals with fields up to 8 T are below 0.1 % and is qualitatively consistent with weak antilocalization. [127, 128]

field oriented at $\alpha = 0°$ for different selected temperatures, with direction and polarity defined as in Fig. 4.3a. At $T = 50$ K, we observed almost no voltage signal (Fig. 4.5a). With decreasing T, a clear $V_{2\omega}$ signal appears, with a sign that changes with respect to the $\boldsymbol{B}$ direction, reflecting the symmetry of the ISHE. When the temperature is above 5 K, the signal magnitude increases monotonically with increasing field, linearly near $\boldsymbol{B} = 0$ T, resembling the $M(H)$ curve (Fig. 4.2a); whereas below 5 K, the signal takes the maximum value at a certain field (for example, 5.2 T at 2.5 K) (Fig. 4.5b). The voltage responses for devices with Pt and W detectors are of opposite signs (shown in

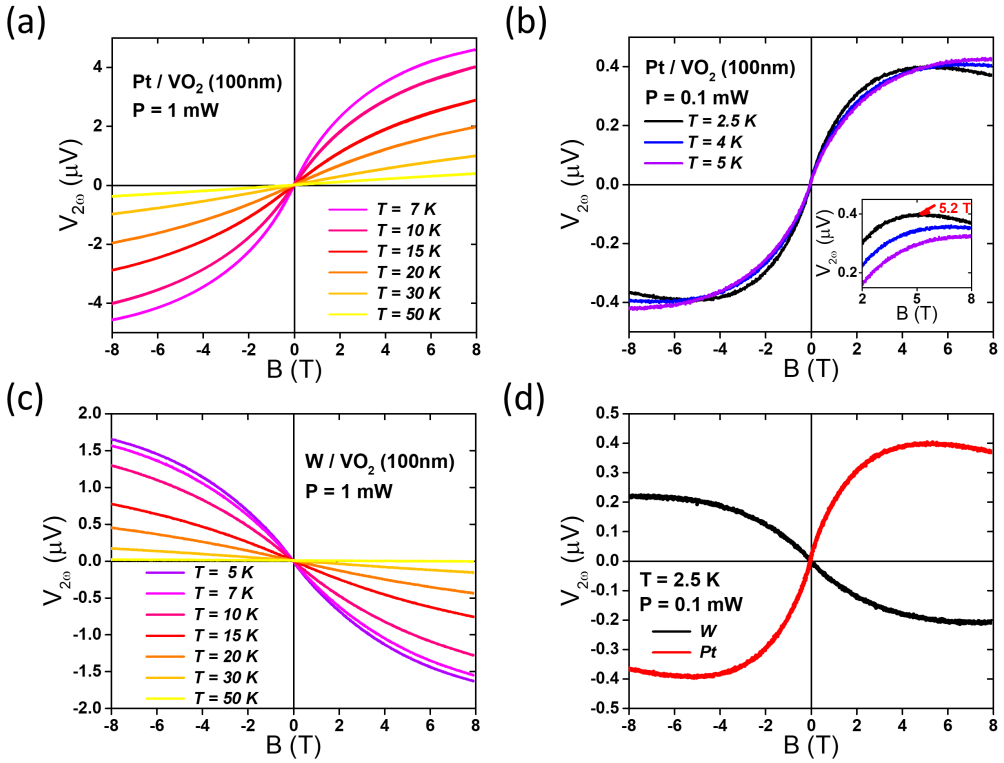

Figure 4.5 : (a-c) The second harmonic voltage as a function of field ($\alpha = 0°$, $\boldsymbol{B}\|$y) at various temperatures for Pt (a,b) and W (c) detector wires on 100 nm thick VO_2. For Pt wire, data above 5 K are taken at 1 mW heater power; data at 5 K and below are taken at 0.1 mW heater power to minimize differences between local temperature and cryostat temperature. For W wire, all the data are taken at 1 mW. (d) Comparison between voltage responses of Pt/VO_2 and W/VO_2 devices at 2.5 K with an applied heater power of 0.1 mW.

Fig. 4.5a,c,d), as expected for a genuine spin current effect, since the spin Hall angles of Pt and W are opposite in sign [15]. The shapes of voltage curves for Pt/VO_2 and W/VO_2, accounting for the sign change, are very similar, indicating they are of the same origin.

At temperatures below 5 K, by further increasing B above some certain field, $V_{2\omega}$ starts to decrease, showing a B-induced reduction of the paramagnetic SSE in the Pt-based device, which is not due to the magnetoresistance of Pt wire (Fig. 4.4c).

A similar B-induced reduction was also observed in measurements on $Gd_3Ga_5O_{12}$ (GGG) [68, 69]. This was interpreted as the suppression of the interfacial spin-flip scattering between the Pt conduction electrons and the spin in the insulator [102], since at high fields and low temperatures, the Zeeman energy ($g\mu_B B$) of the spin becomes comparable to the thermal energy ($k_B T$).

The 2ω signal has the orientation dependence of $\boldsymbol{B}$ in the film plane as expected for the spin Seebeck effect. As shown in Fig. 4.6a, at fixed field magnitudes $|\boldsymbol{B}|$ = 1 T and 6 T, the signal is described well by a $\cos\alpha$ dependence (the dashed curve), as expected for the SSE. The 2ω voltage signal likewise depends linearly on the heater power at fixed $\boldsymbol{B}$ oriented at $\alpha = 0°$ (Fig. 4.6b), as expected for a SSE signal. A potential confounding effect in this experimental geometry, the ordinary Nernst response of Pt (W), expected to be linear with the applied magnetic field, cannot explain the observed magnetic field dependence of $V_{2\omega}$ shown in Fig. 4.5a-c. Furthermore, with a 10-nm-thick insulating SiO_x layer inserted between the Pt and the VO_2 film, the signal is reduced of 2 orders of magnitude (see the subsection 4.5.3), consistent with the ordinary Nernst response measured in similar geometry [129].

4.3.2 Comparison with magnon LSSE in yttrium iron garnet

We compare the magnitude of SSE in VO_2 with that in the ferrimagnetic insulator $Y_3Fe_5O_{12}$ (YIG). The spin Seebeck coefficient [27, 28] is found as $\sigma_{SSE} = (V_{SSE}/l)/(\mathrm{d}T/\mathrm{d}z)$, where l is the length of the ISH detector, and $\mathrm{d}T/\mathrm{d}z$ is the temperature gradient in the insulator. At low temperatures in bulk YIG, the measured σ_{SSE} is around 5 μV/K [28]. For VO_2, a rough estimate of the thermal conductivity gives 10 nV/K at 8 T and 10 K, close to that estimated in YIG of 70 nV/K for 250 nm thickness and the same temperature range. Given the uncertainties as-

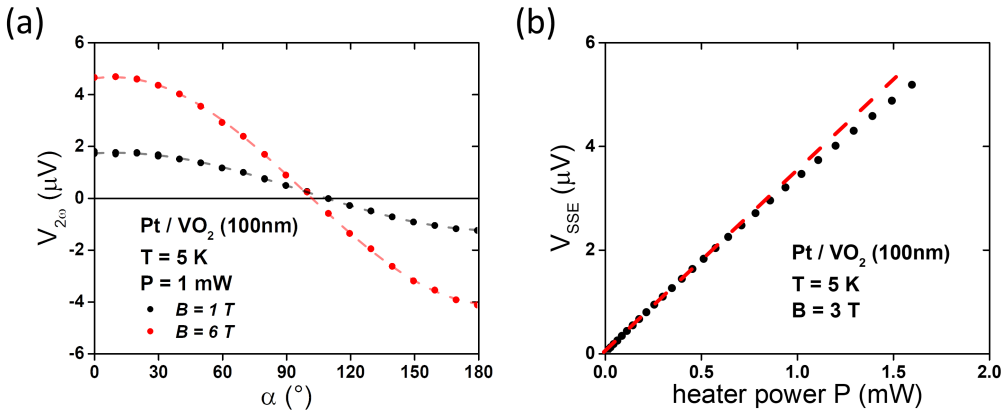

Figure 4.6 : (a) Dependence of the second harmonic signal in Pt wire at 5 K with 1 mW heater power on in-plane field orientation α, showing expected cosine dependence. The device is misaligned in the plane by a few degrees relative to the ideal positioning. (b) Dependence of the spin Seebeck voltage on the heater power at 5 K and 0°. The SSE voltage is defined as the difference of the second harmonic signals between zero-field and 3 T. The slight sublinear dependence at high heater powers indicates a discrepancy between the local sample temperature and cryostat temperature.

sociated with interfacial thermal resistances, an alternative approach to comparing SSE responses between materials uses the spin Seebeck resistivity [29], defined as $R_{SSE} = (V_{SSE}/l)/j_Q$, where j_Q is the heat flux through the insulator. In YIG, R_{SSE} is $\sim$ 10 nm/A for 100 nm thick films at 10 K [29]; and in 100 nm-thick VO_2, R_{SSE} is $\sim$ 65 nm/A at 10 K and 8 T. That VO_2 has a SSE response comparable to that in the ferrimagnet YIG is striking, given that monoclinic VO_2 is not expected to host magnetic excitations.

4.3.3 Comparison with triplon LSSE in copper germanate

The presence of a strong low temperature spin Seebeck response in VO_2 raises the question regarding the nature of the angular momentum-carrying excitations. The fact that the ground state of monoclinic (M1) VO_2 is a singlet-dimer state leads to

considering whether thermally excited triplets ("triplons") may transport spin angular momentum, leading to a triplon SSE. A triplon SSE has previously been reported in the LSSE measurement configuration in the spin-Peierls system $CuGeO_3$ [72], where Cu atoms form one-dimensional spin-1/2 chains with antiferromagnetic exchange interactions. A key distinguishing feature of the triplon SSE is its voltage sign, consistent with the triplon current carrying magnetization in the same orientation as the bulk magnetization. In coerced ferromagnets (or paramagnons in paramagnets), conversely, a magnon transports magnetic moment that is antiparallel to the bulk magnetization. In the $CuGeO_3$ system, consistent with triplons as the spin-carrying excitations, the LSSE voltage was found to be of the opposite sign as the LSSE voltage in YIG, in which magnons provide the SSE response. To test the LSSE voltage sign in our system, we made an analogous device on a YIG thin film of 40 nm thickness deposited on a $Ga_3Gd_5O_{12}$ (GGG) substrate. The sign of the LSSE signal in the VO_2 device is the same as that of the magnon-mediated SSE in the YIG/GGG device (Fig. 4.7), in contrast to the $CuGeO_3$ case, seemingly ruling out the possibility that the SSE in VO_2 is caused by a current of triplons.

Assuming the ideal singlet dimer picture of the monoclinic VO_2 state, there should be no free magnetic moments. In the $CuGeO_3$ case, the free spin density (due to local disorder preventing singlet dimer formation) is estimated to be 0.02%, and the average distance between free spins is estimated to be around 1.5 μm, too dilute for correlations between the free spins to contribute to spin current transport [72]. In the VO_2 case, one analysis based on the low–temperature susceptibility roughly estimates that $\sim 15\%$ V^{4+} ions could be "free" ions residing in the otherwise dimerized system [112], though sample preparation would likely affect this greatly. For example, internal stresses in the film could potentially stabilize regions of two other insulating

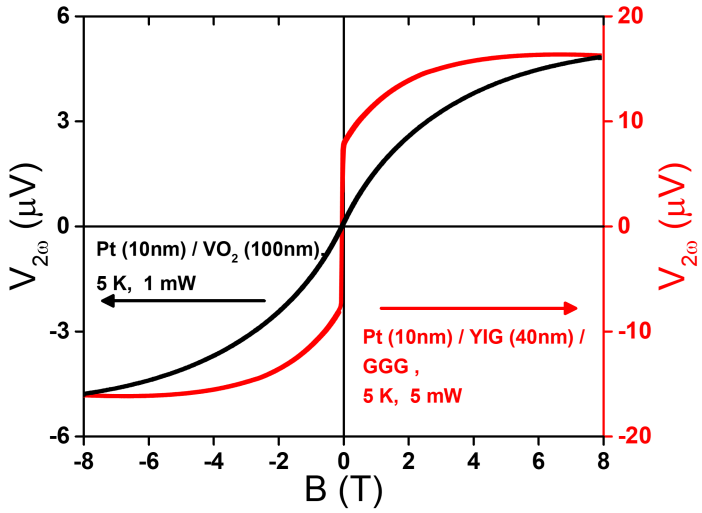

Figure 4.7 : The second harmonic voltage as a function of field for the Pt/VO_2/sapphire device and the Pt/YIG/GGG device.

metastable phases of monoclinic, M2 (space group C2/m) and triclinic, T (space group P1) by introducing tensile strain along the V-V zigzag chain [130], both of which could create some undimerized V ions. Deviations from ideal oxygen stoichiometry could likewise lead to unpaired spins. Further experiments involving radiation damage or other means of breaking V-V dimers could test this idea.

4.3.4 Comparison with paramagnetic SSE model

We consider whether the LSSE data from VO_2 can be understood within a particular model of the paramagnetic SSE due to the spin-flip scattering via the interfacial exchange coupling between localized moments in the VO_2 and conduction-electron spins in the Pt [102]. Within this model, the ISHE-induced voltage, V_{SSE}, can be expressed as:

$$V_{SSE}/V_{SSE}^{max} = C\frac{SB_S(\xi)\xi^2}{\sinh{(\xi/2)}^2}, \tag{4.1}$$

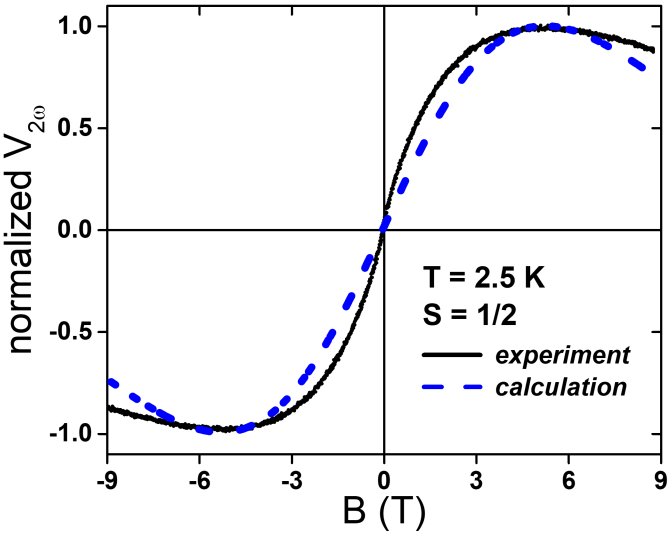

Figure 4.8 : Comparison of normalized spin Seebeck voltage between the experiment data in Fig. 4.12b and the theoretical model calculation described in the text. The experiment data is taken at 2.5 K with 0.1 mW heater power. We obtained the optimal Θ_{CW} = -1.93 K by fitting at this temperature, consistent with a tendency toward antiferromagnetism. The data are normalized so that the maxima are set to 1.

where C is a normalization prefactor, $B_S(\xi)$ is the Brillouin function of spin S, and $\xi = g\mu_B B/k_B T$ is the dimensionless ratio of the Zeeman energy to the thermal energy, in which g is Landé g-factor, μ_B is Bohr magneton and k_B is Boltzmann constant. B is within the Curie-Weiss molecular field model $B_{eff} = [T/(T - \Theta_{CW})]B$, where Θ_{CW} is a possible Curie-Weiss temperature of VO_2. In the formula, the only free parameter is Θ_{CW} and to get the optimal value of Θ_{CW}, we use the least squares fitting. We build the loss function as follows:

$$R^2 = \Sigma_i \left[v_{obs}(B_i) - v_{cal}(B_i)\right]^2, \tag{4.2}$$

where $v_{obs}(B_i)$ is the observed normalized SSE response at field B_i, v_{cal} is given by Eqn. 4.1, and then find the value of Θ_{CW} to minimize R^2. The best fitting with S = 1/2 is shown in Fig. 4.8. Comparing with the measured spin Seebeck signal, the

calculation shows the observed field-induced reduction above a similar field. However, the zero-field slope in the calculation is smaller than the observed signal; in addition, the high-field reduction predicted by the calculation is larger than the reduction observed in the measured data. Attempting to fit the data at higher temperatures requires a temperature-dependent Θ_{CW}, implying that other temperature-dependent physics is relevant. Even allowing Θ_{CW} to vary with temperature or considering spin-1 as well as spin-1/2 moments, it is not possible to simultaneously fit accurately the low-field slope and the high-field reduction in SSE vs. B dependence. The quantitative disagreement between the experiment and the calculation suggests that the measured signal is not caused by a pure interfacial effect. In fact, the sign reversal of nonlocal SSE on VO_2 on 100-nm-thick films (Chapter 3) implies that there is a bulk contribution to the SSE due to the local chemical potential of the spin-carrying excitations [131].

4.3.5 Temperature dependence

To constrain the mechanism driving the spin Seebeck response in VO_2, we examined its temperature dependence. Fig. 4.9a shows the temperature dependence of LSSE voltage response in a Pt wire on 100 nm thick VO_2 with different fields, from 2 K to 50 K. At constant heater power, the LSSE voltage at each field increases with decreasing temperature, reaching a maximum at a peak temperature T_{peak}, and decreases with further decreasing temperature. The peak temperature increases with increasing fields (Fig. 4.9b), qualitatively consistent with the linear field dependence of $T_{peak} \approx g\mu_B B/k_B - |\Theta_{CW}|$ from the model [102]. However, the model does not fully account for the temperature dependence originating from the Kapitza thermal boundary conductance.

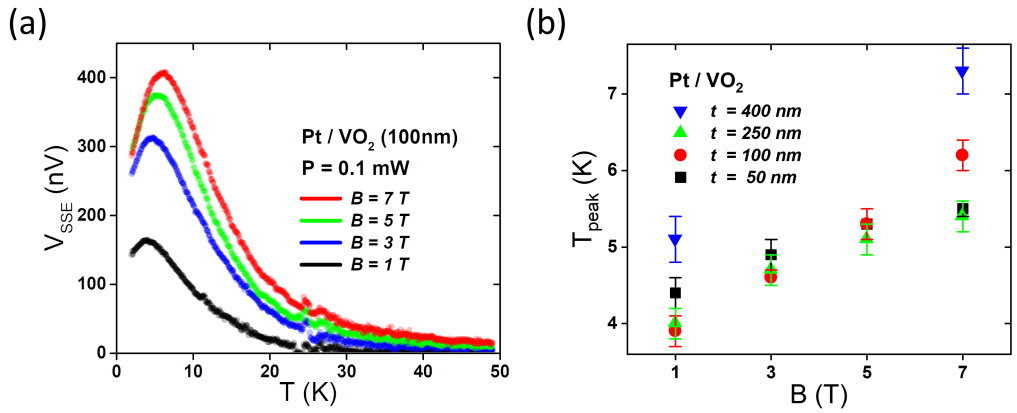

Figure 4.9 : (a) Temperature dependence of the LSSE voltage, defined as the difference between the second harmonic voltages at a certain field and 0 T, in the Pt wire on the 100-nm-thick VO_2 film at constant heater power of 0.1 mW and $\alpha = 0°$. (b) Field dependence of the peak temperature for different thicknesses of VO_2. For each thickness, the peak temperature increases with the field approximately linearly.

Between 15 and 50 K, the LSSE voltage in VO_2 varies approximately as T^{-2}. In contrast, previous work on the paramagnetic SSE in GGG showed a steeper power-law decay of the LSSE voltage at constant heater power, proportional to $V_{2\omega} \propto T^{-3.384}$ [68]. The argument was to be roughly consistent with a Curie-like temperature dependent magnetization $M \propto 1/T$ combined with the temperature-dependent thermal conduction of the crystalline insulator and the Kapitza thermal boundary conductance between the metal and the insulator ($\kappa \sim T^3$ for both). The considerably weaker temperature dependence observed here in VO_2 is thus surprising. Although the magnetization of VO_2 at low temperatures was reported to be unusual [110, 112], we have been unable to measure directly $M(T, H)$ or the low temperature thermal conductivity of these thin films. This discrepancy in temperature dependence suggests a potentially strong temperature dependence of the interfacial spin exchange coupling at the VO_2/metal interface.

The spin-gapped system $Pb_2V_3O_7$ showed a similar peak behavior [73], attributed

to the competition between the decreased paramagnon density and the increased paramagnon lifetime as the temperature decreases, the same explanation as argued in the ferromagnetic SSE [95]. In recent work in ferromagnets, however, both experiment [28] and theory [96], showed that, at low temperatures, the SSE can be dominated by a phonon-drag mechanism, where the spin current is induced by temperature-gradient-driven phonons via magnon-phonon interactions. In this case, the phonon-drag model predicts $V_{SSE} \propto \kappa \nabla T = j_Q$ [96], which is constant in our measurement method, contrary to the observed temperature dependence.

4.3.6 On different thicknesses

As mentioned above, both bulk contribution [95, 96] and the interfacial contribution [102] to the spin Seebeck response exist. We fabricated devices with the same geometry and fabrication protocol but varying thicknesses of VO_2 films [39]. The magnitude of the SSE response is expected to be directly proportional to the interfacial spin exchange coupling at the spin-orbit metal/insulator interface, and thus extremely interface sensitive. Fig. 4.10 shows the field and temperature dependence of the second harmonic signal for different thicknesses of VO_2 film. The responses are qualitatively all very similar. The field dependence of LSSE voltage at 2 K and 5 K shows no systematic trend of the magnitude with film thickness (Fig. 4.11a,c), while interfacial temperature difference should be governed by differences in the sound speed between the metal and the insulator and are not expected to vary by large amounts. This implies that the interfacial spin exchange and thus the effective spin conductance can vary from device to device, even with nominally identical processing steps. When normalizing to its maximum value (Fig. 4.11b,d), the normalized LSSE voltage as a function of field shows consistent behavior across all thicknesses,

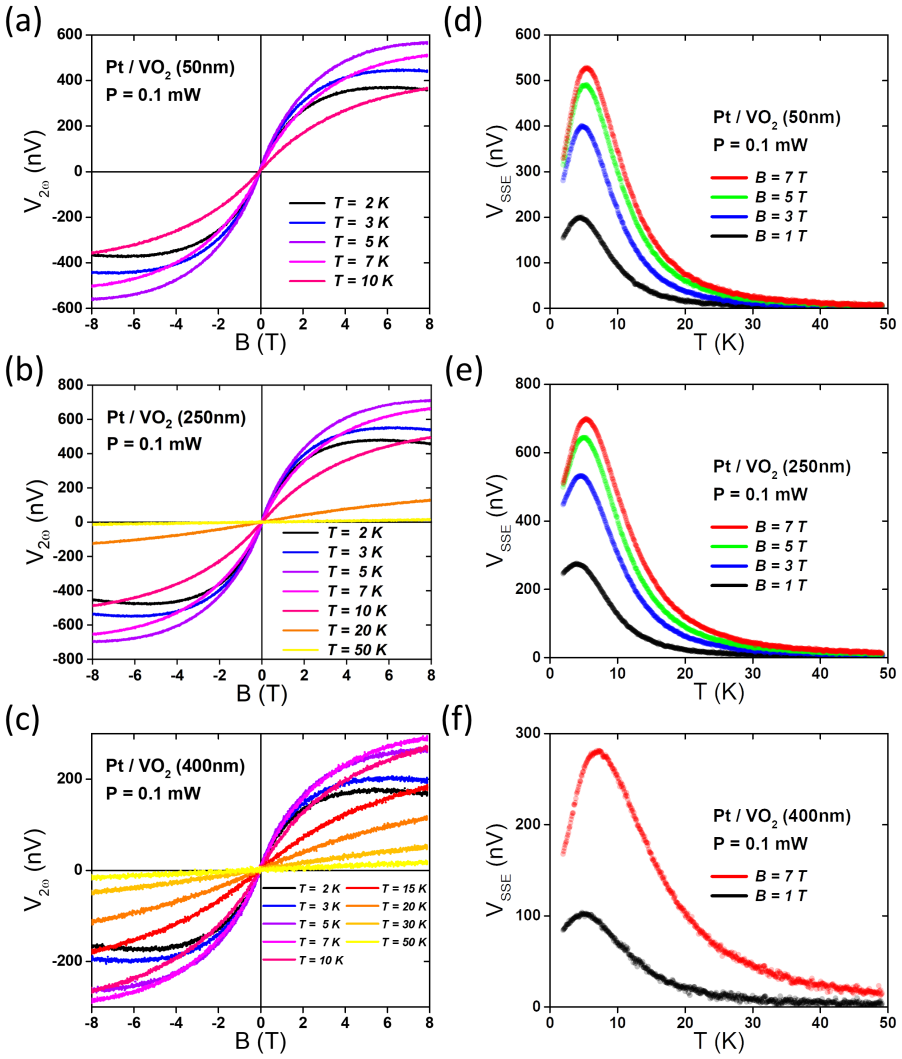

Figure 4.10 : (a-c) The field dependence of the second harmonic voltage for other film thicknesses (50 nm, 250 nm, 400 nm) in Pt/VO_2 devices at different temperatures. (d-f) The temperature dependence of the LSSE voltage for other film thicknesses (50 nm, 250 nm, 400 nm) in Pt/VO_2 devices at different fields.

implying an intrinsic mechanism in VO_2 related to its magnetization.

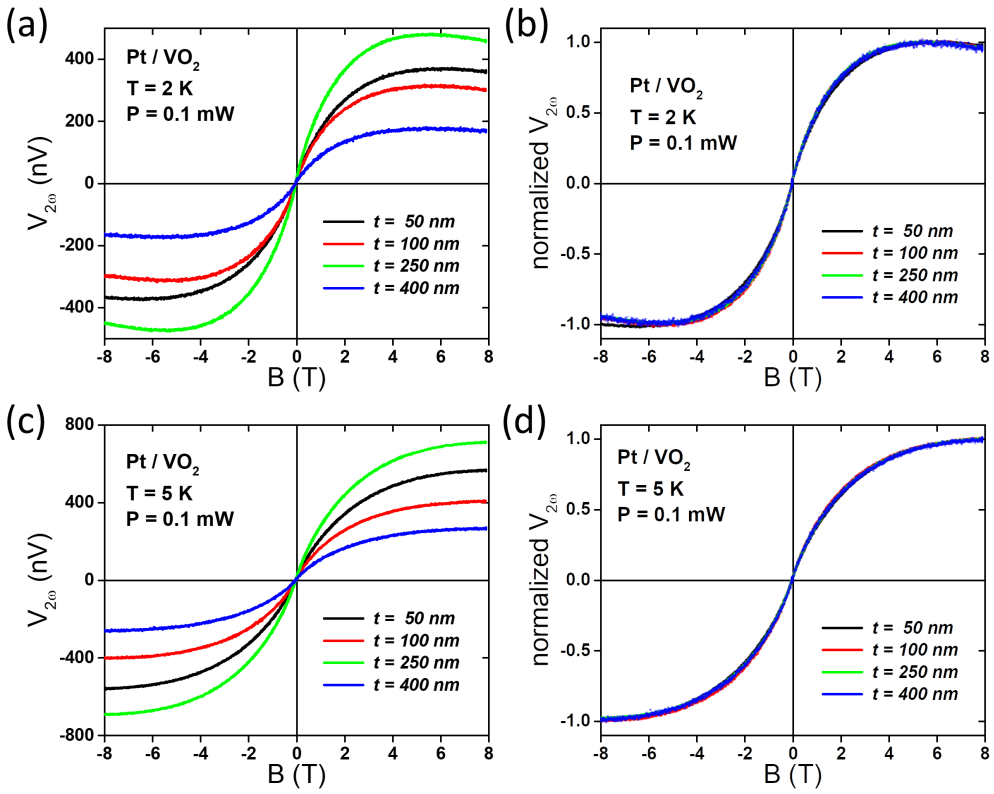

Figure 4.11 : (a) The field dependence of the second harmonic voltage for different thicknesses in the Pt/VO_2 device at 2 K shows no systematic trend of the magnitude of the LSSE voltage with film thickness. (b) When normalized to the maximum value for each film, the second harmonic voltage shows essentially identical dependence on the field, indicating a consistent mechanism associated with the VO_2 material. (c) The field dependence of the second harmonic voltage for different thicknesses in Pt/VO_2 device at 5 K. (d) The same dataset in (c) with normalization.

4.4 Conclusion

We find a strong, temperature-dependent local spin Seebeck response in thin films of VO_2, comparable to that observed in YIG, even though stoichiometric VO_2 is expected to be magnetically inert. The sign of the measured LSSE voltage is incompatible with thermally activated triplons as the spin-carrying excitations. While an interfacial SSE model between a paramagnetic insulator and the strong spin-orbit

metal is qualitatively consistent at fixed temperatures with the nonmonotonic field dependence observed at the lowest temperatures, the temperature and field dependence of the data and prior nonlocal measurements support a bulk SSE interpretation. Additional studies of paramagnetism in the monoclinic phase of VO_2 are required to resolve the nature of spin transport in this correlated system.

4.5 Supplementary information

4.5.1 Angle dependence of the LSSE

Fig. 4.12a shows the field dependence of the second harmonic signal at T = 5 K with different in-plane field orientations. The sign of the signal is opposite for 0° and 180°, and the signal at 90° is almost zero, consistent with the expected symmetry of ISHE and the device geometry. Fig. 4.12b shows the temperature dependence of the SSE response at different angles. The peak temperature where the response reaches the maximum is independent of angle, and the amplitude of the signal scales as $\cos\alpha$, as expected. To show this more readily, we normalized the response to set the maximum to 1 and found that the SSE responses at different angles lie on the same curve (Fig. 4.12c). To conclude, the change of field orientation only affects the overall magnitude of the SSE response. These dependences are consistent with what is expected for the spin Seebeck effect.

4.5.2 Effect of the heater power

The driving force of SSE, either the temperature gradient across the bulk of the VO_2, or the temperature difference at the interface between VO_2 and Pt, is proportional to the heater power. In the absence of self-heating effects, it is expected that

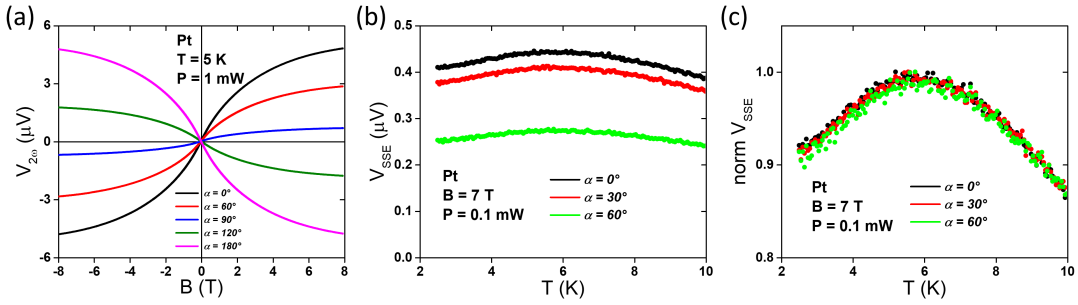

Figure 4.12 : (a) The second harmonic voltage as a function of field at 5 K for Pt at various in-plane field orientations. (b) Temperature dependence of the LSSE voltage, defined here as the difference between the second harmonic voltages at 7 T and 0 T, in the Pt wire at constant heater power of 0.1 mW and different angles. (c) The same data when the maximum value of the voltage in (b) is normalized to 1.

the signal should fall on the same curve when normalized to the heater power. However, our observations indicate that self-heating can play a role at high heater powers and low temperatures. Fig. 4.13 shows the field dependence of the second harmonic signal at 1.8 K with different heater powers in the 14T-DynaCool. With increasing the heater power, the field where the signal reaches the maximum gets larger. A simple explanation is that the high heater power inevitably increases the temperature of the Pt and VO_2 significantly above the cryostat temperature, and then a larger field is needed to let the Zeeman energy balance the thermal energy.

4.5.3 Nernst measurements on a control device

To show the normal Nernst response is much smaller compared to the SSE response, and to confirm that the measurements reflect interfacial processes between the Pt and VO_2, we also characterized a device made with a 10-nm-thick insulating SiO_x spacer layer inserted between the Pt detector wire and the 400-nm-thick VO_2 thin film, to block spin current. As shown in Fig. 4.14a, the signal is roughly linear

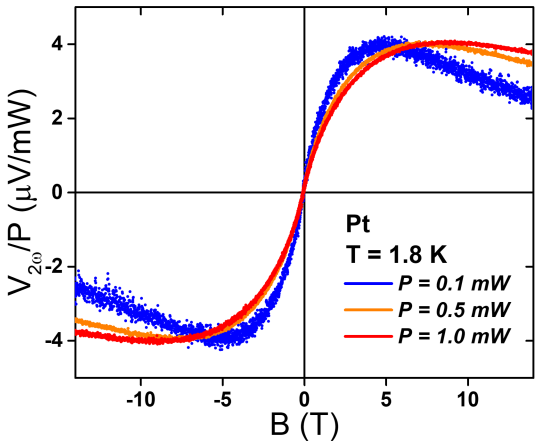

Figure 4.13 : Field dependence of the ratio of second harmonic voltage to the heater power at a cryostat temperature of 1.8 K for three heater powers. The trend here is consistent with the higher heater powers elevating the local Pt temperature significantly above the cryostat temperature.

to the applied field, similar to that was reported in [129]. This signal results from the ordinary Nernst-Ettingshausen response of the sputtered Pt metal. The normalized signal in Fig. 4.14b shows that the SSE response is much larger than the Nernst response.

4.5.4 Estimation of spin Seebeck coefficient and spin Seebeck resistivity in vanadium dioxide

The comparison of spin Seebeck effect between different materials and the quantitative extraction of the precise thermodynamic coefficient ideally require knowledge of the exact temperature profile across the full stack, which, in our case, is Au-SiO_x-Pt-VO_2-sapphire-cryostat stack. This information, however, is extremely difficult to obtain in general, especially for thin film samples and across buried dielectric interfaces. There is no natural, reliable way to measure the temperature of the sapphire

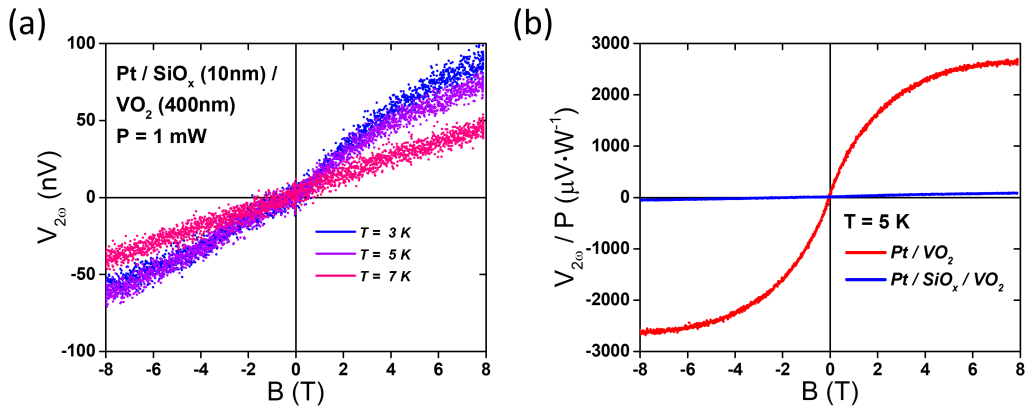

Figure 4.14 : (a) The field dependence of the second harmonic voltage in a $Pt/SiO_x/VO_2$ device at several temperatures. (b) Comparison of the normalized second harmonic voltage to heater power for the Pt/VO_2 device and the $Pt/SiO_x/VO_2$ device on the same VO_2 film at 5 K.

adjacent to the sample board, and similarly there is no way to measure any interfacial temperature difference at the boundary between the VO_2 film and the underlying sapphire, or between the Pt ISH detector and the VO_2 film.

There are two main approaches for quantitative comparisons of the magnitude of the LSSE response between different materials and experimental setups. One figure of merit is the actual spin Seebeck coefficient [27, 28], $\sigma_{SSE} = (V_{SSE}/l)/(\mathrm{d}T/\mathrm{d}z)$, where l is the length of the Pt detector, and $\mathrm{d}T/\mathrm{d}z$ is the temperature gradient through the magnetic material along the direction of heat flow. An alternative figure of merit, formulated knowing that the interfacial temperature differences can be relevant and are difficult to measure, is the spin Seebeck resistivity [29], defined as $R_{SSE} = (V_{SSE}/l)/j_Q$, where j_Q is the heat flux through the SSE insulator. Below we estimate both σ_{SSE} and R_{SSE} for the Pt/VO_2 devices and find responses comparable to that was observed in the ordered magnetic materials such as YIG.

We roughly estimate the temperature gradient across the VO_2 film in a typical

device, given by $\mathrm{d}T/\mathrm{d}z = \dot{q}/(\kappa_{VO_2}A)$, where $\dot{q}$ is the heater power transported vertically through the Pt/VO_2 interface, κ_{VO_2} is the thermal conductivity of VO_2 film, and A is the cross-sectional interface area for the transport. Finite-element thermal modeling (see the subsection 4.5.6) supports the conjecture that in our measurement setup, for reasonable values of thermal boundary resistance parameters, the heat flux through the VO_2 film is approximately constant as a function of temperature, which means the dominant thermal path for power generated in the heater is downward through the VO_2 film. Note that the Pt detector wire is 800 μm long while the Au heater wire is 1300 μm long; thus, for a total heater power of 1 mW in Au wire, at most about 0.615 mW of the heater power is transported downward through the Pt wire; larger thermal boundary resistances would reduce this fraction.

To the best of our knowledge, no data is available for the cross-plane low temperature thermal conductivity κ_{VO_2} of VO_2. Directly measuring the low temperature cross-plane thermal conductivity of the VO_2 films is very difficult. The most common approach (the 3ω method [132]) is not applicable at low temperatures because the T-dependence of the typical heater material (Pt) resistivity vanishes below about 20 K (that is, $\mathrm{d}R/\mathrm{d}T \to 0$). Optical techniques [133] that rely on thermal expansion of the film material similarly do not perform at low temperatures because the temperature-dependent thermal expansion coefficient is suppressed at low temperatures. We can get a rough estimate of the thermal conductivity from the kinetic theory approach, using $\kappa_{VO_2} = (1/3)Cv_s l_m$, where C is the temperature-dependent specific heat per unit volume, v_s is the transverse speed of sound, and l_m is an effective phonon mean free path. This assumes phonon diffusion, so self-consistency would require it to be applied to films thicker than phonon mean free path and thicker than a typical thermal phonon wavelength. At 10 K, specific heat of VO_2 was reported to be 15.4

mJ/(mol K) [134], and converting into per-unit-volume, 848 J/(m^{3}K). A reasonable speed of sound is 4500 m/s [135], giving a thermal phonon wavelength at 10 K of about $hv_s/k_BT = 22$ nm. For consistency with the idea of diffusive phonon conduction, we can assume a phonon mean free path smaller than the film thickness; should the phonon mean free path be comparable to the film thickness, the cross-plane thermal conductivity would be larger by up to a factor of order 3. Assuming a thermal phonon mean free path of 100 nm and diffusive phonon transport implies a κ_{VO_2} thermal conductivity close to 0.13 W/(mK) at 10 K. Then given $A = 8 \times 10^{-9}$ m^2, this would imply a temperature gradient across a 250-nm-thick film of $\mathrm{d}T/\mathrm{d}z = 5.91 \times 10^4$ K/m at a sample temperature of 10 K with the applied total heater power of 0.1 mW. (Thermal boundary resistances would reduce this thermal gradient by favoring lateral heat conduction out of the heater, rather than vertical heat transport. Thus, the estimates of σ_{SSE} and R_{SSE} that we find here are likely underestimates.)

Using the temperature gradient in VO_2, we can then compare SSE in VO_2 and YIG in terms of spin Seebeck coefficient $\sigma_{SSE} = (V_{SSE}/l)/(\mathrm{d}T/\mathrm{d}z)$, where l is the length of the Pt detector, and $\mathrm{d}T/\mathrm{d}z$ is the temperature gradient estimated above. In the device on the 250-nm-thick VO_2 film, V_{SSE} is $\sim$ 500 nV at 10 K and 8 T, giving an estimated σ_{SSE} of 10 nV/K. At low temperatures in YIG, σ_{SSE} is measured around 5 μV/K for bulk [28]. Considering the thickness dependence of the magnon SSE [95,96], and the magnon diffusion length in a 210-nm-thick YIG at 10 K reported to be 8 μm [77], the coefficient σ_{SSE} is estimated to be 70 nV/K in YIG for a film 250 nm thick. This differs from the VO_2 estimate only by a factor of 7; a larger VO_2 thermal conductivity and important thermal boundary resistances would imply a larger estimated σ_{SSE} for VO_2, closer to the YIG value.

Given the uncertainties associated with interfacial thermal resistances and the

difficulty in measuring temperatures of every material at each interface, an alternative approach to comparing SSE responses between materials uses the spin Seebeck resistivity [29], $R_{SSE} = (V_{SSE}/l)/j_Q$, where j_Q is the heat flux through the insulator. In YIG, R_{SSE} was reported to be $\sim$ 10 nm/A for a 100-nm-thick film at 10 K [29]; and in the 100-nm-thick VO_2, using the heat flux computed from a total heater power of 0.1 mW and the device dimensions, R_{SSE} is $\sim$ 65 nm/A at 10 K and 8 T, even larger than that in YIG.

In summary, the magnitude of the longitudinal SSE response in VO_2, a nominally non-magnetic material, is comparable in magnitude to the SSE response of YIG thin films.

4.5.5 Measurements of the temperature rise of the full stack

We use the Johnson-Nyquist (JN) noise in the Pt detector itself under different heater powers to estimate quantitatively the temperature difference between the Pt and the cryostat. The details of the method have been reported elsewhere [129]. Fig. 4.15a shows the temperature rise ΔT_{Pt} (above the cryostat temperature measured using a Cernox thermometer) determined from JN noise in the Pt wire as a function of heater power at the cryostat temperature of 5 K for a 100-nm-thick VO_2 film sample, while Fig. 4.15b shows the temperature dependence of ΔT_{Pt} at fixed heater power of 1 mW. ΔT_{Pt} grows linearly in the low heater power region and decreases with increasing temperature, similar to that observed in the Pt/SiO_2 interface [129].

4.5.6 Thermal model of SSE device on vanadium dioxide

To aid in a quantitative estimate of the LSSE response (subsection 4.5.4), we constructed a finite element thermal model using COMSOL, in part to test the common

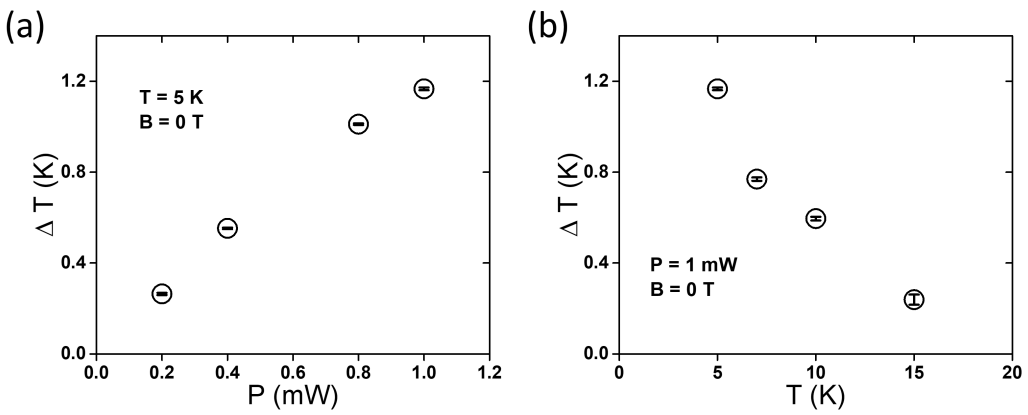

Figure 4.15 : (a) Temperature rise of Pt wire as a function of heater power at the cryostat temperature of 5 K as found via Johnson-Nyquist noise thermometry. (b) Temperature rise of Pt wire at fixed heater power of 1 mW as a function of cryostat temperature.

assumption that all heat generated by the Au heater wire travels straight downwards, heating the area of the substrate directly below the Pt detector wire. To produce the thermal model, we used thermal conductivity values at 10 K for the VO2 (estimated above in subsection 4.5.4), Al_2O_3 [136], and SiO_x [137] of 0.13, 85, and 0.1 W/(mK), respectively.

In addition to contributions from the bulk layers as above, the total thermal path between the Pt ISH detector and the cryostat also involves several thermal boundary resistances (BRs). The data in Fig. 4.15 demonstrate that these thermal resistances are not negligible, as to reproduce the directly measured temperature of Pt wire, the total thermal resistance from Pt to the substrate must be roughly two orders of magnitude larger than the thermal resistance of the material layers themselves. BRs across metal/dielectric interfaces are expected to be the largest since the thermal conduction mechanism changes at those interfaces from electron-dominated transport to phonon transport, as well as due to acoustic velocity mismatch between materials. Di-

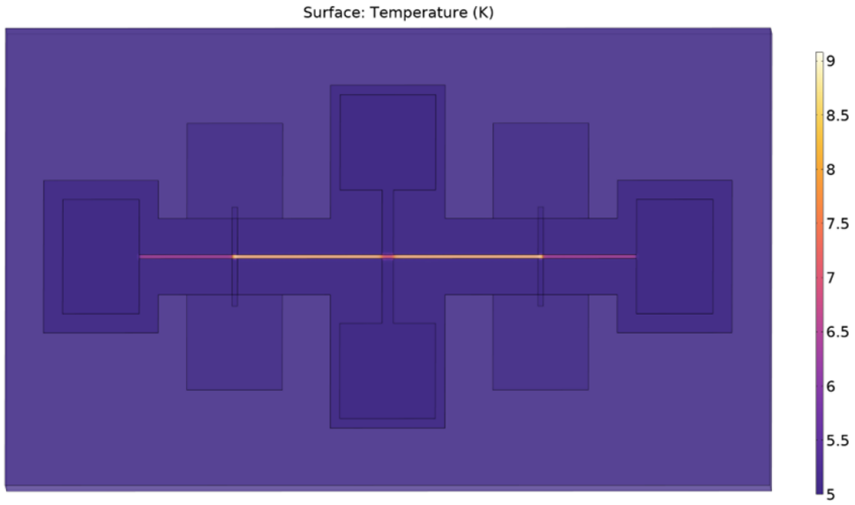

Figure 4.16 : Top view of the temperature profile of the thermal model for the SSE device on VO_2. Heat enters the Au heater wire and exits at the bottom of the substrate which is held to a cryostat temperature of 10 K. The Au wire is colder in the very center because of lateral conduction to non-heated Au contacts. The Au wire is also colder at its ends because there it is not over the Pt wire and thus the thermal path of the heat involves fewer thermal boundary resistances (main thermal resistance contributors).

rectly measuring the thermal BRs is very difficult in practice; worse still, they depend strongly on materials, interface quality, and deposition method (e.g. evaporation or sputtering). Our approach is to insert thermal BRs at the metal/dielectric interfaces in the model and then vary the value of the BRs until the temperature of the Pt wire in the simulation equals the temperature of the Pt wire directly measured using JN noise thermometry. For a heater power of 1 mW, at cryostat temperatures of 5 K, 10 K, and 15 K, the Pt temperature is 6.2 K, 10.6 K and 15.3 K (Fig. 4.15b). To reproduce these Pt wire temperatures in the simulation, it requires the total thermal BRs of 18.9, 9.0, and 2.75 μKm^2/W, respectively.

Quantifying the LSSE as either the SSE coefficient, σ_{SSE}, or the spin Seebeck resistivity, R_{SSE}, requires an estimate of the fraction of heat generated that is trans-

ported vertically through the insulating VO_2 below the Pt ISH detector. Assuming these thermal BRs make the model accurately describe the actual device, we can then estimate how much heat travels down to the Pt wire and how much travels sideways in the SiO_x layer. For cryostat temperatures of 5 K, 10 K, and 15 K, 78.3 %, 75 %, and 81.9 % of the heat current enters the top of the Pt wire (over 98 % of this heat current then enters the sapphire substrate directly below the Pt detector wire), and the rest travels sideways, not contributing to the detected spin Seebeck effect. If no thermal BRs are included, then 92 % of the heat current reaches the top of the Pt wire and the Pt temperature only increases by 0.15 K regardless of cryostat temperature. This demonstrates that the temperature gradient in the VO_2 film $\mathrm{d}T/\mathrm{d}z$ and the heat flux across the VO_2 film j_Q are overestimated by assuming all generated heat travels directly downwards, and thus the VO_2 spin Seebeck coefficient and spin Seebeck resistivity estimated in the main text are underestimates.

Chapter 5

Low Temperature Longitudinal Spin Seebeck Effect in Antiferromagnetic Vanadium Sesquioxide

This chapter will mainly show a local spin Seebeck response in antiferromagnetic vanadium sesquioxide (V_2O_3) thin films as a function of temperature, magnetic field, and film thickness using Pt electrodes. At a fixed heater power, the SSE response develops with increasing external field until it approaches saturation, with a non-monotonic temperature dependence, having a pronounced peak at low temperatures that shifts toward higher temperatures. The peak temperature increases with increasing field. In contrast to the response observed in paramagnetic VO_2, the SSE signal in V_2O_3 consistently decreases as a function of film thickness, implying that the measured response stems from the bulk. These results are interpreted in the context of AFM magnon expectations, suggesting that the length scale for thermal relaxation between magnons and phonons in V_2O_3 is shorter than 50 nm, consistent with the wealth of experimental support for strong spin-lattice interactions in this material. This chapter is largely based on a manuscript in preparation.

5.1 Properties of vanadium sesquioxide

Vanadium sesquioxide (V_2O_3), as an archetypal material with strong electronic correlations, undergoes a high-temperature rhombohedral paramagnetic metal to a low-temperature monoclinic antiferromagnetic insulator (AFI) transition with a transition temperature of around 160 K. Neutron diffraction [138] reveals a magnetic order

where V moments are ferromagnetically coupled in the monoclinic (010) layers tilted away from the hexagonal c-axis by 71°, with a reversal between adjacent layers (Fig. 5.1). The ordered moment is (1.2 ± 0.1) μ_B per V atom, and the spin excitation gap is around 4.75 meV (1.15 THz, or 55 K) [139]. Resonant x-ray scattering experiments at the vanadium K edge found additional Bragg peaks due to the long-range order of 3*d* orbitals occupancy and demonstrated the existence of orbital ordering in V_2O_3, which could account for the complex magnetic structure of V_2O_3 [140]. While V_2O_3 has often been discussed as an example of a Mott insulator, it's clear that the situation is quite subtle [141]. The nature of the metal-insulator phase transition in V_2O_3 is complicated, with strong couplings between spin, lattice, and charge degrees of freedom [142]. The AFM order in V_2O_3 takes effect in Ni/V_2O_3/permalloy spin-valve devices, showing unexpected behavior in the temperature dependence across the V_2O_3 metal-insulator transition [143]. The AFM order can also significantly enhance the exchange bias of the attached ferromagnetic permalloy layer which appears at the onset of the transition temperature [144]. However, to date, spin caloritronics measurements have not been applied to this system.

5.2 Device fabrication and experimental setup

In the on-chip-heating configuration for detecting the longitudinal SSE(LSSE) [23], an alternating current at angular frequency ω is applied to a heater wire. Local Joule heating generates a temperature gradient along the normal direction of the film surface, oscillating at 2ω, which in turn drives a spin angular momentum current. A transverse voltage at 2ω can be detected at a nearby inverse spin Hall (ISH) detector made from a strong spin-orbit metal (e.g., Pt, W) when the magnetization of the insulator is properly oriented. V_2O_3 thin films with different thicknesses (50 nm, 100

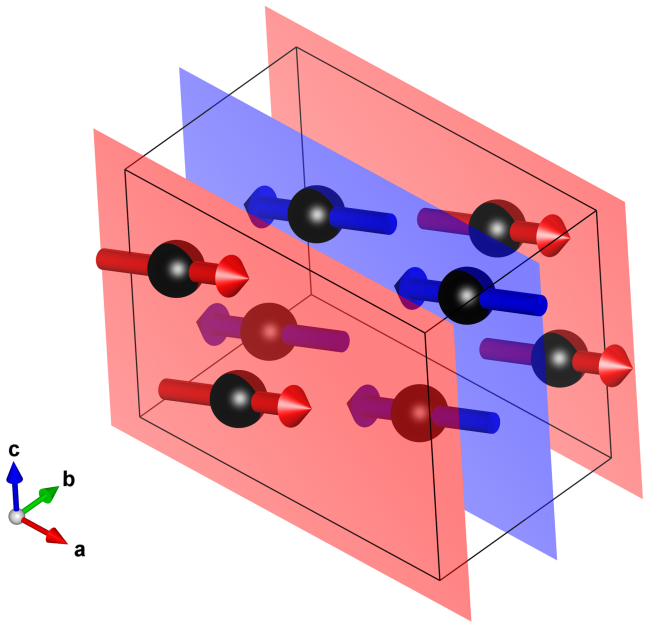

Figure 5.1 : Crystal structure of V_2O_3 in the low temperature, insulating monoclinic phase. The black spheres represent V atoms, with red and blue arrows showing the spin direction. The moments of V atoms are aligned ferromagnetically on the (010) plane and reverse between the neighboring layers. Oxygen atoms are omitted for clarity. The crystal structure is generated by VESTA [125].

nm, 250 nm, 400 nm) were grown epitaxially on r-cut sapphire substrates via RF magnetron sputtering. Due to the lattice match, the V_2O_3 thin film favors (011)-oriented texture, where the moments of V are almost parallel to the surface, and the surface is nominally magnetically compensated. The Pt (or W) wire, 800 μm long, 10 μm wide, and 10 nm thick, is directly deposited on the V_2O_3 film surface using standard photolithography, magnetron sputtering, and a liftoff process. A SiO_x layer with a thickness of 100 nm and an Au heater wire (1300 μm long, 10 μm wide, 50 nm thick) were then fabricated above the Pt (or W) wire by photolithography, e-beam evaporation and liftoff. The Au heater wire and the Pt detector wire are electrically isolated by the SiO_x layer in between. An AC current at angular frequency

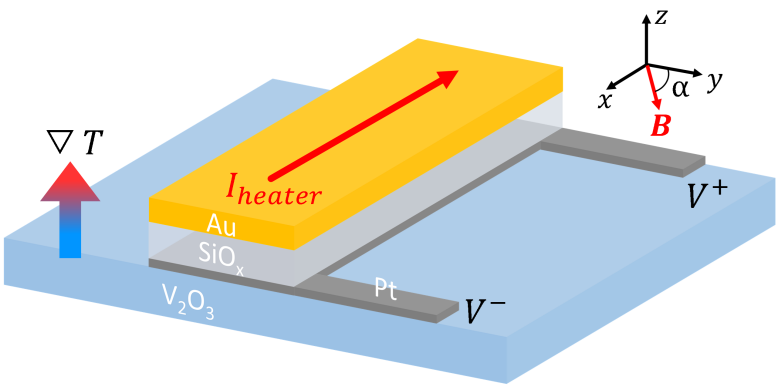

Figure 5.2 : Schematic of local spin Seebeck measurement. An AC heater current produces an oscillating z-directed temperature gradient. A vertical (z-directed) thermal spin current with the y component of the magnetization of the V_2O_3 could produce an ISH voltage along the x-directed strong spin-orbit metal wire.

$\omega = 2\pi \times$ (7.7 Hz) is driven through the Au wire, while the voltage across the Pt (or W) wire is recorded at 2ω using a lock-in amplifier. The measurements are performed as a function of temperature and field in a Quantum Design Physical Property Measurement System (9T-PPMS) equipped with a rotation stage.

5.3 Results

5.3.1 Field strength dependence

The magnetic field dependence of the second harmonic voltage $V_{2\omega}$ is shown for Pt/V_2O_3 (100 nm thick) device (Fig. 5.3a,b) when the field is applied in the film plane and perpendicular to the Pt wire ($\alpha = 0°$). At $T = 2$ K, a pronounced $V_{2\omega}$ signal appears, whose sign changes with respect to the $\boldsymbol{B}$ direction, reflecting the symmetry of the ISHE. The magnitude of the signal grows approximately linearly near $\boldsymbol{B} =$ 0 T, then saturates at high fields at 5 T. A full sweep of the field from +8 T to -8 T exhibits no hysteresis. As temperature increases from 2 K, the overall magnitude

of $V_{2\omega}$ increases, and the saturation region shifts to higher fields. However, above 7 K, the magnitude of the signal begins to decrease, and the saturation behavior disappears. The signal vanishes at $T = 50$ K. When normalizing the signal by its maximum value at 8 T at each temperature, the nonlinear curvature becomes clear at $T = 2$ K (Fig. 5.3c). As temperature goes up, this nonlinearity becomes weaker with the decrease of the zero-field slope. The field dependence of $V_{2\omega}$ closely parallel to that has been reported in uniaxial AFI MnF_2 [54], FeF_2 [55] with field along their easy axis below the spin-flop fields and also in insulating $SrFeO_{3-\delta}$ thin film [60]. Recently, a similar behavior was reported in uniaxial AFI Cr_2O_3 when field is applied along its hard-axis and interpreted as paramagnetic SSE from weakly interacting spins near the Cr_2O_3 surface [52], since the responses are well-fitted using the Brillouin function with weak antiferromagnetic interactions.

The voltage responses for devices with Pt and W detector are of opposite signs (as shown in Fig. 5.3d), consistent with a genuine spin current effect, since Pt and W are known to possess spin Hall angles of opposite sign [15]. Aside from this sign reversal, the field dependence of the voltage in Pt/V_2O_3 and W/V_2O_3 is similar, indicating they are of the same origin.

5.3.2 Field orientation dependence

We checked the magnetic origin of the measured signal by rotating the in-plane magnetic field while keeping the field magnitude constant ($|\boldsymbol{B}| = 1$ T, 3 T, 5 T, 7 T) at 3 K. A cosine dependence was observed, as shown in Fig. 5.4a. The voltage gets the maximum or minimum values when the field is perpendicular to the wire; and the voltage crosses zero when the field aligns along the wire. Since the voltage is from ISHE given by $E_{ISHE} \propto J_s \times \sigma$, where J_s is the interfacial spin current density, σ is

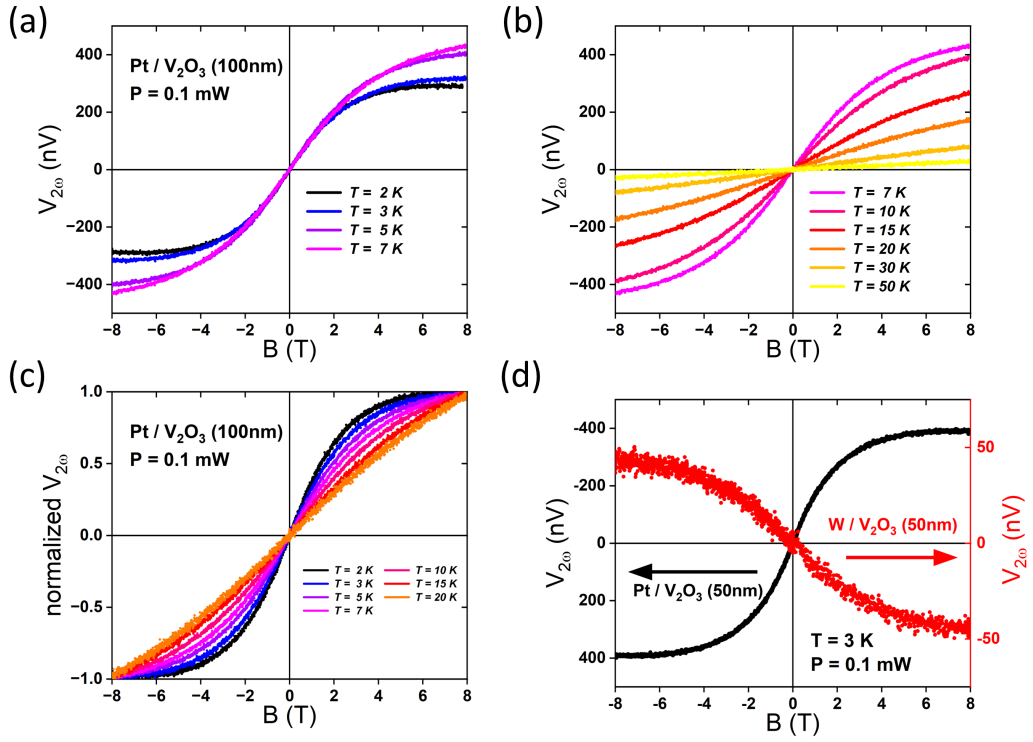

Figure 5.3 : (a,b) The second harmonic voltage as a function of field ($\alpha = 0°$, $\boldsymbol{B}\|$y) at various temperatures for Pt detector wires on 100 nm thick V_2O_3. (c) The same dataset in (a,b) with normalization to the maximum value at each temperature. A transition from nonlinearity to linearity can be seen as temperature increases. (d) Comparison between voltage responses of Pt/V_2O_3 and W/V_2O_3 devices at 3 K with an applied heater power of 0.1 mW.

the spin-polarization vector; in our setup, J_s is always directed along z-axis parallel to the temperature gradient and σ aligns with the magnetization. This cosine dependence suggests that as the field rotates in-plane, either the magnetization of V_2O_3 is unchanged while J_s changes, or J_s remains the same while the magnetization of the V_2O_3 moments coupled to the Pt conduction electrons follows the field orientation. The former idea is suggested in FeF_2 [55] that as the field rotates, the magnetic field component projected to the y-axis (perpendicular to the wire) oscillates; so do the Zeeman splitting of the two antiferromagnetic magnon eigenmodes, and the resulting

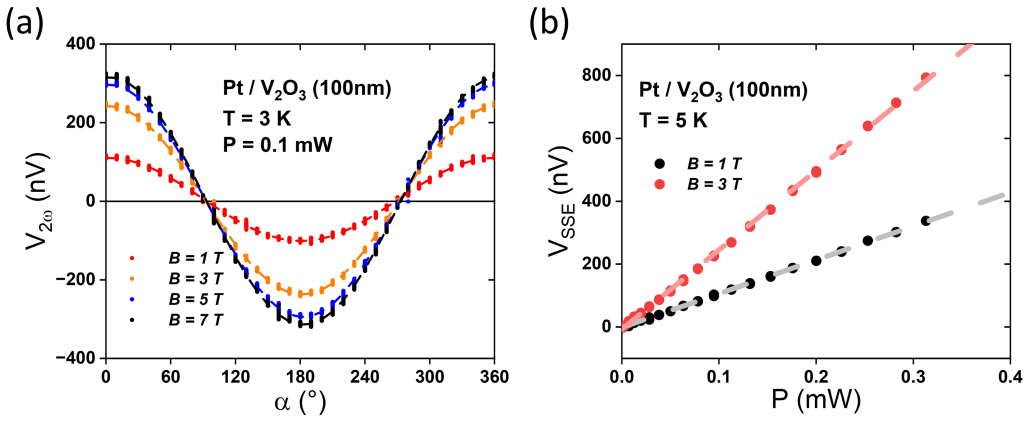

Figure 5.4 : (a) Dependence of the second harmonic signal in Pt wire at 3 K with 0.1 mW heater power on in-plane field orientation α, showing expected cosine dependence. (b) Dependence of the spin Seebeck voltage on the heater power at 3 K and 0°. The SSE voltage is defined as the difference of the second harmonic signals between zero-field and 1 T or 3 T. The dark dots are the measurement data, with corresponding light dash lines showing linear behavior.

spin current induced SSE signal. The latter idea shares the same explanation for SSE in ferrimagnets and paramagnets, that the magnetization of the magnon branch coupled to the Pt conduction electrons points along the applied field.

5.3.3 Heater power dependence

The 2ω voltage signal scales linearly with the applied heater power at fixed $\boldsymbol{B} = 1$ T and 3 T oriented at $\alpha = 0°$ (Fig. 5.4b), as expected for an SSE signal. A potential confounding effect in this experimental geometry, the ordinary Nernst response of Pt (W), is expected to be linear with the applied magnetic field, and thus cannot explain the observed nonlinear magnetic field dependence of $V_{2\omega}$ shown in Fig. 5.3. Furthermore, the previous study with the Pt wire deposited directly on the SiO_2/Si substrate using the identical geometry yields the signal of only ~ 3 μV/(TW) [129], two orders of magnitude smaller than those measured in Pt/V_2O_3 devices.

5.3.4 Temperature dependence

To elucidate the mechanism driving the spin Seebeck response in V_2O_3, we examined its temperature dependence. Fig. 5.5a shows the temperature dependence of LSSE voltage response in the same Pt/V_2O_3 device across temperatures from 2 K to 50 K under fixed heater power and different magnetic fields. At each field, the LSSE voltage increases as temperature decreases, reaches a maximum at a peak temperature T_{peak}, and then diminishes with further reducing temperature. Such peak behavior is also observed in ferrimagnet $Y_3Fe_5O_{12}$ (YIG) [28] and AFI MnF_2 [54] and FeF_2 [55] as well. In YIG, the peak temperature in SSE response correlates with the peak temperature of the thermal conductivity of YIG [28], explained by the phonon-drag mechanism, where temperature-gradient-driven phonons induce the spin current via magnon-phonon interactions. In this case, the phonon-drag model [96] predicts $V_{SSE} \propto \kappa \nabla T = j_q$, where κ is the thermal conductivity of YIG, ∇T is the temperature gradient in YIG, and j_q is the heat flux through the Pt/YIG interface. However, j_q is fixed in our measurement method, contrary to the observed temperature dependence. In MnF_2 and FeF_2 [54, 55], the peak behavior is explained by the antiferromagnetic magnon modes. The uniaxial AFI has two magnon modes (α and β) with opposite chirality. Since β mode lies below α mode under an external field, only the β mode magnons are predominately populated at low temperatures. As temperature increases, the β mode magnons population continues to increase until the α mode magnons start to be occupied. Because of the opposite angular momentum between α mode and β mode, the increasing temperature results in a peak in the net spin current and consequently a peak in SSE. Furthermore, in V_2O_3, the peak temperature increases with increasing fields (Fig. 5.5b), similar to that in MnF_2; however, in FeF_2, the peak temperature remains the same for all the fields. No na-

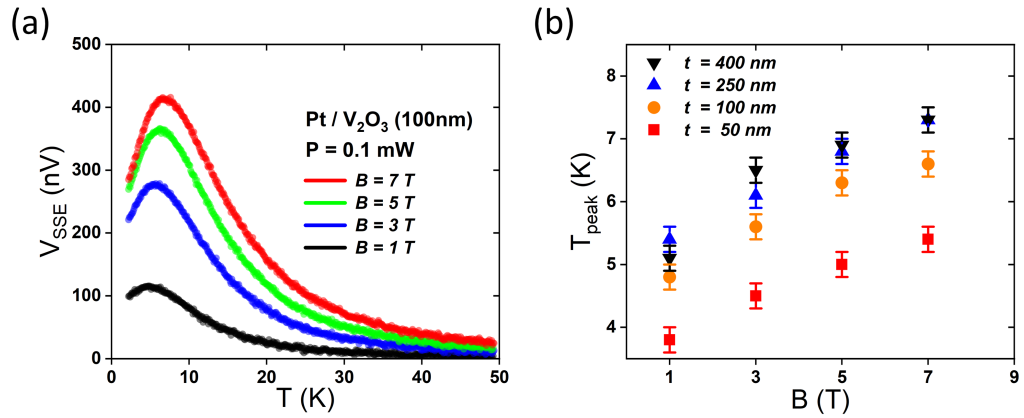

Figure 5.5 : (a) Temperature dependence of the LSSE voltage, defined as the difference of the second harmonic voltages between at a praticular field and 0 T, in the Pt/V_2O_3 device at constant heater power of 0.1 mW and $\alpha = 0°$. (b) Field dependence of the peak temperature of the LSSE signal in devices on different thicknesses of V_2O_3. For each thickness, the peak temperature approximately linearly increases with the field.

ture explanation can be given for now. The qualitative temperature dependence and its variation with field (higher field leads to higher peak temperature) is very similar to what is observed in VO_2 (see chapter 4). We discuss this further in Sec. 5.4.2.

5.3.5 Thickness dependence

The LSSE in AFI has both a bulk contribution [97, 98] from the temperature gradient in the AFI and an interfacial contributios [99, 100, 103, 145] from temperature difference between magnon temperature in the AFI and electron temperature in the spin-orbit metal. To distinguish dominating bulk or interfacial contribution, we fabricated devices with the identical geometry following the same fabrication protocols but varying thicknesses of V_2O_3 films. All devices show similar magnetic field dependence and temperature dependence, such as linear growth at zero field and saturation at high field, weaker nonlinearity with higher temperature, peak behavior with temperature, and increasing peak temperature with increasing field (Fig. 5.6). The

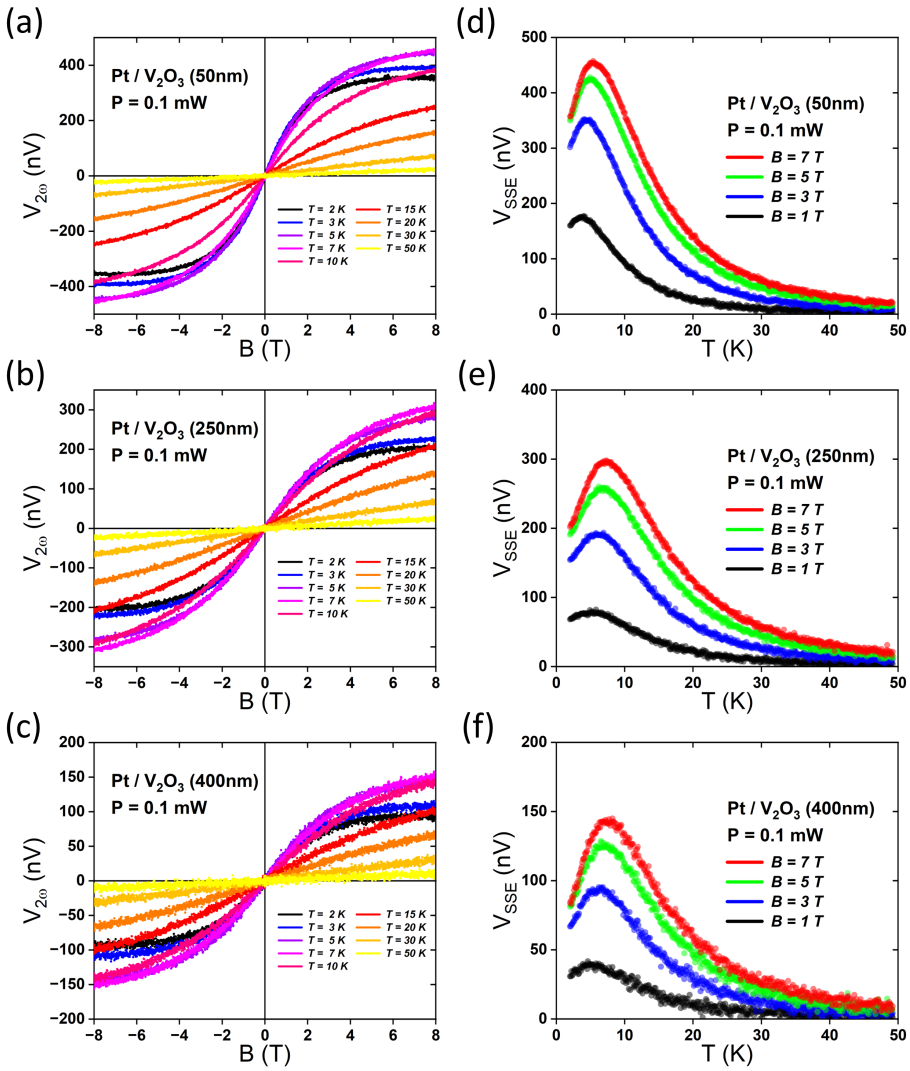

Figure 5.6 : (a-c) The field dependence of the second harmonic voltage for other film thicknesses (50 nm, 250 nm, 400 nm) in Pt/V_2O_3 devices at different temperatures. (d-f) The temperature dependence of the LSSE voltage for other film thicknesses (50 nm, 250 nm, 400 nm) in Pt/V_2O_3 devices at different fields.

magnitude of the signal decreases consistently as the thickness increases (Fig. 5.7a), and the peak temperature at each field shifts upward for thicker film (Fig. 5.5b). When normalizing to its maximum value, the normalized LSSE voltage as a function of field are different at T = 2 K, with thinner films showing a steeper slope at zero

field (Fig. 5.8a). When the temperature increases above 3 K, the normalized signal on films thicker than 100 nm are the same, and the signal on the 50 nm thick film still shows a larger slope at zero field (Fig. 5.8b). When the temperature increases above 20 K, the signals on all the thicknesses overlap.

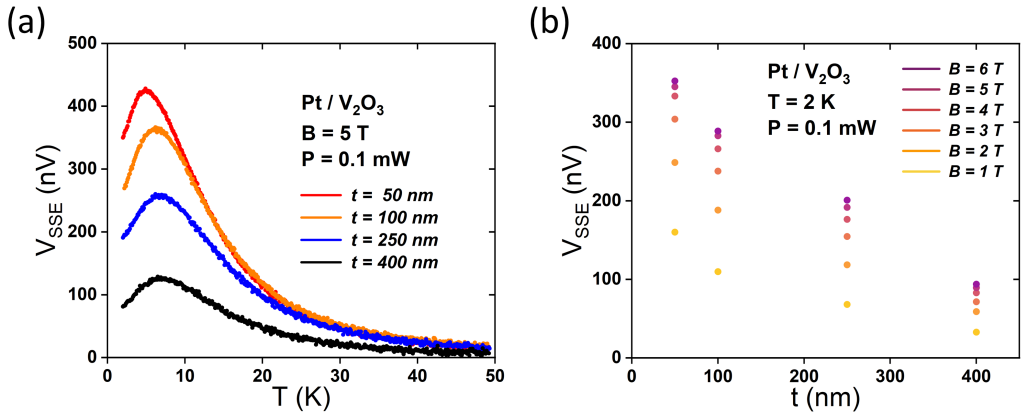

Figure 5.7 : (a) The temperature dependence of the LSSE voltage in Pt/V_2O_3 devices at fixed magnetic field of 5 T and heater power of 0.1 mW for different film thicknesses. (b) The thickness dependence of the LSSE voltage at 2 K in Pt/V_2O_3 devices at different fields. Clearly, as thickness increases, the magnitude of the LSSE voltage decreases.

5.4 Discussions

5.4.1 Magnon energy relaxation length

We now consider possible mechanisms at work in the observed decrease of the SSE signal with increasing film thickness. The spin Seebeck coefficient [27, 28] is defined as $\sigma_{SSE} = (V_{SSE}/l)/(\mathrm{d}T/\mathrm{d}z)$, where l is the length of the ISH detector, and $\mathrm{d}T/\mathrm{d}z$ is the temperature gradient across the insulator. Guo *et al.* found that in YIG films with thicknesses ranging from 150 nm to 50 μm, the magnitude of σ_{SSE} increases gradually with increasing thickness, saturating beyond a critical thickness, and the

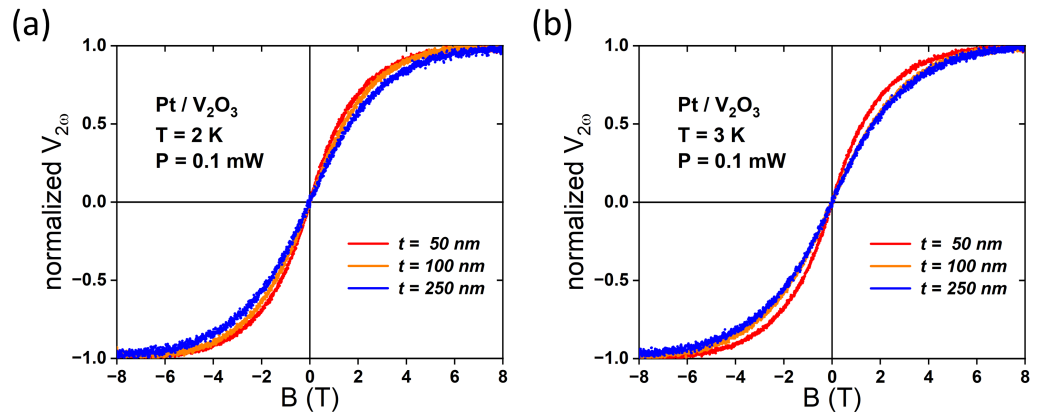

Figure 5.8 : The normalized second harmonic voltage as a function of field in Pt/V_2O_3 devices of different thicknesses at 2 K (a) and 3 K (b).

peak temperature shifts to a higher temperature as the film becomes thinner [27]. These observations are explained by the combination of a temperature-dependent magnon diffusion length $\lambda_m(T) \propto T^{-1}$ and the thermal magnon density $\rho_m(T)$. Only magnons excited within a distance $\sim \lambda_m$ from the interface can reach the detector and contribute to the spin current. Thus, the SSE signal scales as $V_{SSE} \propto \rho_m \times \min(t, \lambda_m)$. As temperature decreases from room temperature, λ_m increases and ρ_m decreases. Initially, the increase in λ_m allows more magnons to reach the interface, enhancing the SSE signal. However, once λ_m reaches the film thickness t, further cooling leads to a drop in ρ_m and causes the SSE signal to decline. This competition leads to a non-monotonic temperature dependence of the SSE signal. In thinner films, λ_m reaches t at higher temperatures, resulting in the shift of the peak to higher temperatures.

In the Pt/V_2O_3/sapphire system, vertical thermal conduction at fixed heater power would imply a fixed interfacial temperature difference $T_p(\mathrm{Pt})$-$T_p(V_2O_3)$ (for unchanging thermal boundary resistance) and a fixed temperature gradient $\nabla T_p(V_2O_3)$ within the film, where $T_p(\mathrm{Pt})$ and $T_p(V_2O_3)$ are the phonon temperature of Pt and

V_2O_3, respectively. If we assume that the spin current is generated from the thermally excited magnons in the bulk V_2O_3, then the spin Seebeck voltage would be expected to increase as the thickness increases and saturate when the thickness reaches λ_m [97, 98]. However, instead we observe a decrease of the signal as the thickness increases. Within this framework, to match the observation would require the interfacial spin mixing conductance to decrease with increasing thickness faster than the increase in the thickness factor, implying that the thicker film has more defects [52].

Another possible explanation for a smaller bulk SSE response with thicker film to consider would be a strong dependence of the crossplane thermal conductivity, $\kappa_{V_2O_3}$, of the V_2O_3 on film thickness. If $\kappa_{V_2O_3}$ improves considerably with increasing thickness, then at fixed heater power the temperature gradient in the film would be lower for thicker films. This requires a thermal conductivity change roughly inversely proportional to the thickness. There is no reason, however, to expect that the crossplane thermal conductivity of the films varies significantly with thickness.

A particular explanation for the observed thickness dependence of the LSSE signal is consistent with the strong spin-lattice coupling known in V_2O_3. An alternative approach to quantifying SSE responses uses the spin Seebeck resistivity [29], defined as $R_{SSE} = (V_{SSE}/l)/j_q$, where j_q is the heat flux through the insulator. Prakash *et al.* found that the SSE was a non-monotonic function of YIG thickness ranging from 10 nm to 1 μm with a peak at $\sim$ 250 nm [29] in the Pt/YIG/gadolinium gallium garnet (GGG) stack, which is explained in terms of the energy-equilibration dynamics of magnons to phonons in the YIG. There is another length scale different from the magnon diffusion length λ_m, the magnon energy relaxation length λ_u, which parametrizes the relaxation of the magnon temperature T_m to the phonon temperature T_p. When the film thickness is close to λ_u, thermalization mechanisms

between magnons in YIG and phonons in GGG lower the magnon temperature T_m near the YIG/GGG interface, which contribute positively to the temperature imbalance $T_p - T_m$ in YIG. However, when the film thickness is larger than λ_u, these magnons thermalize with phonons before reaching the Pt/YIG interface, thus this contribution vanishes, leading to the non-monotonic behavior in thickness. If we assume the spin current is from the difference between T_m and T_p in V_2O_3, then the observed thickness dependence would imply that the decrease in SSE voltage with increasing thickness is a consequence of λ_u being smaller than 50 nm. Further measurements on ultrathin films (i.e., those thinner than 50 nm) and bulk crystals would provide more insights.

5.4.2 Comparison with vanadium dioxide

Our previous studies found that the paramagnetic insulator vanadium dioxide (VO_2) supports the paramagnetic SSE at low temperatures. The current investigation finds that V_2O_3 and VO_2, though magnetically distinct, exhibit SSE signals with the same sign, comparable magnitude under the same heater power with identical geometry, and similar temperature and field dependences (Fig. 5.9). We observed field-induced suppression of the SSE voltage at low temperature and high field in VO_2, whereas V_2O_3 does not exhibit this suppression. Still, the similarities in the responses of the two oxides warrant discussion, and it appears that the interface between oxide and Pt could potentially play a role. Since VO_2 and V_2O_3 were both grown on r-cut sapphire, the (012) plane of Al_2O_3 favors a lattice-matching V atom arrangement analogous to Al atoms on the surface of Al_2O_3, ignoring small lattice distortions. Ideally, it's Pt/oxide interface where the exchange interaction between d electrons of V atoms in the oxide and s electrons in the Pt happens, which induces

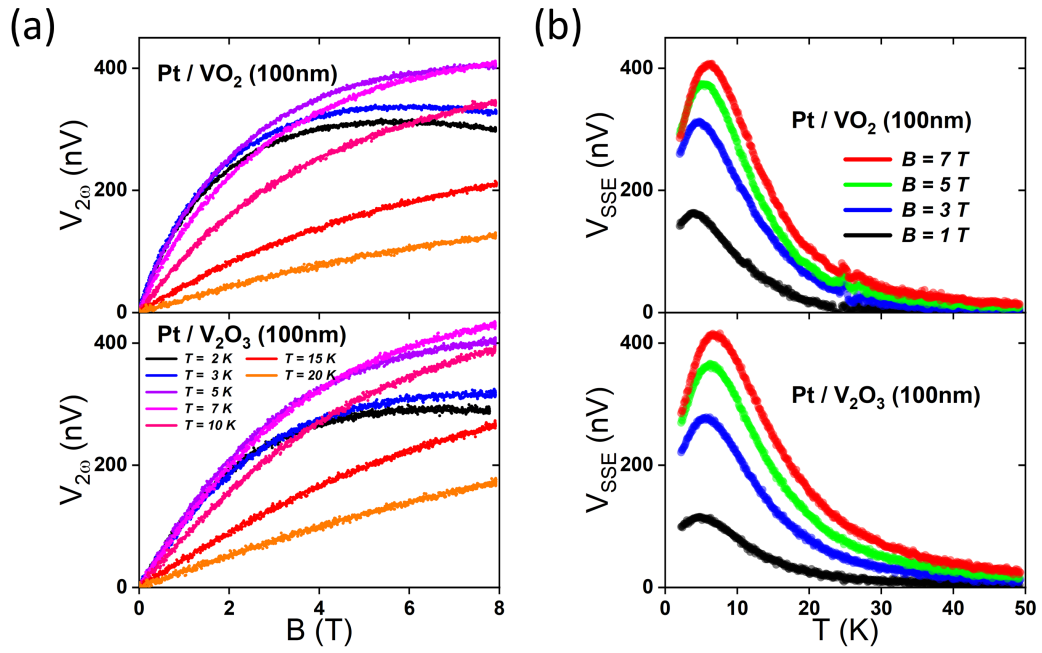

Figure 5.9 : (a) The field dependence of the second harmonic voltage at various temperatures in Pt/VO_2 and Pt/ceV2O3 device with the same 100 nm thickness. (b)The temperature dependence of the SSE voltage at various fields in Pt/VO_2 and Pt/ceV2O3 device with the same 100 nm thickness.

the spin current into the Pt. We also notice that the SSE in Cr_2O_3 when the field is along the hard axis is interpreted as paramagnetic in nature from weakly interacting spins near the Cr_2O_3 surface. Thus, it is important to consider whether the SSE signal in V_2O_3 can be understood as the paramagnetic SSE.

In a paramagnetic insulator (PI), the interfacial spin current, and thus SSE voltage, is expected to be roughly proportional to the magnetization of the PI described by a Brillouin function $B_S(x)$ of the spin S, where $x = g\mu B/k_BT$ [68, 102]. To check this, we examine whether the field dependence of the voltage can be fit with a Brillouin function. Under this assumption, the SSE voltage can be written as:

$$V(B,T) = C(T)\, B_S\left(\frac{g\mu_B B}{k_B(T-\Theta_{CW})}\right), \tag{5.1}$$

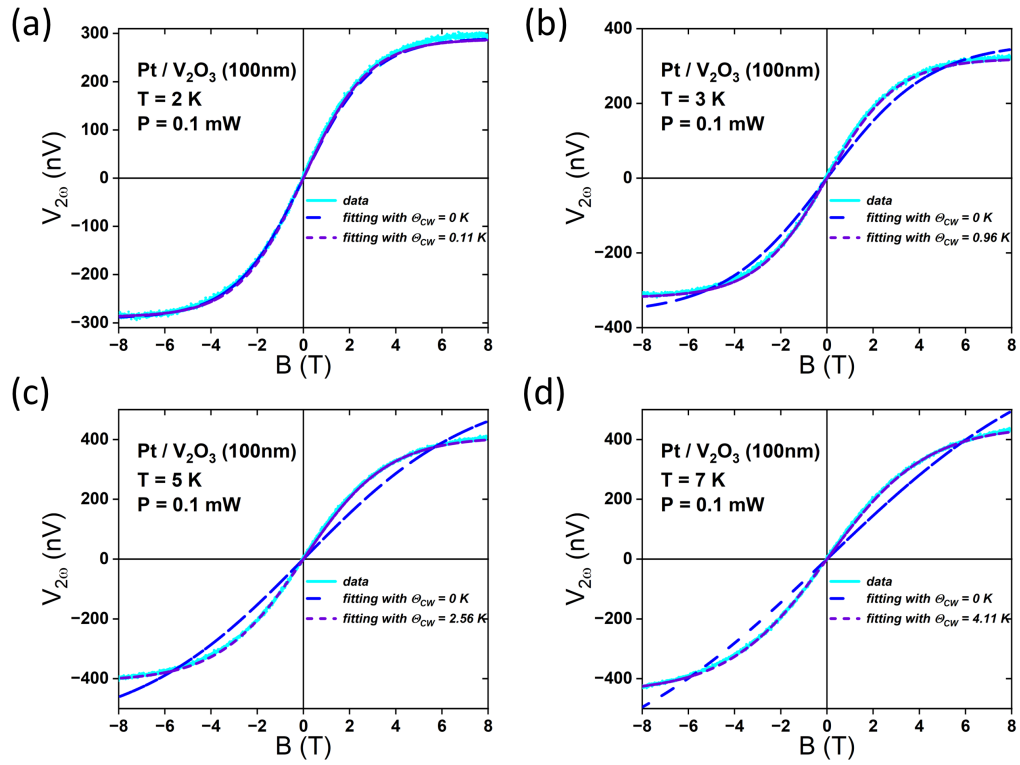

Figure 5.10 : Comparison of the measured second harmonic voltage and fitting with eq. 5.1 with and without the parameter Θ_{CW} at (a) 2 K, (b) 3 K, (c) 5 K and (d) 7 K. The blue line is the data points, the cyan dash line is the fitting without Θ_{CW}, and the purple double dash line is the fitting with Θ_{CW}.

$$B_S(x) = \frac{2S+1}{2S}\coth\left(\frac{2S+1}{2}x\right) - \frac{1}{2S}\coth\left(\frac{x}{2}\right), \tag{5.2}$$

where $C(T)$ is temperature-dependent magnitude including thermal conductivity, and Θ_{CW} is a possible Curie-Weiss temperature. Fig. 5.10 shows the fitting results with and without Θ_{CW}. The fitting excluding Θ_{CW} fails to capture the shape of the data accurately, whereas incorporating Θ_{CW} gives good fits at each temperature. However, the extracted Θ_{CW} exhibits a strong temperature dependence, becoming increasingly positive as temperature rises, indicating stronger ferromagnetic interactions. In V_2O_3, we expect the interactions between the neighboring V ions to be antiferromagnetic.

Thus, between this analysis and the observed systematic thickness dependence in V_2O_3, we conclude that the LSSE in V_2O_3 is not paramagnetic SSE.

5.5 Conclusion

We observe a temperature-dependent longitudinal spin Seebeck response in V_2O_3 thin films within the low-temperature antiferromagnetic phase. The behavior of the measured LSSE voltage shares a significant feature with the paramagnetic LSSE response observed in VO_2. However, the magnitude of LSSE signal decreases consistently with increasing thickness, which seemingly rules out a dominant interfacial contribution to the SSE. This negative correlation between the SSE magnitude and the thickness suggests that the magnon energy relaxation length is shorter than 50 nm in V_2O_3, consistent with strong spin-lattice coupling in V_2O_3. Additional studies of magnon modes in V_2O_3 are required to resolve the nature of spin transport in this correlated system.

Chapter 6

Open Questions and Outlook

In the preceding chapters, we demonstrated the presence of spin Seebeck effect both in the low temperature paramagnetic insulating phase of VO_2 and in the low temperature antiferromagnetic insulating phase of V_2O_3, highlighted their striking similarity, and explored potential mechanisms underlying these observations. In this concluding chapter, we will discuss some pertinent open questions in the field of spin Seebeck research. We also provide an outlook on future experimental investigations.

6.1 Open questions

To quantify the spin Seebeck coefficient across different materials and elucidate its underlying mechanism, obtaining an accurate temperature profile is paramount. Unfortunately, even with state-of-the-art techniques, this remains elusive. Because the spin Seebeck effect requires a heater to generate a spin current, the system resides in a nonequilibrium steady state. Here the temperature profile involves the phonon temperature in the spin-orbit metal (SOM), the electron temperature in the SOM, the phonon temperature in the magnetic insulator (MI) and the spin (magnon) temperature in the MI. Conventional thermometers can only probe the local phonon temperature at its point of contact. The electron temperature and spin temperature are usually inferred via simulations. Generally, we need to take care of which temperature the thermometers give. In the traditional LSSE setup for the bulk ma-

terials, the thermometers are placed on the sapphire plates which sandwich the MI crystal [24]. These thermometers actually measure the local temperature of the heat bath, not the MI. To circumvent this, the method of using the SOM layer itself as an in-situ thermometer comes up [28]. This excludes thermal artifacts in the LSSE measurements and shows the concomitant enhancement of spin Seebeck coefficient and thermal conductivity in the YIG slab at low temperatures. However, even this method yields only the average electron temperature in the SOM layer, and, due to the Kapitza thermal boundary resistance which grows approximately as T^{-3} as the temperature decreases, this method is not valid at low temperatures for indicating the MI temperature. The Johnson-Nyquist thermal noise measurements can be used to assess the electron temperature of the SOM at low temperatures [129]. Still, it doesn't help with the phonon or spin temperature in the MI.

Simulations likewise face challenges. When the thickness of the MI layer approaches its thermal diffusion length, the heat diffusion equations no longer apply, and numerical solutions of the Boltzmann Transport Equation via Monte Carlo method [146] are required. Besides, key parameters, such as the low temperature thermal conductivity of the MI thin film and the thermal boundary resistance between the MI and the SOM, are notoriously difficult to measure. If we extend the model to consider the electron temperature and spin temperature, additional unknowns emerge: we need to know the electron-phonon coupling strength in the SOM and spin-phonon (magnon-phonon) coupling strength in the MI. Together, these measurement and modeling obstacles currently limit our ability to map the full temperature landscape that governs the spin Seebeck effect.

The electric detection of SSE also faces several inherent drawbacks. It depends on the ISHE of the injected spin current in the SOM and the interfacial spin conductance

between the MI and the SOM. The SSE signal depends on the resistivity, spin Hall angle, spin diffusion length, and thickness of the SOM, all of which make the comparison among different MI complicated. Most critically, the interfacial spin conductance is highly variable. It can differ by 2 orders of magnitude depending on the surface cleaning methods and preparation [147–149]. It can even change the field dependence of the LSSE signal in systems like Pt/YIG [150], Pt/Cr_2O_3 [50]. To overcome these issues, one may use optical methods, such as time-resolved magneto-optical Kerr effect (TR-MOKE) [151]. TR-MOKE can directly detect the spin accumulation at the surface along the normal direction of SOM, which may avoid the annoying interfacial problems. Or one can use nitrogen-vacancy (NV) magnetometry to measure the local magnetic field fluctuations generated by thermally excited magnons [152].

6.2 Outlook

Thanks to complicated magnetic states in the world, the spin Seebeck effect has numerous opportunities for further exploration.

6.2.1 Multiferroics

$BiFeO_3$ (BFO) is a room-temperature multiferroic with a large ferroelectric polarization ($\sim 90\ \mu C/cm^2$), G-type antiferromagnetic ordering, and a weak ferromagnetic moment arising from the Dzyaloshinskii-Moriya interaction [153, 154]. A nonlocal geometry demonstrated the nonvolatile, hysteretic, electric-field control of thermally excited magnon current in the absence of an applied magnetic field in BFO thin film at room temperature [91]. By alternating positive and negative polarity electric field pulses, two distinct nonvolatile states appear in the measured nonlocal SSE voltage. This has been suggested as a basis for low-power logic-in-memory comput-

ing device [155]. A symmetry-based phenomenological model [156] was presented to explain the magnon transport in the BFO with complicated magnetic texture. However, the temperature dependence of nonlocal SSE in BFO remains under explored. The pilot experiment suggests that, as temperature goes down, the difference between the two nonvolatile voltages decreases and vanishes at ~ 250 K. Yet, the poor signal-to-noise ratio and limited reproducibility currently hinder deeper analysis. To advance understanding, more comprehensive temperature-dependent measurements with improved experimental repeatability and sensitivity are required.

6.2.2 Spin Ices

$Dy_2Ti_2O_7$ (DTO) is an example of classical spin ice [157, 158], where Dy^{3+} ions ($J = 15/2$) form a pyrochlore lattice comprising corner-sharing tetrahedra, with the centers of the tetrahedra forming a diamond lattice (Fig. 6.1a). The strong crystallographic anisotropy on the order of 300 K locks the moment of Dy^{3+} ions along its local <111> axis, forcing it to point either radially towards or away from the center of its tetrahedron (Fig. 6.1b). Meanwhile, the nearest-neighbor dipole-dipole interactions on the order of 2 K cause the ground states that favor 6 energetically degenerate "2-in/2-out" configurations for each tetrahedron [159], analogous to the "2-in/2-out" arrangement of hydrogen in Pauling's model of ice water [160]. That's why it's named (classical) spin ice. The lowest excitations arise when a single spin flip disrupts the ice rule, creating adjacent "1-in/3-out" and "3-in/1-out" tetrahedra. They are thought as effective magnetic monopoles (or monopole-antimonopole pairs) [161, 162] and are connected via a "Dirac string" of flipped moments [163]. The monopole excitations interact via a Coulomb-like interaction [157,161] with Debye-Hückel-like screening [164], and at temperatures around 5 to 10 K, DTO supports a monopole plasma that under-

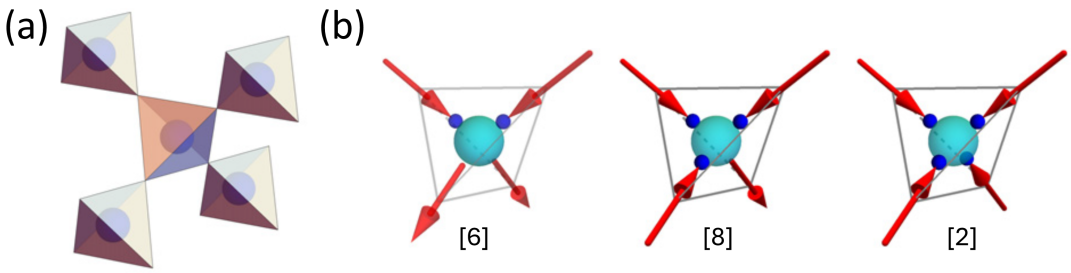

Figure 6.1 : (a) A fragment of the cubic pyrochlore lattice of corner linked tetrahedra occupied by the magnetic ions in spin ice. There is an oxide ion at the centre of every tetrahedron (spheres). (b) The spin ice mapping, where spins in $Dy_2Ti_2O_7$ become analogous to proton displacement vectors in water ice. Left to right, respectively: single tetrahedra showing the water ice configurations H_2O, H_3O^+ and $H_4O_2^+$, with analogous spin ice configurations (red arrows indicate ionic magnetic moments, large circle the oxide ion O^{2-}, small circles the proton H^+). Numbers in square brackets: per tetrahedron, there are 6 possible '2-in/2-out" states, 8 possible "3-in/1-out" or "3-out/1-in" states, and 2 possible "all in" or "all out" states. Taken from [158].

goes generation/recombination of monopole/antimonopole pairs [165]. Experimental evidence for these monopole excitations has been observed through neutron scattering [166], muon spin rotation [167], and magnetic susceptibility [168]. However, to date, there has been no published investigation of driven spin transport in a classical spin ice. This presents a unique opportunity to explore angular momentum transport in a magnetic insulator where the spin-carrying emergent excitations differ fundamentally from conventional magnons. The pilot experiments cannot distinguish the spin Seebeck signal in DTO from the normal Nernst voltage down to 3 K. To advance understanding, measurements performed in dilution temperature are required.

6.2.3 Altermagnetism

Altermagnetism [169, 170] is a newly recognized magnetic phase based on spin-symmetry principles, in which strong time-reversal symmetry-breaking responses and

spin-polarization phenomena, typical of ferromagnets, are accompanied by antiparallel magnetic moment alignment with vanishing net magnetization, typical of antiferromagnets. The degeneracy of magnon bands with opposite chirality is predicted to be lifted in altermagnets, with the sign of the splitting alternating across the magnon Brillouin zone. These altermagnetic magnons can be chiral and carry spin currents, similar to ferromagnets but with highly anisotropic characteristics; around the degenerate Γ point, their dispersion can be linear reminiscent of antiferromagnets. Their unique magnon band structure may open intriguing new directions in research and application of spintronics and spin caloritronics. MnF_2 and Fe_2O_3 are promising candidates and revisiting SSE measurements in these materials may shed new light on the mechanism underneath.

6.2.4 Orbitronics

Recently, the notion of spin current has been extended to the idea of "orbital current", a flow of orbital angular momentum (OAM) [171, 172]. Some theories [173] and experiments have uncovered that electrons may acquire nonvanishing OAM when an external electric field is applied, even without the spin–orbit coupling. These findings have spurred the emergence of a burgeoning field known as orbitronics, which harnesses the orbit degree of freedom to manipulate magnetic devices. How orbital current can contribute to SSE is an unexplored area of research.

Bibliography

[1] I. Žutić, J. Fabian, and S. D. Sarma, "Spintronics: Fundamentals and applications," *Reviews of modern physics*, vol. 76, no. 2, p. 323, 2004.

[2] A. Hoffmann and S. D. Bader, "Opportunities at the frontiers of spintronics," *Physical Review Applied*, vol. 4, no. 4, p. 047001, 2015.

[3] A. Hirohata, K. Yamada, Y. Nakatani, I.-L. Prejbeanu, B. Diény, P. Pirro, and B. Hillebrands, "Review on spintronics: Principles and device applications," *Journal of Magnetism and Magnetic Materials*, vol. 509, p. 166711, 2020.

[4] G. S. Nolas, J. Sharp, and J. Goldsmid, *Thermoelectrics: basic principles and new materials developments*, vol. 45. Springer Science & Business Media, 2013.

[5] G. E. Bauer, E. Saitoh, and B. J. Van Wees, "Spin caloritronics," *Nature materials*, vol. 11, no. 5, pp. 391–399, 2012.

[6] K.-I. Uchida, "Transport phenomena in spin caloritronics," *Proceedings of the Japan Academy, Series B*, vol. 97, no. 2, pp. 69–88, 2021.

[7] S. Maekawa, S. O. Valenzuela, and E. Saitoh, *Spin current*. Oxford University Press, 2017.

[8] V. Kruglyak, S. Demokritov, and D. Grundler, "Magnonics," *Journal of Physics D: Applied Physics*, vol. 43, no. 26, p. 264001, 2010.

[9] S. M. Rezende, A. Azevedo, and R. L. Rodríguez-Suárez, "Introduction to antiferromagnetic magnons," *Journal of Applied Physics*, vol. 126, no. 15, 2019.

[10] R. M. White, *Quantum theory of magnetism: magnetic properties of materials*. Springer, 2007.

[11] J. Robinson, J. Witt, and M. Blamire, "Controlled injection of spin-triplet supercurrents into a strong ferromagnet," *Science*, vol. 329, no. 5987, pp. 59–61, 2010.

[12] C.-Z. Chen, Q.-f. Sun, F. Wang, and X. Xie, "Detection of spinons via spin transport," *Physical Review B—Condensed Matter and Materials Physics*, vol. 88, no. 4, p. 041405, 2013.

[13] J. Romhányi, K. Penc, and R. Ganesh, "Hall effect of triplons in a dimerized quantum magnet," *Nature communications*, vol. 6, no. 1, p. 6805, 2015.

[14] T. Funato, M. Matsuo, and T. Kato, "Chirality-induced phonon-spin conversion at an interface," *Physical Review Letters*, vol. 132, no. 23, p. 236201, 2024.

[15] A. Hoffmann, "Spin Hall effects in metals," *IEEE transactions on magnetics*, vol. 49, no. 10, pp. 5172–5193, 2013.

[16] J. Sinova, S. O. Valenzuela, J. Wunderlich, C. Back, and T. Jungwirth, "Spin Hall effects," *Reviews of modern physics*, vol. 87, no. 4, pp. 1213–1260, 2015.

[17] K. Ando, S. Takahashi, J. Ieda, Y. Kajiwara, H. Nakayama, T. Yoshino, K. Harii, Y. Fujikawa, M. Matsuo, S. Maekawa, and E. Saitoh, "Inverse spin-Hall effect induced by spin pumping in metallic system," *Journal of applied physics*, vol. 109, no. 10, 2011.

[18] K. Uchida, M. Ishida, T. Kikkawa, A. Kirihara, T. Murakami, and E. Saitoh, "Longitudinal spin Seebeck effect: from fundamentals to applications," *Journal of Physics: Condensed Matter*, vol. 26, no. 34, p. 343202, 2014.

[19] K.-I. Uchida, H. Adachi, T. Kikkawa, A. Kirihara, M. Ishida, S. Yorozu, S. Maekawa, and E. Saitoh, "Thermoelectric generation based on spin Seebeck effects," *Proceedings of the IEEE*, vol. 104, no. 10, pp. 1946–1973, 2016.

[20] T. Kikkawa and E. Saitoh, "Spin Seebeck effect: Sensitive probe for elementary excitation, spin correlation, transport, magnetic order, and domains in solids," *Annual Review of Condensed Matter Physics*, vol. 14, no. 1, pp. 129–151, 2023.

[21] K.-I. Uchida, S. Takahashi, K. Harii, J. Ieda, W. Koshibae, K. Ando, S. Maekawa, and E. Saitoh, "Observation of the spin Seebeck effect," *Nature*, vol. 455, no. 7214, pp. 778–781, 2008.

[22] K.-I. Uchida, H. Adachi, T. Ota, H. Nakayama, S. Maekawa, and E. Saitoh, "Observation of longitudinal spin-Seebeck effect in magnetic insulators," *Applied Physics Letters*, vol. 97, no. 17, 2010.

[23] S. M. Wu, F. Y. Fradin, J. Hoffman, A. Hoffmann, and A. Bhattacharya, "Spin Seebeck devices using local on-chip heating," *Journal of Applied Physics*, vol. 117, no. 17, 2015.

[24] K.-I. Uchida, T. Kikkawa, A. Miura, J. Shiomi, and E. Saitoh, "Quantitative temperature dependence of longitudinal spin Seebeck effect at high temperatures," *Physical Review X*, vol. 4, no. 4, p. 041023, 2014.

[25] T. Kikkawa, K.-I. Uchida, S. Daimon, Z. Qiu, Y. Shiomi, and E. Saitoh, "Critical suppression of spin Seebeck effect by magnetic fields," *Physical Review B*,

vol. 92, no. 6, p. 064413, 2015.

[26] H. Jin, S. R. Boona, Z. Yang, R. C. Myers, and J. P. Heremans, "Effect of the magnon dispersion on the longitudinal spin Seebeck effect in yttrium iron garnets," *Physical Review B*, vol. 92, no. 5, p. 054436, 2015.

[27] E.-J. Guo, J. Cramer, A. Kehlberger, C. A. Ferguson, D. A. MacLaren, G. Jakob, and M. Kläui, "Influence of thickness and interface on the low-temperature enhancement of the spin Seebeck effect in YIG films," *Physical Review X*, vol. 6, no. 3, p. 031012, 2016.

[28] R. Iguchi, K.-I. Uchida, S. Daimon, and E. Saitoh, "Concomitant enhancement of the longitudinal spin Seebeck effect and the thermal conductivity in a Pt/YIG/Pt system at low temperatures," *Physical Review B*, vol. 95, no. 17, p. 174401, 2017.

[29] A. Prakash, B. Flebus, J. Brangham, F. Yang, Y. Tserkovnyak, and J. P. Heremans, "Evidence for the role of the magnon energy relaxation length in the spin Seebeck effect," *Physical Review B*, vol. 97, no. 2, p. 020408, 2018.

[30] T. Kikkawa, K. Shen, B. Flebus, R. A. Duine, K.-I. Uchida, Z. Qiu, G. E. Bauer, and E. Saitoh, "Magnon polarons in the spin Seebeck effect," *Physical review letters*, vol. 117, no. 20, p. 207203, 2016.

[31] Z. Shi, Q. Xi, J. Li, Y. Li, M. Aldosary, Y. Xu, J. Zhou, S.-M. Zhou, and J. Shi, "Role of magnon-magnon scattering in magnon polaron spin Seebeck effect," *Physical Review Letters*, vol. 127, no. 27, p. 277203, 2021.

[32] A. Kehlberger, U. Ritzmann, D. Hinzke, E.-J. Guo, J. Cramer, G. Jakob, M. C. Onbasli, D. H. Kim, C. A. Ross, M. B. Jungfleisch, B. Hillebrands, U. Nowak,

and M. Kläui, "Length scale of the spin Seebeck effect," *Physical review letters*, vol. 115, no. 9, p. 096602, 2015.

[33] T. Kikkawa, K. Uchida, Y. Shiomi, Z. Qiu, D. Hou, D. Tian, H. Nakayama, X.-F. Jin, and E. Saitoh, "Longitudinal spin Seebeck effect free from the proximity nernst effect," *Physical review letters*, vol. 110, no. 6, p. 067207, 2013.

[34] T. Kikkawa, K. Uchida, S. Daimon, Y. Shiomi, H. Adachi, Z. Qiu, D. Hou, X.-F. Jin, S. Maekawa, and E. Saitoh, "Separation of longitudinal spin Seebeck effect from anomalous Nernst effect: Determination of origin of transverse thermoelectric voltage in metal/insulator junctions," *Physical Review B—Condensed Matter and Materials Physics*, vol. 88, no. 21, p. 214403, 2013.

[35] D. Qu, S. Huang, J. Hu, R. Wu, and C. Chien, "Intrinsic spin Seebeck effect in Au/YIG," *Physical review letters*, vol. 110, no. 6, p. 067206, 2013.

[36] N. Vlietstra, J. Shan, B. J. Van Wees, M. Isasa, F. Casanova, and J. Ben Youssef, "Simultaneous detection of the spin-Hall magnetoresistance and the spin-Seebeck effect in platinum and tantalum on yttrium iron garnet," *Physical Review B*, vol. 90, no. 17, p. 174436, 2014.

[37] B. Miao, S. Huang, D. Qu, and C. Chien, "Absence of anomalous Nernst effect in spin Seebeck effect of Pt/YIG," *AIP Advances*, vol. 6, no. 1, 2016.

[38] A. Sola, P. Bougiatioti, M. Kuepferling, D. Meier, G. Reiss, M. Pasquale, T. Kuschel, and V. Basso, "Longitudinal spin Seebeck coefficient: heat flux vs. temperature difference method," *Scientific reports*, vol. 7, no. 1, p. 46752, 2017.

[39] P. Jiménez-Cavero, I. Lucas, D. Bugallo, C. López-Bueno, R. Ramos, P. A. Algarabel, M. R. Ibarra, F. Rivadulla, and L. Morellón, "Quantification of the interfacial and bulk contributions to the longitudinal spin Seebeck effect," *Applied Physics Letters*, vol. 118, no. 9, 2021.

[40] W. Xing, Y. Ma, Y. Yao, R. Cai, Y. Ji, R. Xiong, K. Shen, and W. Han, "Facet-dependent magnon-polarons in epitaxial ferrimagnetic Fe_3O_4 thin films," *Physical Review B*, vol. 102, no. 18, p. 184416, 2020.

[41] A. Aqeel, N. Vlietstra, J. A. Heuver, G. E. Bauer, B. Noheda, B. J. Van Wees, and T. Palstra, "Spin-Hall magnetoresistance and spin Seebeck effect in spin-spiral and paramagnetic phases of multiferroic $CoCr_2O_4$ films," *Physical Review B*, vol. 92, no. 22, p. 224410, 2015.

[42] N. Ito, T. Kikkawa, J. Barker, D. Hirobe, Y. Shiomi, and E. Saitoh, "Spin Seebeck effect in the layered ferromagnetic insulators $CrSiTe_3$ and $CrGeTe_3$," *Physical Review B*, vol. 100, no. 6, p. 060402, 2019.

[43] S. Geprägs, A. Kehlberger, F. D. Coletta, Z. Qiu, E.-J. Guo, T. Schulz, C. Mix, S. Meyer, A. Kamra, M. Althammer, H. Huebl, G. Jakob, Y. Ohnuma, H. Adachi, J. Barker, S. Maekawa, G. E. Bauer, E. Saitoh, R. Gross, S. T. Goennenwein, and M. Kläui, "Origin of the spin Seebeck effect in compensated ferrimagnets," *Nature communications*, vol. 7, no. 1, p. 10452, 2016.

[44] J. Cramer, E.-J. Guo, S. Geprägs, A. Kehlberger, Y. P. Ivanov, K. Ganzhorn, F. Della Coletta, M. Althammer, H. Huebl, R. Gross, J. Kosel, M. Kläui, and S. T. Goennenwein, "Magnon mode selective spin transport in compensated ferrimagnets," *Nano letters*, vol. 17, no. 6, pp. 3334–3340, 2017.

[45] B. Yang, S. Xia, H. Zhao, G. Liu, J. Du, K. Shen, Z. Qiu, and D. Wu, "Revealing thermally driven distortion of magnon dispersion by spin Seebeck effect in $Gd_3Fe_5O_{12}$," *Physical Review B*, vol. 103, no. 5, p. 054411, 2021.

[46] K.-K. Wu, H.-M. Lee, J. Xu, P.-Y. Yang, C. Chien, S.-Y. Huang, and D. Qu, "Magnon spin current from a non-collinear magnetic phase in a compensated rare earth ferrimagnet," *Applied Physics Letters*, vol. 124, no. 10, 2024.

[47] A. Chanda, C. Holzmann, N. Schulz, D. Stein, M. Albrecht, M.-H. Phan, and H. Srikanth, "Thermally generated magnonic spin currents in a polycrystalline gadolinium iron garnet thin film with perpendicular magnetic anisotropy," *Journal of Applied Physics*, vol. 135, no. 12, 2024.

[48] S. Seki, T. Ideue, M. Kubota, Y. Kozuka, R. Takagi, M. Nakamura, Y. Kaneko, M. Kawasaki, and Y. Tokura, "Thermal generation of spin current in an antiferromagnet," *Physical review letters*, vol. 115, no. 26, p. 266601, 2015.

[49] J. Li, H. T. Simensen, D. Reitz, Q. Sun, W. Yuan, C. Li, Y. Tserkovnyak, A. Brataas, and J. Shi, "Observation of magnon polarons in a uniaxial antiferromagnetic insulator," *Physical review letters*, vol. 125, no. 21, p. 217201, 2020.

[50] W. Yuan, J. Li, and J. Shi, "Spin current generation and detection in uniaxial antiferromagnetic insulators," *Applied Physics Letters*, vol. 117, no. 10, 2020.

[51] Y. Luo, C. Liu, H. Saglam, Y. Li, W. Zhang, S. S.-L. Zhang, J. E. Pearson, B. Fisher, T. Zhou, A. Bhattacharya, and A. Hoffmann, "Distinguishing antiferromagnetic spin sublattices via the spin Seebeck effect," *Physical Review B*, vol. 103, no. 2, p. L020401, 2021.

[52] J. Keagy, H. Liu, J. Tang, W. Tan, W. Yuan, S. Mahesh, R. Cheng, and J. Shi, "Disorder-induced suppression of antiferromagnetic magnon transport in Cr_2O_3," *Physical Review Applied*, vol. 24, no. 1, p. L011005, 2025.

[53] C. Liu, Y. Luo, D. Hong, S. S.-L. Zhang, H. Saglam, Y. Li, Y. Lin, B. Fisher, J. E. Pearson, J. S. Jiang, H. Zhou, J. Wen, A. Hoffmann, and A. Bhattacharya, "Electric field control of magnon spin currents in an antiferromagnetic insulator," *Science Advances*, vol. 7, no. 40, p. eabg1669, 2021.

[54] S. M. Wu, W. Zhang, A. Kc, P. Borisov, J. E. Pearson, J. S. Jiang, D. Lederman, A. Hoffmann, and A. Bhattacharya, "Antiferromagnetic spin Seebeck effect," *Physical review letters*, vol. 116, no. 9, p. 097204, 2016.

[55] J. Li, Z. Shi, V. H. Ortiz, M. Aldosary, C. Chen, V. Aji, P. Wei, and J. Shi, "Spin Seebeck effect from antiferromagnetic magnons and critical spin fluctuations in epitaxial FeF_2 films," *Physical review letters*, vol. 122, no. 21, p. 217204, 2019.

[56] Y. Shiomi, R. Takashima, D. Okuyama, G. Gitgeatpong, P. Piyawongwatthana, K. Matan, T. Sato, and E. Saitoh, "Spin Seebeck effect in the polar antiferromagnet α-$Cu_2V_2O_7$," *Physical Review B*, vol. 96, no. 18, p. 180414, 2017.

[57] J. Holanda, D. Maior, O. Alves Santos, L. Vilela-Leão, J. Mendes, A. Azevedo, R. Rodríguez-Suárez, and S. Rezende, "Spin Seebeck effect in the antiferromagnet nickel oxide at room temperature," *Applied Physics Letters*, vol. 111, no. 17, 2017.

[58] P. Ribeiro, F. Machado, M. Gamino, A. Azevedo, and S. Rezende, "Spin Seebeck effect in antiferromagnet nickel oxide in wide ranges of temperature and magnetic field," *Physical Review B*, vol. 99, no. 9, p. 094432, 2019.

[59] I. Gray, T. Moriyama, N. Sivadas, G. M. Stiehl, J. T. Heron, R. Need, B. J. Kirby, D. H. Low, K. C. Nowack, D. G. Schlom, D. C. Ralph, T. Ono, and G. D. Fuchs, "Spin Seebeck imaging of spin-torque switching in antiferromagnetic Pt/NiO heterostructures," *Physical Review X*, vol. 9, no. 4, p. 041016, 2019.

[60] D. Hong, C. Liu, J. E. Pearson, A. Hoffmann, D. D. Fong, and A. Bhattacharya, "Spin Seebeck effect in insulating $SrFeO_{3-\delta}$ films," *Applied Physics Letters*, vol. 114, no. 24, 2019.

[61] M. H. Mohammed, J. Horvat, Z. Cheng, S. Cao, E. Li, and R. Li, "Magnetic interaction between Pr^{3+} and Dy^{3+} spins and their spin transition induced by magnetic field in a $Dy_{0.5}Pr_{0.5}FeO_3$ single crystal," *The Journal of Physical Chemistry C*, vol. 123, no. 50, pp. 30584–30593, 2019.

[62] A. Das, V. E. Phanindra, A. Watson, and T. Banerjee, "Coexistence of different magnetic ordering in thin films of $SrMnO_3$ studied by spin transport," *Applied Physics Letters*, vol. 118, no. 5, 2021.

[63] J. Xu, J. He, J.-S. Zhou, D. Qu, S.-Y. Huang, and C. Chien, "Observation of vector spin Seebeck effect in a noncollinear antiferromagnet," *Physical Review Letters*, vol. 129, no. 11, p. 117202, 2022.

[64] J. Xu, W. Lin, J. He, J.-S. Zhou, D. Qu, S.-Y. Huang, and C. Chien, "Vector spin Seebeck effect and spin swapping effect in antiferromagnetic insulators with non-collinear spin structure," *APL Materials*, vol. 11, no. 9, 2023.

[65] J. de Lima, P. Ribeiro, F. Machado, and S. Rezende, "Enhanced spin Seebeck effect in the paramagnetic phase of the three-dimensional heisenberg antiferromagnet $RbMnF_3$," *Physical Review B*, vol. 107, no. 14, p. L140406, 2023.

[66] K. Nakagawa, M. Kanega, T. Yokouchi, M. Sato, and Y. Shiomi, "Spin transport in a Berezinskii-Kosterlitz-Thouless magnet candidate $BaNi_2V_2O_8$," *Physical Review Materials*, vol. 9, no. 1, p. L011401, 2025.

[67] X. He, S. Ding, H. G. Giil, J. Wang, M. Bhukta, M. Wu, W. Shi, Z. Lin, Z. Liang, J. Yang, M. Kläui, A. Brataas, Y. Hou, and R. Wu, "Spin Seebeck in the weakly exchange-coupled van der Waals antiferromagnet across the spin-flip transition," *Nature Communications*, vol. 16, no. 1, p. 3037, 2025.

[68] S. M. Wu, J. E. Pearson, and A. Bhattacharya, "Paramagnetic spin Seebeck effect," *Physical review letters*, vol. 114, no. 18, p. 186602, 2015.

[69] C. Liu, S. M. Wu, J. E. Pearson, J. S. Jiang, N. d'Ambrumenil, and A. Bhattacharya, "Probing short-range magnetic order in a geometrically frustrated magnet by means of the spin Seebeck effect," *Physical Review B*, vol. 98, no. 6, p. 060415, 2018.

[70] D. Hirobe, M. Sato, T. Kawamata, Y. Shiomi, K.-I. Uchida, R. Iguchi, Y. Koike, S. Maekawa, and E. Saitoh, "One-dimensional spinon spin currents," *Nature Physics*, vol. 13, no. 1, pp. 30–34, 2017.

[71] D. Hirobe, T. Kawamata, K. Oyanagi, Y. Koike, and E. Saitoh, "Generation of spin currents from one-dimensional quantum spin liquid," *Journal of Applied Physics*, vol. 123, no. 12, 2018.

[72] Y. Chen, M. Sato, Y. Tang, Y. Shiomi, K. Oyanagi, T. Masuda, Y. Nambu, M. Fujita, and E. Saitoh, "Triplon current generation in solids," *Nature communications*, vol. 12, no. 1, p. 5199, 2021.

[73] W. Xing, R. Cai, K. Moriyama, K. Nara, Y. Yao, W. Qiao, K. Yoshimura, and W. Han, "Spin Seebeck effect in quantum magnet $Pb_2V_3O_9$," *Applied Physics Letters*, vol. 120, no. 4, 2022.

[74] L. Cornelissen, J. Liu, R. Duine, J. B. Youssef, and B. Van Wees, "Long-distance transport of magnon spin information in a magnetic insulator at room temperature," *Nature Physics*, vol. 11, no. 12, pp. 1022–1026, 2015.

[75] J. Shan, L. J. Cornelissen, N. Vlietstra, J. Ben Youssef, T. Kuschel, R. A. Duine, and B. J. Van Wees, "Influence of yttrium iron garnet thickness and heater opacity on the nonlocal transport of electrically and thermally excited magnons," *Physical Review B*, vol. 94, no. 17, p. 174437, 2016.

[76] J. Shan, L. J. Cornelissen, J. Liu, J. B. Youssef, L. Liang, and B. Van Wees, "Criteria for accurate determination of the magnon relaxation length from the nonlocal spin Seebeck effect," *Physical Review B*, vol. 96, no. 18, p. 184427, 2017.

[77] L. J. Cornelissen, J. Shan, and B. Van Wees, "Temperature dependence of the magnon spin diffusion length and magnon spin conductivity in the magnetic insulator yttrium iron garnet," *Physical Review B*, vol. 94, no. 18, p. 180402, 2016.

[78] L. Cornelissen and B. Van Wees, "Magnetic field dependence of the magnon spin diffusion length in the magnetic insulator yttrium iron garnet," *Physical Review B*, vol. 93, no. 2, p. 020403, 2016.

[79] K. Oyanagi, T. Kikkawa, and E. Saitoh, "Magnetic field dependence of the nonlocal spin Seebeck effect in Pt/YIG/Pt systems at low temperatures," *AIP*

Advances, vol. 10, no. 1, 2020.

[80] J. Shan, P. Bougiatioti, L. Liang, G. Reiss, T. Kuschel, and B. Van Wees, "Nonlocal magnon spin transport in $NiFe_2O_4$ thin films," *Applied Physics Letters*, vol. 110, no. 13, 2017.

[81] J. Shan, A. Singh, L. Liang, L. Cornelissen, Z. Galazka, A. Gupta, B. Van Wees, and T. Kuschel, "Enhanced magnon spin transport in $NiFe_2O_4$ thin films on a lattice-matched substrate," *Applied Physics Letters*, vol. 113, no. 16, 2018.

[82] C. O. Avci, E. Rosenberg, M. Huang, J. Bauer, C. A. Ross, and G. S. Beach, "Nonlocal detection of out-of-plane magnetization in a magnetic insulator by thermal spin drag," *Physical review letters*, vol. 124, no. 2, p. 027701, 2020.

[83] W. Yuan, Q. Zhu, T. Su, Y. Yao, W. Xing, Y. Chen, Y. Ma, X. Lin, J. Shi, R. Shindou, X. Xie, and W. Han, "Experimental signatures of spin superfluid ground state in canted antiferromagnet Cr_2O_3 via nonlocal spin transport," *Science advances*, vol. 4, no. 4, p. eaat1098, 2018.

[84] P. Muduli, R. Schlitz, T. Kosub, R. Hübner, A. Erbe, D. Makarov, and S. T. Goennenwein, "Local and nonlocal spin Seebeck effect in lateral Pt-Cr_2O_3-Pt devices at low temperatures," *APL Materials*, vol. 9, no. 2, 2021.

[85] R. Lebrun, A. Ross, S. Bender, A. Qaiumzadeh, L. Baldrati, J. Cramer, A. Brataas, R. Duine, and M. Kläui, "Tunable long-distance spin transport in a crystalline antiferromagnetic iron oxide," *Nature*, vol. 561, no. 7722, pp. 222–225, 2018.

[86] A. Ross, R. Lebrun, M. Evers, A. Deák, L. Szunyogh, U. Nowak, and M. Kläui,

"Exceptional sign changes of the nonlocal spin Seebeck effect in antiferromagnetic hematite," *Physical Review B*, vol. 103, no. 22, p. 224433, 2021.

[87] G. R. Hoogeboom and B. J. Van Wees, "Nonlocal spin seebeck effect in the bulk easy-plane antiferromagnet NiO," *Physical Review B*, vol. 102, no. 21, p. 214415, 2020.

[88] W. Xing, L. Qiu, X. Wang, Y. Yao, Y. Ma, R. Cai, S. Jia, X. Xie, and W. Han, "Magnon transport in quasi-two-dimensional van der Waals antiferromagnets," *Physical Review X*, vol. 9, no. 1, p. 011026, 2019.

[89] F. Feringa, J. Vink, and B. Van Wees, "Spin-flop transition in the quasi-two-dimensional antiferromagnet $MnPS_3$ detected via thermally generated magnon transport," *Physical Review B*, vol. 106, no. 22, p. 224409, 2022.

[90] T. Liu, J. Peiro, D. K. de Wal, J. C. Leutenantsmeyer, M. H. Guimarães, and B. J. Van Wees, "Spin caloritronics in a $CrBr_3$-based magnetic van der Waals heterostructure," *Physical Review B*, vol. 101, no. 20, p. 205407, 2020.

[91] E. Parsonnet, L. Caretta, V. Nagarajan, H. Zhang, H. Taghinejad, P. Behera, X. Huang, P. Kavle, A. Fernandez, D. Nikonov, H. Li, I. Young, J. Analytis, and R. Ramesh, "Nonvolatile electric field control of thermal magnons in the absence of an applied magnetic field," *Physical review letters*, vol. 129, no. 8, p. 087601, 2022.

[92] A. Kirihara, K.-I. Uchida, Y. Kajiwara, M. Ishida, Y. Nakamura, T. Manako, E. Saitoh, and S. Yorozu, "Spin-current-driven thermoelectric coating," *Nature materials*, vol. 11, no. 8, pp. 686–689, 2012.

[93] S. Manipatruni, D. E. Nikonov, C.-C. Lin, T. A. Gosavi, H. Liu, B. Prasad, Y.-L. Huang, E. Bonturim, R. Ramesh, and I. A. Young, "Scalable energy-efficient magnetoelectric spin–orbit logic," *Nature*, vol. 565, no. 7737, pp. 35–42, 2019.

[94] J. Xiao, G. E. Bauer, K.-c. Uchida, E. Saitoh, and S. Maekawa, "Theory of magnon-driven spin Seebeck effect," *Physical Review B—Condensed Matter and Materials Physics*, vol. 81, no. 21, p. 214418, 2010.

[95] S. Rezende, R. Rodríguez-Suárez, R. Cunha, A. Rodrigues, F. Machado, G. Fonseca Guerra, J. Lopez Ortiz, and A. Azevedo, "Magnon spin-current theory for the longitudinal spin-Seebeck effect," *Physical Review B*, vol. 89, no. 1, p. 014416, 2014.

[96] R. L. Rodríguez-Suárez and S. M. Rezende, "Dominance of the phonon drag mechanism in the spin Seebeck effect at low temperatures," *Physical Review B*, vol. 108, no. 13, p. 134407, 2023.

[97] S. Rezende, R. Rodríguez-Suárez, and A. Azevedo, "Theory of the spin Seebeck effect in antiferromagnets," *Physical Review B*, vol. 93, no. 1, p. 014425, 2016.

[98] S. M. Rezende, A. Azevedo, and R. L. Rodríguez-Suárez, "Magnon diffusion theory for the spin Seebeck effect in ferromagnetic and antiferromagnetic insulators," *Journal of Physics D: Applied Physics*, vol. 51, no. 17, p. 174004, 2018.

[99] D. Reitz, J. Li, W. Yuan, J. Shi, and Y. Tserkovnyak, "Spin Seebeck effect near the antiferromagnetic spin-flop transition," *Physical Review B*, vol. 102, no. 2, p. 020408, 2020.

[100] Y. Yamamoto, M. Ichioka, and H. Adachi, "Spin Seebeck effect in paramagnets and antiferromagnets at elevated temperatures," *Physical Review B*, vol. 100, no. 6, p. 064419, 2019.

[101] Y. Yamamoto, M. Ichioka, and H. Adachi, "Antiferromagnetic spin Seebeck effect across the spin-flop transition: A stochastic Ginzburg-Landau simulation," *Physical Review B*, vol. 105, no. 10, p. 104417, 2022.

[102] K. Oyanagi, S. Takahashi, T. Kikkawa, and E. Saitoh, "Mechanism of paramagnetic spin Seebeck effect," *Physical Review B*, vol. 107, no. 1, p. 014423, 2023.

[103] D. Reitz and Y. Tserkovnyak, "Spin transport from order to disorder," *Physical Review B*, vol. 108, no. 14, p. L140407, 2023.

[104] L. F. Thompson, *An introduction to lithography*. ACS Publications, 1983.

[105] D. Brambley, B. Martin, and P. Prewett, "Microlithography: an overview," *Advanced Materials for Optics and Electronics*, vol. 4, no. 2, pp. 55–74, 1994.

[106] M. Ohring, *Materials science of thin films: depositon and structure*. Academic press, 2002.

[107] M. L. Meade, "Lock-in amplifiers: principles and applications," *IEE Electrical Measurement Series*, 1983.

[108] R. Luo, X. Zhao, L. Chen, T. J. Legvold, H. Navarro, I. K. Schuller, and D. Natelson, "Spin seebeck effect at low temperatures in the nominally paramagnetic insulating state of vanadium dioxide," *Applied Physics Letters*, vol. 121, no. 10, 2022.

[109] Ó. Nájera, M. Civelli, V. Dobrosavljević, and M. J. Rozenberg, "Resolving the VO_2 controversy: Mott mechanism dominates the insulator-to-metal transition," *Physical Review B*, vol. 95, no. 3, p. 035113, 2017.

[110] Ó. Nájera, M. Civelli, V. Dobrosavljević, and M. Rozenberg, "Multiple crossovers and coherent states in a Mott-Peierls insulator," *Physical Review B*, vol. 97, no. 4, p. 045108, 2018.

[111] C. Yin, R. Zhang, G. Qian, Q. Fu, C. Li, M. Wang, C. Zhu, L. Wang, S. Yuan, X. Zhao, and H. Tao, "Unusual magnetic transition near metal-insulator transition and paramagnetic anomaly in VO_2," *Applied Physics Letters*, vol. 110, no. 17, 2017.

[112] R. Zhang, Q. Fu, C. Yin, C. Li, X. Chen, G. Qian, C. Lu, S. Yuan, X. Zhao, and H. Tao, "Understanding of metal-insulator transition in VO_2 based on experimental and theoretical investigations of magnetic features," *Scientific reports*, vol. 8, no. 1, p. 17093, 2018.

[113] D. Meier, D. Reinhardt, M. Van Straaten, C. Klewe, M. Althammer, M. Schreier, S. T. Goennenwein, A. Gupta, M. Schmid, C. H. Back, J.-M. Schmalhorst, T. Kuschel, and R. Günter, "Longitudinal spin Seebeck effect contribution in transverse spin Seebeck effect experiments in Pt/YIG and Pt/NFO," *Nature communications*, vol. 6, no. 1, p. 8211, 2015.

[114] F. Volmer, T. Bisswanger, A. Schmidt, C. Stampfer, and B. Beschoten, "Charge-induced artifacts in nonlocal spin-transport measurements: How to prevent spurious voltage signals," *Physical Review Applied*, vol. 18, no. 1, p. 014028, 2022.

[115] R. Salzer, D. Spemann, P. Esquinazi, R. Höhne, A. Setzer, K. Schindler, H. Schmidt, and T. Butz, "Possible pitfalls in search of magnetic order in thin films deposited on single crystalline sapphire substrates," *Journal of magnetism and magnetic materials*, vol. 317, no. 1-2, pp. 53–60, 2007.

[116] L. J. Cornelissen, K. J. Peters, G. E. Bauer, R. A. Duine, and B. J. Van Wees, "Magnon spin transport driven by the magnon chemical potential in a magnetic insulator," *Physical Review B*, vol. 94, no. 1, p. 014412, 2016.

[117] T. Wimmer, A. Kamra, J. Gückelhorn, M. Opel, S. Geprägs, R. Gross, H. Huebl, and M. Althammer, "Observation of antiferromagnetic magnon pseudospin dynamics and the Hanle effect," *Physical Review Letters*, vol. 125, no. 24, p. 247204, 2020.

[118] P. Mengyan, R. Lichti, B. Baker, and G. Jayarathna, "Magnetic order and muon motion in VO_2," in *Journal of Physics: Conference Series*, vol. 551, p. 012017, IOP Publishing, 2014.

[119] T.-H. Yang, S. Nori, H. Zhou, and J. Narayan, "Defect-mediated room temperature ferromagnetism in vanadium dioxide thin films," *Applied Physics Letters*, vol. 95, no. 10, 2009.

[120] R. Luo, T. J. Legvold, L. Chen, H. Navarro, A. C. Basaran, D. Hong, C. Liu, A. Bhattacharya, I. K. Schuller, and D. Natelson, "Low-temperature spin seebeck effect in nonmagnetic vanadium dioxide," *Physical Review B*, vol. 110, no. 2, p. 024415, 2024.

[121] S. Cheng, M.-H. Lee, R. Tran, Y. Shi, X. Li, H. Navarro, C. Adda, Q. Meng, L.-Q. Chen, R. Dynes, S. Ping Ong, I. K. Schuller, and Y. Zhu, "Inherent

stochasticity during insulator-metal transition in VO_2," *Proceedings of the National Academy of Sciences*, vol. 118, no. 37, p. e2105895118, 2021.

[122] D. Paquet and P. Leroux-Hugon, "Electron correlations and electron-lattice interactions in the metal-insulator, ferroelastic transition in VO_2: A thermodynamical study," *Physical Review B*, vol. 22, no. 11, p. 5284, 1980.

[123] H. Zheng and L. K. Wagner, "Computation of the correlated metal-insulator transition in vanadium dioxide from first principles," *Physical review letters*, vol. 114, no. 17, p. 176401, 2015.

[124] R. Basu, V. Srihari, M. Sardar, S. K. Srivastava, S. Bera, and S. Dhara, "Probing phase transition in VO_2 with the novel observation of low-frequency collective spin excitation," *Scientific reports*, vol. 10, no. 1, p. 1977, 2020.

[125] K. Momma and F. Izumi, "VESTA: a three-dimensional visualization system for electronic and structural analysis," *Applied Crystallography*, vol. 41, no. 3, pp. 653–658, 2008.

[126] M.-H. Lee, Y. Kalcheim, J. d. Valle, and I. K. Schuller, "Controlling metal–insulator transitions in vanadium oxide thin films by modifying oxygen stoichiometry," *ACS Applied Materials & Interfaces*, vol. 13, no. 1, pp. 887–896, 2020.

[127] G. Bergmann, "Weak localization in thin films," *Physica Scripta*, vol. 1986, no. T14, p. 99, 1986.

[128] Y. Niimi, D. Wei, H. Idzuchi, T. Wakamura, T. Kato, and Y. Otani, "Experimental verification of comparability between spin-orbit and spin-diffusion lengths," *Physical review letters*, vol. 110, no. 1, p. 016805, 2013.

[129] R. Luo, T. J. Legvold, L. Chen, and D. Natelson, "Nernst-Ettingshausen effect in thin Pt and W films at low temperatures," *Applied Physics Letters*, vol. 122, no. 18, 2023.

[130] J. H. Park, J. M. Coy, T. S. Kasirga, C. Huang, Z. Fei, S. Hunter, and D. H. Cobden, "Measurement of a solid-state triple point at the metal-insulator transition in VO_2," *Nature*, vol. 500, no. 7463, pp. 431–434, 2013.

[131] L. Cornelissen, K. Oyanagi, T. Kikkawa, Z. Qiu, T. Kuschel, G. Bauer, B. Van Wees, and E. Saitoh, "Nonlocal magnon-polaron transport in yttrium iron garnet," *Physical Review B*, vol. 96, no. 10, p. 104441, 2017.

[132] D. G. Cahill, M. Katiyar, and J. Abelson, "Thermal conductivity of α-si:h thin films," *Physical review B*, vol. 50, no. 9, p. 6077, 1994.

[133] D. G. Cahill, "Thermal-conductivity measurement by time-domain thermoreflectance," *MRS Bulletin*, vol. 43, no. 10, pp. 782–789, 2018.

[134] V. I. Surikov, N. Semenyuk, V. I. Surikov, Y. V. Kuznetsova, and S. Yanchij, "Low-temperature heat capacity vo2$\pm\delta$ and solid solutions v1-xfexo2," in *Journal of Physics: Conference Series*, vol. 1050, p. 012083, IOP Publishing, 2018.

[135] D. Maurer, A. Leue, R. Heichele, and V. Müller, "Elastic behavior near the metal-insulator transition of VO_2," *Physical Review B*, vol. 60, no. 19, p. 13249, 1999.

[136] F. Pobell, *Matter and methods at low temperatures*, vol. 2. Springer, 2007.

[137] D. G. Cahill, S. K. Watson, and R. O. Pohl, "Lower limit to the thermal conductivity of disordered crystals," *Physical Review B*, vol. 46, no. 10, p. 6131,

1992.

[138] R. Moon, "Antiferromagnetism in V_2O_3," *Journal of Applied Physics*, vol. 41, no. 3, pp. 883–883, 1970.

[139] W. Yelon, S. Werner, R. Word, J. Honig, and S. Shivashankar, "Neutron scattering study of the spin waves and magnetic structures in pure and metal-deficient V_2O_3," *Journal of Applied Physics*, vol. 52, no. 3, pp. 2237–2239, 1981.

[140] L. Paolasini, C. Vettier, F. De Bergevin, F. Yakhou, D. Mannix, A. Stunault, W. Neubeck, M. Altarelli, M. Fabrizio, P. Metcalf, and J. Honig, "Orbital occupancy order in V_2O_3: resonant x-ray scattering results," *Physical review letters*, vol. 82, no. 23, p. 4719, 1999.

[141] Y. Kalcheim, N. Butakov, N. M. Vargas, M.-H. Lee, J. Del Valle, J. Trastoy, P. Salev, J. Schuller, and I. K. Schuller, "Robust coupling between structural and electronic transitions in a mott material," *Physical Review Letters*, vol. 122, no. 5, p. 057601, 2019.

[142] B. A. Frandsen, Y. Kalcheim, I. Valmianski, A. S. McLeod, Z. Guguchia, S. C. Cheung, A. M. Hallas, M. N. Wilson, Y. Cai, G. M. Luke, Z. Salman, A. Suter, T. Prokscha, T. Murakami, H. Kageyama, D. Basov, I. K. Schuller, and Y. J. Uemura, "Intertwined magnetic, structural, and electronic transitions in V_2O_3," *Physical Review B*, vol. 100, no. 23, p. 235136, 2019.

[143] M. Erekhinsky, J. De La Venta, and I. K. Schuller, "Spin valve effect across the metal-insulator transition in V_2O_3," *Journal of Applied Physics*, vol. 114, no. 14, 2013.

[144] R. el Hage, T. D. Wang, J. Li, A. C. Basaran, F. Torres, and I. K. Schuller, "Antiferromagnetic V_2O_3 based exchange coupling," *Physical Review Materials*, vol. 8, no. 5, p. 054407, 2024.

[145] K. Masuda and M. Sato, "Microscopic theory of spin Seebeck effect in antiferromagnets," *Journal of the Physical Society of Japan*, vol. 93, no. 3, p. 034702, 2024.

[146] D. Lacroix, K. Joulain, and D. Lemonnier, "Monte Carlo transient phonon transport in silicon and germanium at nanoscales," *Physical Review B—Condensed Matter and Materials Physics*, vol. 72, no. 6, p. 064305, 2005.

[147] M. Jungfleisch, V. Lauer, R. Neb, A. Chumak, and B. Hillebrands, "Improvement of the yttrium iron garnet/platinum interface for spin pumping-based applications," *Applied Physics Letters*, vol. 103, no. 2, 2013.

[148] Z. Qiu, D. Hou, K. Uchida, and E. Saitoh, "Influence of interface condition on spin-Seebeck effects," *Journal of Physics D: Applied Physics*, vol. 48, no. 16, p. 164013, 2015.

[149] S. Pütter, S. Geprägs, R. Schlitz, M. Althammer, A. Erb, R. Gross, and S. T. Goennenwein, "Impact of the interface quality of Pt/YIG (111) hybrids on their spin hall magnetoresistance," *Applied physics letters*, vol. 110, no. 1, 2017.

[150] A. Aqeel, I. J. Vera-Marun, B. J. Van Wees, and T. Palstra, "Surface sensitivity of the spin Seebeck effect," *Journal of Applied Physics*, vol. 116, no. 15, 2014.

[151] J. Kimling, G.-M. Choi, J. T. Brangham, T. Matalla-Wagner, T. Huebner, T. Kuschel, F. Yang, and D. G. Cahill, "Picosecond spin Seebeck effect," *Physical review letters*, vol. 118, no. 5, p. 057201, 2017.

[152] C. Du, T. Van der Sar, T. X. Zhou, P. Upadhyaya, F. Casola, H. Zhang, M. C. Onbasli, C. A. Ross, R. L. Walsworth, Y. Tserkovnyak, and A. Yacoby, "Control and local measurement of the spin chemical potential in a magnetic insulator," *Science*, vol. 357, no. 6347, pp. 195–198, 2017.

[153] C. Ederer and N. A. Spaldin, "Weak ferromagnetism and magnetoelectric coupling in bismuth ferrite," *Physical Review B—Condensed Matter and Materials Physics*, vol. 71, no. 6, p. 060401, 2005.

[154] J. Neaton, C. Ederer, U. Waghmare, N. Spaldin, and K. Rabe, "First-principles study of spontaneous polarization in multiferroic $BiFeO_3$," *Physical Review B—Condensed Matter and Materials Physics*, vol. 71, no. 1, p. 014113, 2005.

[155] R. Ramesh, S. Salahuddin, S. Datta, C. H. Diaz, D. E. Nikonov, I. A. Young, D. Ham, M.-F. Chang, W.-S. Khwa, A. S. Lele, M. Hoffmann, J.-M. Hu, Z. Yao, L. Bellaiche, P. Wu, J. Cai, J. Appenzeller, S. Datta, K. Y. Camsari, J. Kwon, J. A. C. Incorvia, I. Asselberghs, F. Ciubotaru, S. Couet, C. Adelmann, Y. Zheng, A. M. Lindenberg, P. G. Evans, P. Ercius, and I. P. Radu, "Roadmap on low-power electronics," *APL Materials*, vol. 12, no. 9, 2024.

[156] I. A. Harris, S. Husain, P. Meisenheimer, M. Ramesh, H. W. Park, L. Caretta, D. G. Schlom, Z. Yao, L. W. Martin, J. Íñiguez-González, S. K. Kim, and R. Ramesh, "Symmetry-based phenomenological model for magnon transport in a multiferroic," *Physical Review Letters*, vol. 134, no. 1, p. 016703, 2025.

[157] C. Castelnovo, R. Moessner, and S. Sondhi, "Spin ice, fractionalization, and topological order," *Annu. Rev. Condens. Matter Phys.*, vol. 3, no. 1, pp. 35–55, 2012.

[158] S. T. Bramwell and M. J. Harris, "The history of spin ice," *Journal of Physics: Condensed Matter*, vol. 32, no. 37, p. 374010, 2020.

[159] S. Bramwell and M. Harris, "Frustration in ising-type spin models on the pyrochlore lattice," *Journal of Physics: Condensed Matter*, vol. 10, no. 14, p. L215, 1998.

[160] L. Pauling, "The structure and entropy of ice and of other crystals with some randomness of atomic arrangement," *Journal of the American Chemical Society*, vol. 57, no. 12, pp. 2680–2684, 1935.

[161] C. Castelnovo, R. Moessner, and S. L. Sondhi, "Magnetic monopoles in spin ice," *Nature*, vol. 451, no. 7174, pp. 42–45, 2008.

[162] L. D. Jaubert and P. C. Holdsworth, "Signature of magnetic monopole and dirac string dynamics in spin ice," *Nature Physics*, vol. 5, no. 4, pp. 258–261, 2009.

[163] P. Dirac, "Quantised singularities in the electromagnetic field," *Proceedings of the Royal Society of London. Series A, Containing Papers of a Mathematical and Physical Character*, vol. 133, no. 821, pp. 60–72, 1931.

[164] V. Kaiser, J. Bloxsom, L. Bovo, S. T. Bramwell, P. C. Holdsworth, and R. Moessner, "Emergent electrochemistry in spin ice: Debye-Hückel theory and beyond," *Physical Review B*, vol. 98, no. 14, p. 144413, 2018.

[165] R. Dusad, F. K. Kirschner, J. C. Hoke, B. R. Roberts, A. Eyal, F. Flicker, G. M. Luke, S. J. Blundell, and J. S. Davis, "Magnetic monopole noise," *Nature*, vol. 571, no. 7764, pp. 234–239, 2019.

[166] D. Morris, D. Tennant, S. Grigera, B. Klemke, C. Castelnovo, R. Moessner, C. Czternasty, M. Meissner, K. Rule, J.-U. Hoffmann, K. Kiefer, S. Gerischer, D. Slobinsky, and P. RS, "Dirac strings and magnetic monopoles in the spin ice $Dy_2Ti_2O_7$," *Science*, vol. 326, no. 5951, pp. 411–414, 2009.

[167] S. Bramwell, S. Giblin, S. Calder, R. Aldus, D. Prabhakaran, and T. Fennell, "Measurement of the charge and current of magnetic monopoles in spin ice," *Nature*, vol. 461, no. 7266, pp. 956–959, 2009.

[168] L. Bovo, J. Bloxsom, D. Prabhakaran, G. Aeppli, and S. Bramwell, "Brownian motion and quantum dynamics of magnetic monopoles in spin ice," *Nature communications*, vol. 4, no. 1, p. 1535, 2013.

[169] L. Šmejkal, J. Sinova, and T. Jungwirth, "Emerging research landscape of altermagnetism," *Physical Review X*, vol. 12, no. 4, p. 040501, 2022.

[170] L. Bai, W. Feng, S. Liu, L. Šmejkal, Y. Mokrousov, and Y. Yao, "Altermagnetism: Exploring new frontiers in magnetism and spintronics," *Advanced Functional Materials*, vol. 34, no. 49, p. 2409327, 2024.

[171] D. Go, D. Jo, H.-W. Lee, M. Kläui, and Y. Mokrousov, "Orbitronics: Orbital currents in solids," *Europhysics Letters*, vol. 135, no. 3, p. 37001, 2021.

[172] D. Jo, D. Go, G.-M. Choi, and H.-W. Lee, "Spintronics meets orbitronics: Emergence of orbital angular momentum in solids," *npj Spintronics*, vol. 2, no. 1, p. 19, 2024.

[173] D. Go, D. Jo, C. Kim, and H.-W. Lee, "Intrinsic spin and orbital Hall effects from orbital texture," *Physical review letters*, vol. 121, no. 8, p. 086602, 2018.

[174] P. Meisenheimer, M. Ramesh, S. Husain, I. Harris, H. W. Park, S. Zhou, H. Taghinejad, H. Zhang, L. W. Martin, J. Analytis, P. Stevenson, J. Íñiguez-González, S. K. Kim, D. G. Schlom, L. Caretta, Z. Yao, and R. Ramesh, "Designed spin-texture-lattice to control anisotropic magnon transport in antiferromagnets," *Advanced Materials*, vol. 36, no. 36, p. 2404639, 2024.

[175] S. Husain, I. Harris, P. Meisenheimer, S. Mantri, X. Li, M. Ramesh, P. Behera, H. Taghinejad, J. Kim, P. Kavle, S. Zhou, T. Y. Kim, H. Zhang, P. Stevenson, J. G. Analytis, D. Schlom, S. Salahuddin, J. Íñiguez-González, B. Xu, L. W. Martin, L. Caretta, Y. Han, L. Bellaiche, Z. Yao, and R. Ramesh, "Non-volatile magnon transport in a single domain multiferroic," *Nature communications*, vol. 15, no. 1, p. 5966, 2024.

Appendix A

Spin Seebeck measurements in spin ice dysprosium titanate thin film

A.1 Film growth

The $Dy_2Ti_2O_7$ (DTO) film with 15 nm thickness was deposited on (111)-oriented yttria-stabilized ZrO_2 (YSZ) substrate with thickness of 0.5 mm. Due to the lattice match, DTO also favors (111)-orientation, with alternating layers of Kagome and triangular lattices of the cations.

A.2 Longitudinal SSE in dysprosium titanate

The device geometry is similar to those on VO_2 and V_2O_3. Photolithography, magnetron sputtering, and liftoff were used to prepare the Pt wire (600 μm long, 10 μm wide, 10 nm thick) on the DTO film surface. Next, a lithographically defined SiO_x insulating layer with a thickness of 100 nm and an Au heater wire (1000 μm long, 10 μm wide, 50 nm thick) were fabricated on the top of the Pt wire by evaporation and liftoff. During the measurements, an AC current at angular frequency $\omega = 2\pi \times$ (7.7 Hz) is driven through the Au wire, while the voltage across the Pt wire is measured at 2ω using a lock-in amplifier. The measurements are performed as a function of temperature and magnetic field in a Quantum Design Physical Property Measurement System (9T-PPMS) equipped with a rotation stage.

Below we will show results for two identically geometrized devices fabricated on

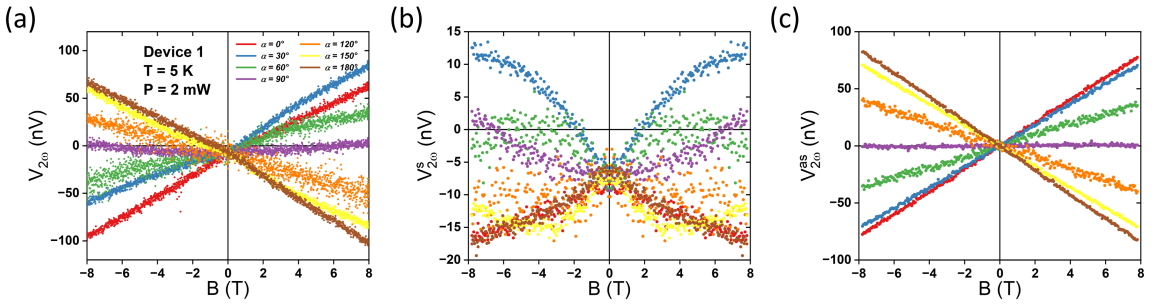

Figure A.1 : (a) The second harmonic voltage as a function of field with different field orientations at 5 K in device 1. The symmetric component (b) and the antisymmetric component (c) as a function of field.

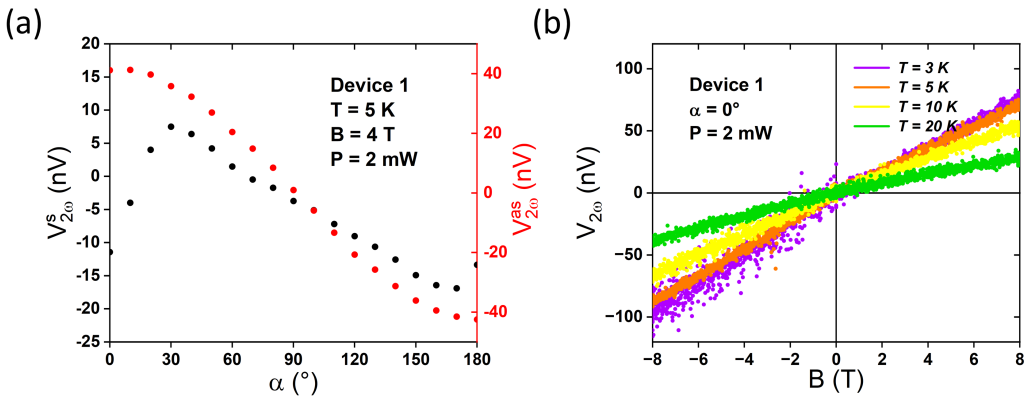

Figure A.2 : (a) Dependence of the symmetric and antisymmetric components of the second harmonic signal in device 1 at 5 K and 4 T with 2 mW heater power on in-plane field orientation α. (b) Field dependence of the second harmonic signal at different temperatures in device 1 with $\alpha = 0°$ and 2 mW heater power.

different $Dy_2Ti_2O_7$ films.

The magnetic field dependence of the second harmonic voltage $V_{2\omega}$ in device 1 for different in-plane field orientations at $T = 5$ K is shown in Fig. A.1a. Clearly, the raw signal is not antisymmetric with the field. We decompose the $V_{2\omega}$ into the symmetric and antisymmetric components: $V^s_{2\omega} = \frac{1}{2}[V_{2\omega}(+H) + V_{2\omega}(-H)]$, and $V^{as}_{2\omega} = \frac{1}{2}[V_{2\omega}(+H) - V_{2\omega}(-H)]$. In devices on FeF_2, the symmetric component $V^s_{2\omega}$ is

explained to be due to the normal magneto-Seebeck signal produced by an incidental in-plane temperature gradient [55]. In devices on SiO_2/Si, $V^s_{2\omega}$ shows a parabolic field response without field orientation dependence [129]. However, in DTO device, $V^s_{2\omega}$ exhibits a complicated magnetic field dependence and a strange orientation dependence (Fig. A.1b), with the maximum magnitude occurring at $\alpha = 30°$, the minimum one at $\alpha = 170°$ (Fig. A.2a), and an approximately linear angular variation in between. The antisymmetric component $V^{as}_{2\omega}$ displays a linear dependence on the magnetic field (Fig. A.1c) and follows a cosine angular dependence with α (Fig. A.2a), which resembles the ordinary Nernst effect in Pt [129]. As temperature increases, the second harmonic voltage decreases (Fig. A.2b). Notably, the symmetric component decays more rapidly. At $T = 20$ K, only the antisymmetric component remains.

In device 2 at $T = 2.5$ K, still the second harmonic voltage $V_{2\omega}$ can split into the symmetric and antisymmetric components (Fig. A.3a). The antisymmetric component $V^{as}_{2\omega}$ retains linear field dependence (Fig. A.3c) and cosine angular behavior with α (Fig. A.4a). However, the symmetric component $V^s_{2\omega}$ exhibits distinctly different angle dependence compared to that in device 1. $V^s_{2\omega}$ seems to have a plateau for $30° \leq \alpha \leq 90°$ and changes rapidly between 160° and 200° (Fig. A.4a). The overall magnitude of $V_{2\omega}$ decreases as temperature increases (Fig. A.4b). For $\alpha = 0°$, the symmetric component $V^s_{2\omega}$ remains approximately zero for temperature range from 3 K to 20 K, whereas the antisymmetric component $V^{as}_{2\omega}$ gradually declines (Fig. A.5). For $\alpha = 160°$, a signficant $V^s_{2\omega}$ emerges at 3 K, having about half the magnitude of $V^{as}_{2\omega}$; both $V^s_{2\omega}$ and $V^{as}_{2\omega}$ decrease as temperature rises, with only $V^s_{2\omega}$ vanishing above 20 K.

In summary, the antisymmetric $V^{as}_{2\omega}$ seems to consistently reflect the ordinary Nernst effect in Pt: having linear behavior with magnetic field and cosine depen-

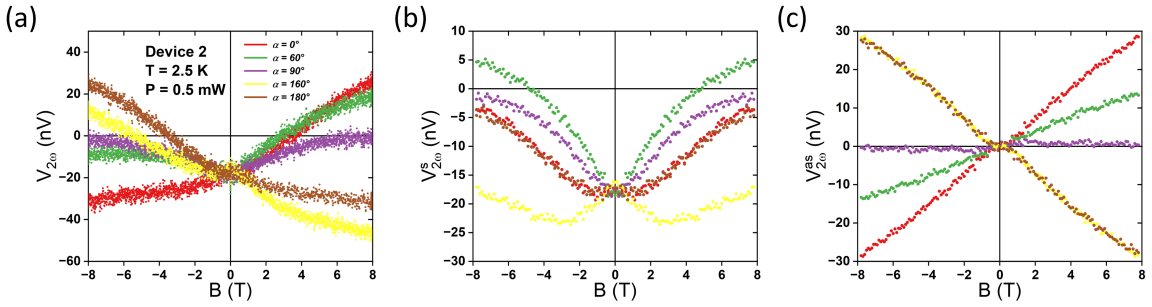

Figure A.3 : (a) The second harmonic voltage as a function of field with different field orientations at 2.5 K in device 2. The symmetric component (b) and the anti-symmetric component (c) as a function of field.

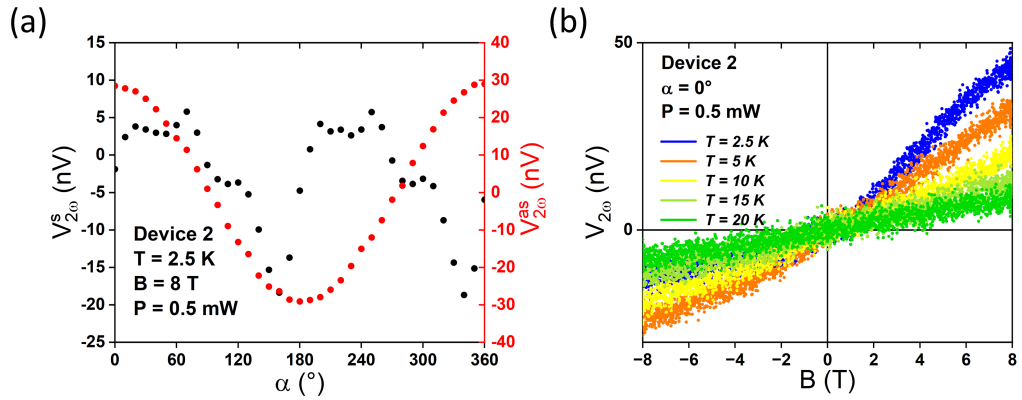

Figure A.4 : (a) Dependence of the symmetric and antisymmetric components of the second harmonic signal in device 2 at 2.5 K and 8 T with 0.5 mW heater power on in-plane field orientation α. (b) Field dependence of the second harmonic signal at different temperatures in device 2 with $\alpha = 0°$ and 0.5 mW heater power. As temperature increases, the signal decreases in magnitude.

dence on field orientation, and diminishing at higher temperatures; the symmetric $V^s_{2\omega}$ behaves in a device-dependent manner: device 1 shows a smooth dependence while device 2 exhibits plateaus and abrupt transitions. In both devices, $V^s_{2\omega}$ decays faster with temperature than $V^{as}_{2\omega}$, disappearing above 20 K.

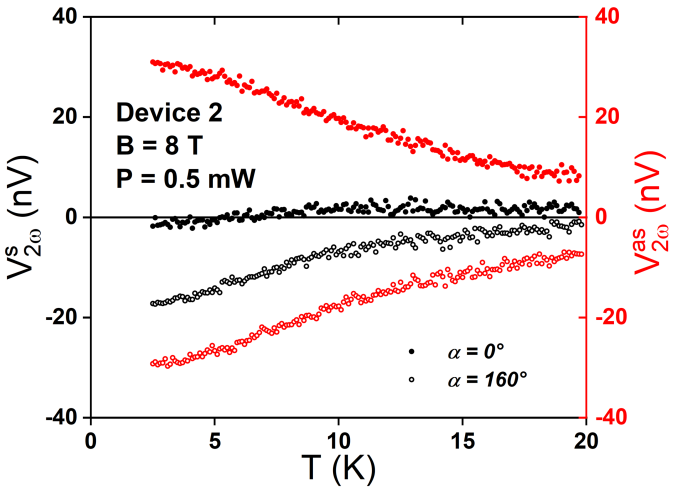

Figure A.5 : Temperature Dependence of the symmetric and antisymmetric components of the second harmonic signal in device 2 at 8 T with 0.5 mW heater power for $\alpha = 0°$ and 160°.

A.3 Nonlocal SSE in dysprosium titanate

To measure the nonlocal spin Seebeck response in $Dy_2Ti_2O_7$, we fabricated two devices with different Pt nanowire geometries.

Device 3 has Pt nanowires 100 μm long, 2 μm wide, 10 nm thick, separated by 1.5 μm, made by photolithography, magnetron sputtering and liftoff process. Typical

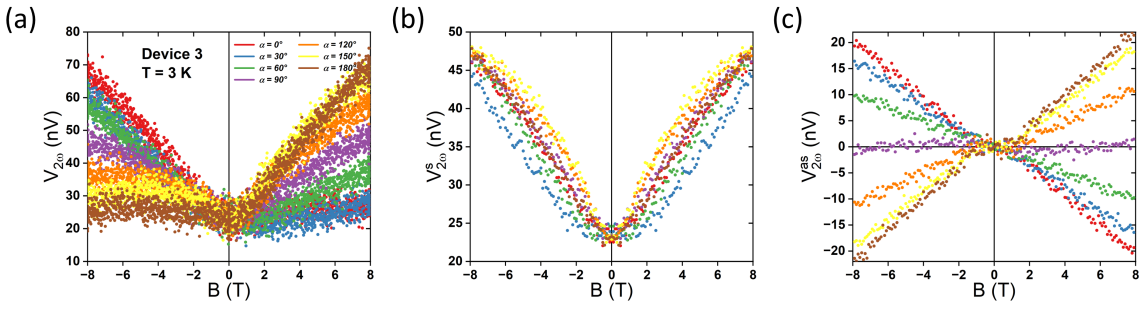

Figure A.6 : (a) The second harmonic voltage as a function of field with different field orientations at 3 K in device 3. The symmetric component (b) and the antisymmetric component (c) as a function of field. The heater current is 800 μA.

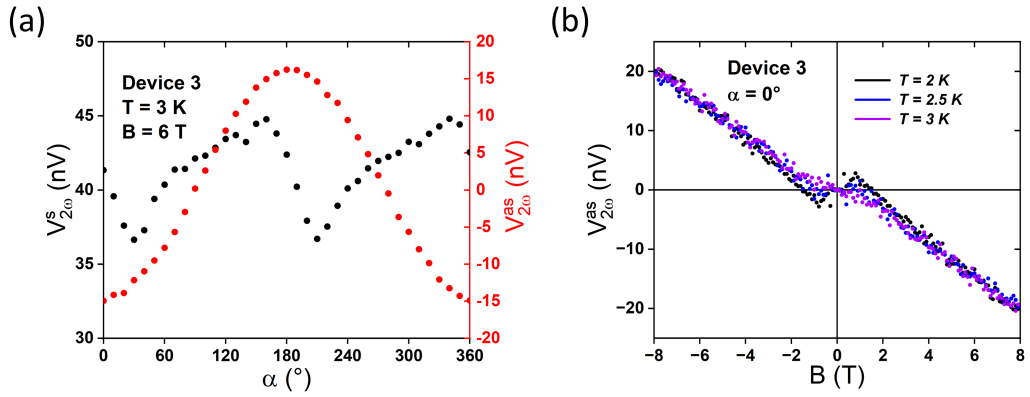

Figure A.7 : (a) Dependence of the symmetric and antisymmetric components of the second harmonic signal in device 3 at 3 K and 6 T on in-plane field orientation α. (b) Field dependence of the second harmonic signal at lower temperatures in device 3 with $\alpha = 0°$. The heater current is 800 μA.

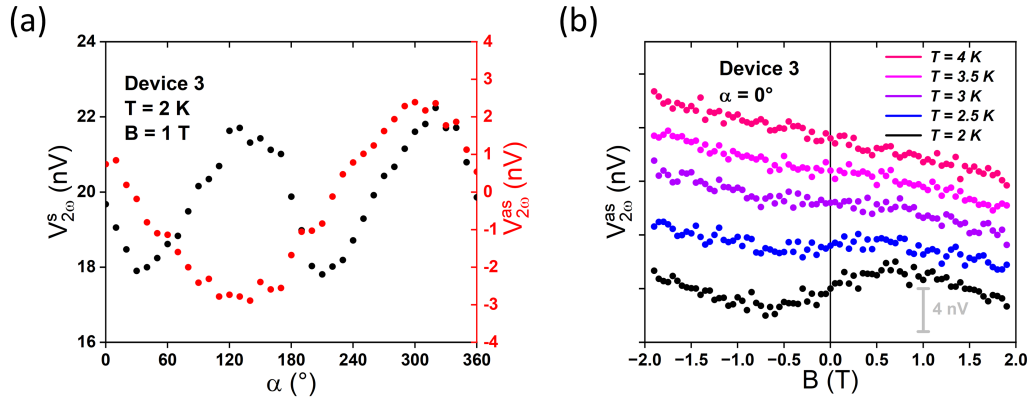

Figure A.8 : (a) Dependence of the symmetric and antisymmetric components of the second harmonic signal in device 3 at 2 K and 1 T on in-plane field orientation α. (b) Field dependence of the second harmonic signal at different temperatures in device 3 with $\alpha = 0°$. The heater current is 800 μA.

resistance of each wire is 1.8 kΩ. The wires are along the $[1\bar{1}0]$ axis of DTO. The magnetic field dependence of second harmonic voltage $V_{2\omega}$ in device 3 for different in-plane field orientations at $T = 3$ K is shown in Fig. A.6a. Similar to LSSE voltages, the nlSSE voltages have a strong symmetric component. The symmetric component $V^s_{2\omega}$ has a nearly parabolic dependence on field and weak angular variation with field

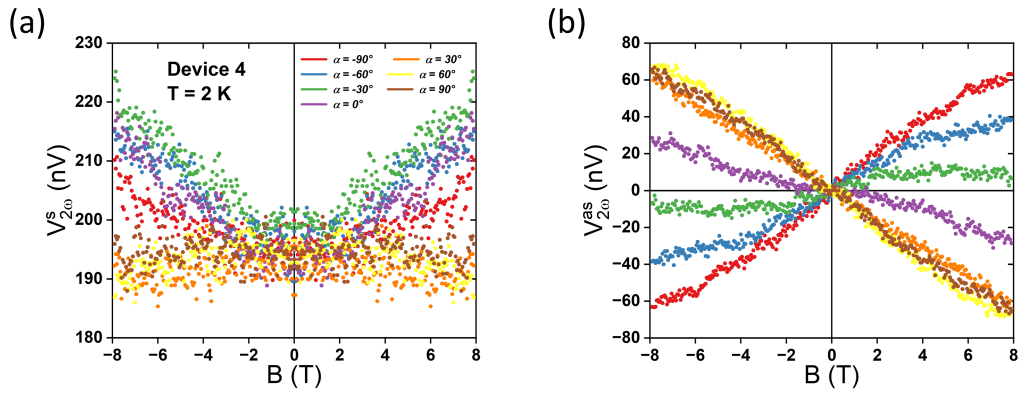

Figure A.9 : The symmetric component (a) and the antisymmetric component (b) of the second harmonic voltage as a function of field with different field orientations at 2 K in device 4. The heater current is 10 μA.

orientation α (Fig. A.6b). In contrast, the antisymmetric component $V^{as}_{2\omega}$ has a zero plateau in $|\boldsymbol{B}| < 1$ T, and then grows linearly with field above 1 T (Fig. A.6c). $V^{as}_{2\omega}$ at 6 T has a cosine dependence with α, with maximum magnitude for field perpendicular to the wire and zero for field along the wire (Fig. A.7a). When temperature decreases down to 2 K, $V^{as}_{2\omega}$ reverses sign for field below 2 T, showing a peak at 1 T (Fig. A.7b). This "1 T anomaly" corresponds to the peak behavior in the adiabatic susceptibility at the same temperature, which is associated with monopole condensation in spin ice [168]. Although it has cosine dependence with α, the antisymmetric component of this 1 T anomaly at 2 K shows the minimum at $\alpha = 160°$ and the maximum at $\alpha = 300°$ (Fig. A.8a), different from $V^{as}_{2\omega}$ at 3 K and 6 T. With increasing temperature, the anomaly changes from a peak at 2 K, to a zero plateau at 3 K, and finally disappears at 4 K (Fig. A.8b).

Device 4 has Pt nanowires 100 μm long, 200 nm wide, 10 nm thick, separated by 400 nm, made by e-beam lithography, sputtering and liftoff process. Typical resistance of each wire is 300 kΩ. The antisymmetric component $V^{as}_{2\omega}$ is linear to the

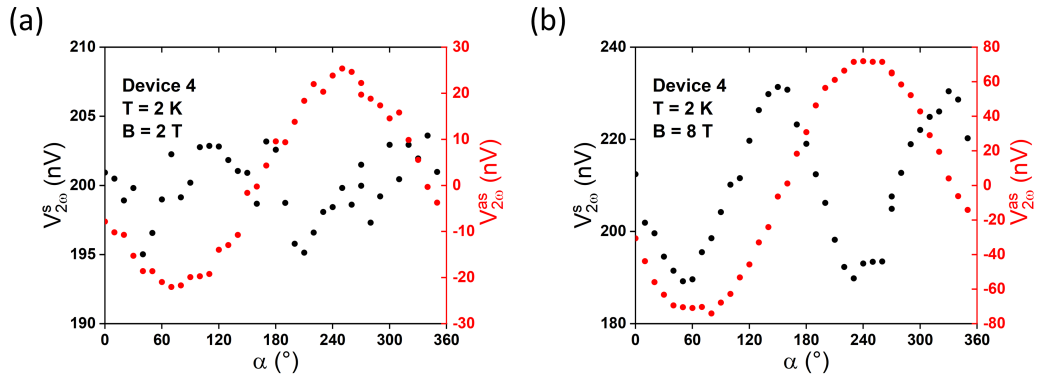

Figure A.10 : Dependence of the symmetric and antisymmetric components of the second harmonic signal in device 4 at 3 K and 2 T (a) or 8 T (b) on in-plane field orientation α. (b) The heater current is 10 μA.

field around 0 T and deviates from linear dependence at high fields (Fig. A.9b). The most striking is that $V^{as}_{2\omega}$ is small when field is perpendicular to the wire and reaches large magnitude when field is along the wire, contradict to what was observed in the device 3 (Fig. A.9a). The signal has opposite sign for α = -90° and 90°. At 2 T and 8 T, $V^{as}_{2\omega}$ shows a cosine dependence with α, with the maximum magnitude at α = 240° and the minimum one at α = 60° (Fig. A.10). As temperature increases, $V^{as}_{2\omega}$ remains nearly constant from 2 K to 5 K, and then decreases gradually from 5 K to 10 K (Fig. A.11).

A.4 Procedure for e-beam lithography on insulating substrates

Since both the $Dy_2Ti_2O_7$ film and YSZ substrate are highly insulating, surface charging during the e-beam exposure on DTO film can be a major concern. To address this problem, we use a thin, water-soluble polymer poly(4-styrenesulfonic acid) (PSSA) layer and a metal coating. The detailed procedure is as follows:

1) Spin-coat a standard double-layer PMMA on the DTO film as usual.

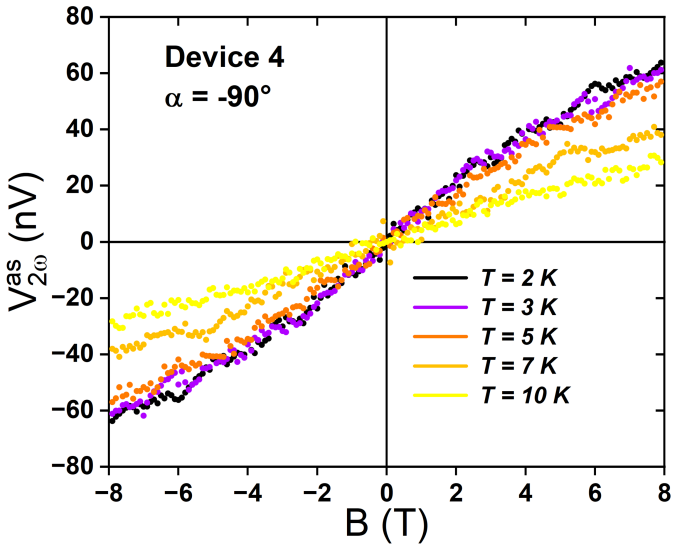

Figure A.11 : Field dependence of the second harmonic signal at different temperatures in device 4 with α = -90°. The heater current is 10 μA.

2) After PMMA coating, spin-coat a 4.5 wt% PSSA solution at 3,000 rpm for 60 seconds. Then bake at 220°C for 2 minutes.

3) Evaporate a 5-10 nm thick Cr film onto the PSSA layer.

4) Do the e-beam lithography process. During the exposure, ensure the sample is well grounded to the sample holder. It can be achieved by a small metal bridge connecting the film to the screw on the sample holder.

5) After exposure, rinse the sample in the deionized water to get rid of the PSSA layer and the Cr film on it, and then blow dry.

6) Develop the PMMA layer using the standard MIBK:IPA developer. Proceed with subsequent processing (deposit/lift-off) as usual.

Appendix B

Nonlocal spin transport measurements in multiferroics

B.1 Introduction of nonlocal measurements

The nonlocal geometry consist of two parallel spin-orbit metal (SOM) electrodes deposited on a magnetic insulator (MI). One electrode serves as injector, the other as detector. When a charge current I is sent through the injector, the spin Hall effect (SHE) generates a transverse spin current within the injector electrode, leading to a spin accumulation μ_s at the SOM/MI interface. If the spin orientation of μ_s is parallel or antiparallel to the average magnetization $\boldsymbol{M}$ of the MI, magnons in the MI are annihilated or excited due to the interfacial spin-flipping scattering, creating a nonequilibrium magnon population in the MI. These nonequilibrium magnons diffuse in the MI, producing a magnon current $\boldsymbol{j}_m$ from the injector to the detector. At the detector, the reciprocal process occurs: magnons interact at the interface and then create a spin current in the detector electrode. Owing to the inverse spin Hall effect (ISHE), this induced spin current is converted into a charge current, which under open-circuit conditions generates a nonlocal voltage V_{EI} arising from electrically injected magnons. At the same time, magnons can also be thermally excited by the spin Seebeck effect, leading to another nonlocal voltage V_{SSE}.

When an ac current of angular frequency ω is applied to drive the injector, the resulting voltage V_{EI} also oscillates at ω, whereas V_{SSE} oscillates at 2ω. With a lock-

in amplifier, both V_ω and $V_{2\omega}$ can be extracted simultaneously from the measured voltage across the detector, where V_ω corresponds to V_{EI} and $V_{2\omega}$ corresponds to V_{SSE}, respectively.

B.2 Nonlocal measurements in strontium iridium oxide / bismuth ferrite devices

The $BiFeO_3$ (BFO) thin film of 100 nm thickness was grown on the $TbScO_3$ substrate by pulsed laser deposition (PLD). Subsequently, the $SrIrO_3$ (SIO) layer of 20 nm thickness was deposited using molecular-beam epitaxy (MBE) in an atmosphere of 80% ozone and 20% O_2 mixture, along with elemental sources of strontium and iridium. Due to the epitaxial strain, the BFO film favors 109° ferroelastic domains and exhibits only one variant of the spin cycloid which propagates along $\boldsymbol{k} \parallel [101]$ axis and persists across the ferroelastic domain walls [174].

Two parallel wires, each 100 μm long and 1.2 μm wide, spaced 1.5 μm apart, were defined by photolithography and ion milling. In the "measurement configuration", an AC current of frequency $f = 7.7$ Hz is driven through the injector wire and the voltage across the detector wire is measured at both the first (V_ω) and the second ($V_{2\omega}$) harmonic frequencies. In the "pulsing configuration", a unipolar (30 ms, ± 50 V) voltage pulse is applied between the injector wire and the detector wire. During the measurements, the BFO film was first poled in the pulsing configuration, after which the nonlocal voltage on the detector wire is measured in the measurement configuration. The pulse polarity is then reversed, and the measurements are repeated.

At 300 K, we observed the change of the first harmonic voltage V_ω upon reversing the poling direction (Fig. B.1a). The difference of V_ω between the two poling

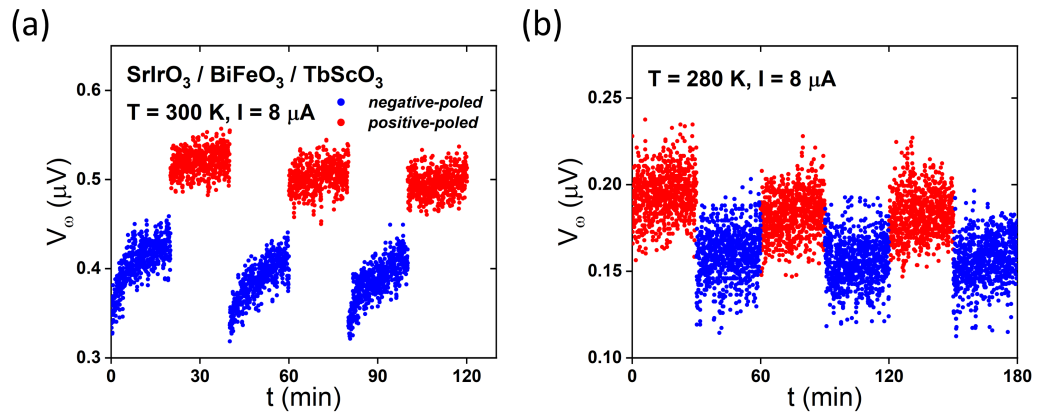

Figure B.1 : Measured first harmonic nonlocal voltage as a function of time at 300 K (a) and 280 K (b). 20 minutes for (a) and 30 minutes for (b) of data are collected after each voltage pulse. The injector current is set to 8 μA.

directions is $\sim$ 0.1 μV. When temperature is cooling down to 280 K, the change in V_ω persisted but decreased to 0.04 μV (Fig. B.1b). At 250 K, no measurable difference in V_ω was detected between the two poling states. A detailed temperature dependence is shown in Fig. B.2. As temperature decreases from 300 K to 250 K, a gradual decrease of V_ω is clearly seen, indicating worse spin conductance with deceasing temperature.

B.3 Nonlocal measurements in strontium iridium oxide / Lanthanum-doped bismuth ferrite devices

The 90-nm-thick $La_{0.15}Bi_{0.85}FeO_3$ (LBFO) thin film was grown on the $DyScO_3(110)$ substrate by PLD; then the $SrIrO_3$ (SIO) layer of 20 nm thickness was deposited via MBE. The 15% La-substitution transforms the ground state of LBFO from a pure spin cycloid phase to a mixed state comprising both spin cycloid phase and canted antiferromagnetic phases [175]. When an electric field is applied along the [100] direction, in-plane poling produces a single uniform ferroelectric domain with a single

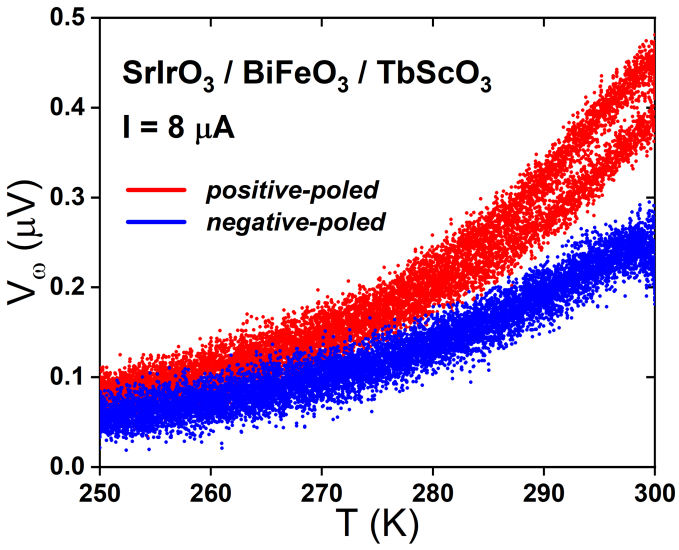

Figure B.2 : Temperature dependence of the first harmonic voltage for two poling conditions. The injector current is set to 8 μA.

variant of the spin cycloid and has the capacity to control the sign of the magnon spin current in the LBFO film; however, for a field along the [010] direction, a blocky multi-domain configuration persists even in the poled region [175].

Two parallel wires, each 100 μm long and 1.2 μm wide, spaced 1.5 μm apart, were defined by photolithography and ion milling. The typical resistance for one wire ranges from 100 kΩ to 3 MΩ, since SIO is sensitive to moisture. Following the ion milling, a 30-minute annealing in pure O_2 atmosphere is preferred. In the measurements, a voltage pulse (10 ms, $\pm$ 40 V) is applied between the injector wire and the detector wire. Following each electrical pulse, an ac current of frequency f = 7.7 Hz is introduced into the injector wire, and the voltage across the detector wire is measured at both the first and the second harmonic frequencies.

Before the temperature cycle, we observed the changes of both the first and the second harmonic voltage (V_ω and $V_{2\omega}$) upon reversing the poling direction at 300

K (Fig. B.3). However, after cooling the device down to 1.8 K and subsequently warming it up back to 300 K, the change of V_ω and $V_{2\omega}$ disappeared (Fig. B.4). It suggests that cooling may degrade the interface between SIO and LBFO.

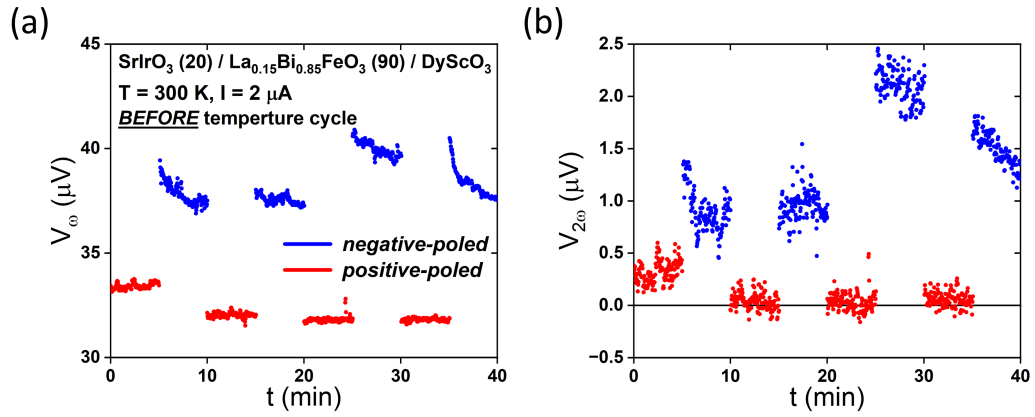

Figure B.3 : (a) The first harmonic voltage and (b) the second harmonic voltage as a function of time at 300 K before the temperature cycle. 5 minutes of data are collected after each voltage pulse. The injector current is set to 2 μA.

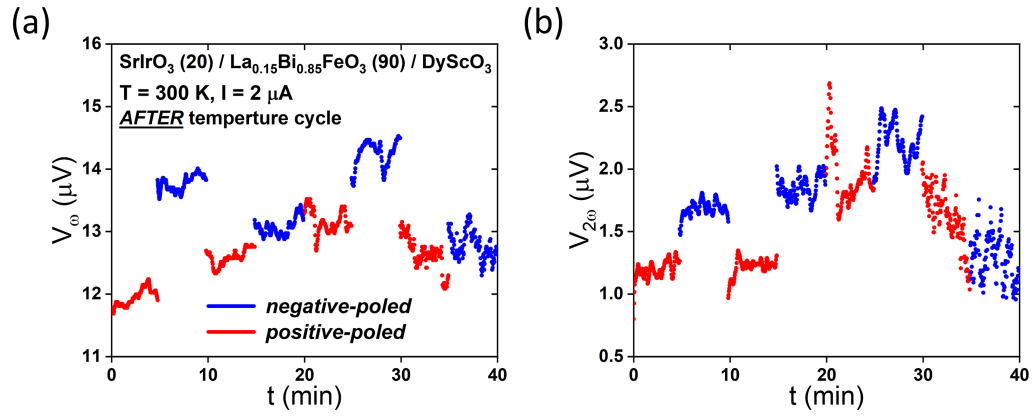

Figure B.4 : (a) The first harmonic voltage and (b) the second harmonic voltage as a function of time at 300 K after the temperature cycle. 5 minutes of data are collected after each voltage pulse. The injector current is set to 2 μA.